

國立臺灣大學理學院應用物理研究所

博士論文

Graduate Institute of Applied Physics

College of Science

National Taiwan University

Doctoral Dissertation

p 型及 n 型半導體之反向自旋霍爾效應

Inverse spin Hall effect in p -type and n -type
semiconductors

翁怡鍵

Yi-Chien Weng

指導教授: 林昭吟博士、梁啟德博士

Advisor: Dr. Jauyn Grace Lin, Dr. Chi-Te Liang

中華民國 109 年 7 月

July 2020



國立臺灣大學博士學位論文
口試委員會審定書

p 型及 n 型半導體之反向自旋霍爾效應

Inverse spin Hall effect in p -type and n -type
semiconductors

本論文係 翁怡鍵 君 (D02222007) 在國立臺灣大學物理學系、
所完成之博士學位論文，於民國 109 年 07 月 15 日承下列考試委員審
查通過及口試及格，特此證明

口試委員：

林昭吟 梁啟德 (簽名)

黃榮文 (指導教授)

黃其鈞

白奇峰

致謝



在博士的求學生涯當中經歷了很的喜悅及挫折。在研究方面從一開始的盲目摸索到後來有系統性的研究，這些成長與改變要感謝我的兩位指導教授林昭吟博士以及梁啟德博士。謝謝您們提供最好的研究資源讓我可以探索新穎且重要的科學領域：自旋電子學，同時也鼓勵我參加國際會議了解相關領域最先進的研究成果。最重要的是培養我做研究所需的基本能力及態度，同時需要改進的地方我也會持續加強。

同時也要感謝我的太太偲宇及家人在研究遇到瓶頸時給我鼓勵及關懷。你們是我完成學位的重要支柱及動力來源，謝謝你們無怨無悔的為我付出。再來也謝謝實驗室的學長冠宇、明遠、友生、Ramesh 及學弟驛翔、子翔、欽漢謝謝你們在實驗上的教導及各方面的幫助讓我可以快速上手以及突破思考的盲點。感謝冠儒在程式計算方面的教導及協助，還有宏宜、宗煜及智維學長平時的關心及幫忙。此外也謝謝普物實驗室的各位成員及求學期間所有幫助過我的朋友，你們讓我的研究生生活多了許多歡樂且美好的記憶。

中文摘要



矽和砷化鎵是很重要的自旋半導體材料因為它們具有較大的自旋生命週期 (spin lifetime) 或反向自旋霍爾角 (inverse spin Hall angle)，同時他們也是現今電子元件中不可或缺的材料之二。然而關於這些半導體材料的自旋傳輸特性及傳輸機制尚未被完整研究及討論。從過去研究結果發現，各種半導體材料的反向自旋霍爾角符號及大小差異是由於 n 型和 p 型半導體中的摻雜濃度及摻雜原子不同所導致。為了理解半導體材料中自旋傳輸現象以及摻雜效應對自旋軌道交互作用的影響，我們利用鐵磁共振式自旋幫浦的技術來對矽和砷化鎵材料中的摻雜效應進行有系統的研究，並且精準量測到幾個關鍵的自旋傳輸參數，例如：自旋生命週期、自旋擴散長度 (spin diffusion length) 及反向自旋霍爾角。

藉由改變矽半導體中的載子種類 (n 型和 p 型) 及摻雜濃度 (1×10^{13} to $1 \times 10^{19} \text{ cm}^{-3}$) 觀察到自旋擴散長度和反向自旋霍爾角之間的關聯性，也證明了可以藉由改變摻雜濃度及摻雜原子來有效調控自旋-電荷間的轉換效率。同時計算出矽的自旋擴散長度和自旋霍爾角乘積為 17.8 nm，該值略大於白金的實驗結果 (12.8 nm)。此結果顯示矽半導體的大範圍可調控性將成為具有發展潛力的自旋電子應用材料。此外，反向自旋霍爾角的大小與摻雜原子序 (Z) 相關但其符號與載子種類無關。從砷化鎵的研究中觀察到反向自旋霍爾角的數值與 Z^2 成正比。該結果與 Landau-Lifshitz Z^2 scaling 的理論模型相符。該模型考慮了各種元素外層電子對自旋耦合效應的影響而非只討論特定元素如過渡金屬。藉由該研究結果可以深入了解到半導體材料中摻雜效應對自旋-電荷間轉換效率的影響。由於自旋電子流的節能特性使自旋電子元件成為下世代的發展主軸，因此這研究成果將有助於半導體自旋電子元件的開發與設計，如新型自旋場效電晶體 (spin-based CMOS)。

關鍵字：自旋幫浦，自旋進動，摻雜效應，反向自旋霍爾角，自旋生命週期，自旋

擴散長度，半導體。



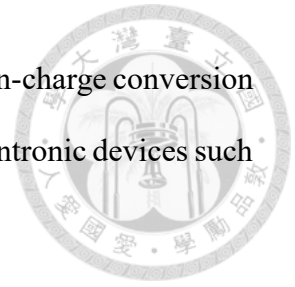
Abstract



Silicon (Si) and gallium arsenide (GaAs) are two important semiconducting materials for the applications of spintronics due to either long spin lifetime (for Si) or large inverse spin Hall angle (for GaAs) compared to those of other semiconductors (SC). Meanwhile, they are already the essential parts of modern electronic devices. However, for practical applications, the complete knowledge about the spintronic properties and the related mechanism in SC is still not established yet. In particular, the reported results on the magnitude and the sign of θ_{ISHE} in the various SCs are rather diversified due to the fact that the doping concentration and dopants atom in *n*-type and *p*-type sample are always different. In order to understand the behavior of spintronic transport and the dopant effect on spin-orbit interaction in SCs, we adopted the technique of ferromagnetic resonance driven spin pumping (FMR-SP) to accurately determine several critical parameters, including the τ_s , the spin diffusion length (λ_s) and the θ_{ISHE} in the Si and GaAs single crystal.

By changing the type (*n*- and *p*-type) of carrier and the doping concentration (1×10^{13} to $1 \times 10^{19} \text{ cm}^{-3}$) for Si, a correlation between λ_s and θ_{ISHE} is found, demonstrating an effective route to tune the efficiency of spin-charge conversion by changing the doping concentration and dopant atoms. A constant value of $\lambda_s \theta_{ISHE}$ (17.2 nm) for Si is found to be larger than Py (12.8 nm), indicating that Si is as effective as Pt in terms of converting the spin current to charge current for the application of spintronic devices. Furthermore, the magnitude of θ_{ISHE} is sensitive to the atomic number of dopant (*Z*), but the sign of θ_{ISHE} is independent on the carrier type. The relationship between θ_{ISHE} of GaAs and *Z* follows the Landau-Lifshitz Z^2 scaling, in agreement with the model considering only the outmost electron for non-specific atoms. The overall results of this study provide

an in-depth understanding for the influence of dopant effect on the spin-charge conversion rate of SC, which benefits the future applications of energy-saving spintronic devices such as new type of field emission spin-based MOSFET.



Keywords: Spin pumping, Spin precession, Dopant effect, Inverse spin Hall angle, Spin lifetime, Spin diffusion length, Semiconductor.

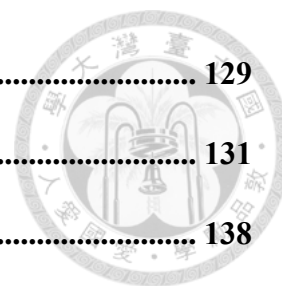
Contents



| | |
|--|-----------|
| 致謝 | I |
| 中文摘要 | II |
| Abstract | IV |
| Contents | VI |
| List of figures | IX |
| List of tables | XVI |
| Chapter 1 Introduction | 1 |
| 1.1 Development of spintronic devices | 1 |
| 1.2 Injection and detection techniques of spin current | 4 |
| 1.3 Types of spintronic devices | 10 |
| 1.3.1 Magnetoresistive random access memory (MRAM) device | 11 |
| 1.3.2 Spin transfer torque MRAM (STT-MRAM) | 13 |
| 1.3.3 Spin orbit torque MRAM (SOT-MRAM) | 14 |
| 1.3.4 Spin-based Metal-Oxide-Semiconductor field-effect transistor (Spin-based MOSFET) | 16 |
| 1.4 Motivation | 18 |
| Chapter 2 Theoretical background | 21 |
| 2.1 Quantum description of spin-orbit interaction | 21 |
| 2.2 Spin-orbit interaction in the semiconductors | 22 |
| 2.2.1 The band structure with spin-orbit interaction | 22 |
| 2.2.2 The Spin relaxation in multivalley semiconductor | 24 |
| 2.3 Spin Hall effect (SHE) | 28 |
| 2.3.1 Phenomenological description | 28 |
| 2.3.2 Physical mechanism of spin Hall effect | 29 |
| 2.4 Magnetization dynamics and ferromagnetic resonance (FMR) | 33 |

| | | |
|------------------|---|-----------|
| 2.5 | Phenomenological model of Spin pumping..... | 37 |
| 2.5.1 | Spin pumping and inverse spin Hall effect (ISHE) | 37 |
| 2.5.2 | Spin precession | 41 |
| Chapter 3 | Experimental techniques..... | 44 |
| 3.1 | Magnetron Sputtering | 44 |
| 3.1.1 | Principle of sputtering | 44 |
| 3.1.2 | Sputtering system | 48 |
| 3.2 | Thin film deposition | 50 |
| 3.2.1 | Principle of thin film deposition..... | 50 |
| 3.2.2 | Sample preparation | 57 |
| 3.3 | Measurements | 60 |
| 3.3.1 | Hall effect | 60 |
| 3.3.2 | High resolution transmission electron microscopy (HRTEM) | 62 |
| 3.3.3 | Vibrating-Sample Magnetometer (VSM) | 64 |
| 3.3.4 | Ferromagnetic resonance (FMR) and Inverse spin Hall effect (ISHE) | 67 |
| Chapter 4 | Result and discussions | 72 |
| 4.1 | Spintronic transport in Si with different doping concentration and dopants .. | 72 |
| 4.1.1 | Hall effect measurement for Si | 72 |
| 4.1.2 | Microstructures and magnetic properties of Co/Si | 74 |
| 4.1.3 | Ferromagnetic resonance and inverse spin Hall effect results of reference sample [Pt (10 nm)/Co (t_{Co} nm)/unpoded] | 81 |
| 4.1.4 | Ferromagnetic resonance results of Co (t_{Co} nm)/Si | 86 |
| 4.1.5 | Effective damping constant and effective spin mixing conductance for Co (t_{Co} nm)/Si | 90 |
| 4.1.6 | Inverse spin Hall effect of Co (t_{Co} nm)/Si | 94 |
| 4.1.7 | Spin lifetime and spin diffusion length of Si | 99 |
| 4.1.8 | Inverse spin Hall angle of Si | 102 |
| 4.2 | The dopant effect on spin-orbit interaction in GaAs | 109 |
| 4.2.1 | Hall effect measurement for GaAs | 109 |
| 4.2.2 | Magnetic properties of Co/GaAs | 110 |
| 4.2.3 | Ferromagnetic resonance and effective damping constant of Co (t_{Co} nm)/GaAs. | 114 |
| 4.2.4 | Inverse spin Hall effect, spin lifetime, spin diffusion length and inverse spin Hall angle of GaAs | 119 |

| | |
|-----------------------------------|------------|
| Chapter 5 Conclusion | 129 |
| References..... | 131 |
| List of publications | 138 |
| Appendix A..... | 139 |
| Appendix B..... | 145 |
| Appendix C..... | 154 |



List of figures

- Fig. 1.1 The illustration of the two-current model. The transport paths of electrons spin up and down have two different cases in the ferromagnetic multilayer: current-in-plane (CIP) and current-perpendicular-to-plane (CPP) transport. The equivalent resistance of circuit depends on the configuration of two adjacent magnetizations..... 1
- Fig. 1.2 The illustration of the charge and spin current. 2
- Fig. 1.3 MR of three different Fe/Cr superlattices and the MR ratio is depended on the superlattices structure. 4
- Fig. 1.4 The illustration of (a) spin Hall effect and (b) Inverse spin Hall effect 5
- Fig. 1.5 (a) The experimental setup of SHE measurement for GaAs sample. (b) The typical spectra of KR as a function of magnetic field for $x = 35$ and $-35\mu\text{m}$ and the signal changes sign for the two edges of the sample. (c) Two-dimensional images of spin density and reflectivity for GaAs sample with $E = 10 \text{ mV } \mu\text{m}^{-1}$. This result show that an accumulation of electron spin polarized in the $+z$ ($-z$) at $x = 35$ (-35) μm 6
- Fig. 1.6 (a) Image of atomic force microscope for device (b) The measurement scheme of SHE measurement (c) Result of R_{SH} vs. B_{\perp} for $t_{Al} = 12 \text{ nm}$ and $L_{SH} = 860 \text{ nm}$ (top), 590 nm (middle) and 480 nm (bottom)..... 7
- Fig. 1.7 (a) The schematic diagram of spin pumping measurement. (b) The FMR and ISHE spectra of Py/Pt bilayer with different field direction (θ). The signal of ISHE is decrease with changing θ from 90° to 0° ; this result consistent with the relation between j_c and j_s ($j_c \propto \theta_{ISHE} j_s \times \sigma$) 8
- Fig. 1.8 (a) Schematic illustration of the spin transfer torque extra on the magnetization of Py and setup of ST-FMR measurement. The dimension of sample is $20 \mu\text{m}$ wide and $110 \mu\text{m}$ long. (b) the DC voltage signal of ST-FMR for Pt(6 nm)/Py(4 nm) sample measured under frequencies of 5-10 GHz. 9
- Fig. 1.9 (a) The schematic diagram of the Py/*p*-Si film. (b) The FMR and ISHE spectra of Py/*p*-Si film. 10
- Fig. 1.10 The summary of Mott- and Dirac-types spintronic devices. 11
- Fig. 1.11 The Schematic diagram of (a) first generation MRAM. The next

| | | |
|-----------|--|----|
| | generation MARAM (b) STT-MRAM and (c) SOT-MRAM. | 12 |
| Fig. 1.12 | The Schematic diagram of switching magnetization by STT in the MRAM cell. (a) switch from AP to P (b) switch from AP to P. | 14 |
| Fig. 1.13 | The illustration of the SOT effect on the magnetization. The direction of τ_{SO} is parallel or antiparallel to the damping torque and the τ_{FL} is perpendicular to the damping torque. | 15 |
| Fig. 1.14 | The illustration of spin-based MOSFET. Spin current spin current transport from the source to the drain through a SC channel and the transmission properties of channel can be controlled by applying a voltage bias. | 17 |
| Fig. 2.1 | Schematic diagram of a direct band-gap structure near $k = 0$ for bulk semiconductor. | 24 |
| Fig. 2.2 | Diagram of dominant spin relaxation mechanisms in n -type silicon as a function of doping concentration and temperature. | 25 |
| Fig. 2.3 | (a) Substitutional impurity atom in a Si crystal host. (b) Scheme of the dominant impurity-driven spin relaxation mechanism (f -process intervalley scattering) (c) Energy levels of donor states for Silicon of the $1s$ state due to valleyorbit coupling with T_d symmetry. | 26 |
| Fig. 2.4 | Spin relaxation time in heavily doped n -type Si for three common donor type at low temperature. Solid line denotes the theory result and other marks denote experiment results. | 27 |
| Fig. 2.5 | Schematic diagram of spin-dependent Hall effect. | 29 |
| Fig. 2.6 | (a) The intrinsic spin Hall conductivity of transition metals are calculated by tight binding mode. (b) The spin Hall angle of the 5d transition metals are detected by spin pumping technique. (c) The anomalous Hall angle and the spin Hall angle of nonmagnetic Au and Pd hosts with magnetic 3d impurities from V to Ni. | 31 |
| Fig. 2.7 | The Schematic diagram of mechanism contribution in the different range and the mechanism of SHE as a function of $\hbar\tau/m^*$. The value of $\hbar\tau/m^*$ is approximately equal to 6 times the value of the mobility. | 33 |
| Fig. 2.8 | (a) The illustration of the magnetization precession with a damping effect. (b) The configuration of coordinate system for thin film. | 35 |
| Fig. 2.9 | (a) The schematic diagram of spin pumping under the FMR condition. (b) The schematic illustration of the coordinate system. | 38 |

| | | |
|-----------|--|----|
| Fig. 2.10 | The Schematic diagram of spin precession under the FMR condition..... | 42 |
| Fig. 2.11 | The calculation values of $V_{ISHE}(80^\circ)$ with different τ_s | 43 |
| Fig. 3.1 | The illustration of the sputtering collision..... | 45 |
| Fig. 3.2 | The configuration of typical example and the process of glow discharge. | 46 |
| Fig. 3.3 | A classification of gas discharge modes for different discharge current. . | 46 |
| Fig. 3.4 | (a) The orbital motion of electron around the magnetic field. The (b) Cycloid and (c) helical motion of electron under the magnetic and electric field..... | 47 |
| Fig. 3.5 | The configuration of (a) cylindrical type and (b) planar type magnetron sputtering systems. | 48 |
| Fig. 3.6 | The (a) multi-gun DC magnetron sputtering system and (b) the sputtering source..... | 49 |
| Fig. 3.7 | The detail configuration of (a) vacuum and (b) sputtering chamber for CVT TFS-4700 system. | 50 |
| Fig. 3.8 | The illustration of nucleation process..... | 52 |
| Fig. 3.9 | Three different growth mechanisms: Volmer-Weber (3D island growth), Frank-van der Merwe (2D layer by layer growth) and Stranski-Krastanow (S-K growth). | 53 |
| Fig. 3.10 | The typical deposition methods of thin film..... | 54 |
| Fig. 3.11 | The schematic of measurement for van der Pauw method..... | 60 |
| Fig. 3.12 | The schematic of (a) Hall effect system, (b) sample holder and (c) measured sample..... | 62 |
| Fig. 3.13 | The schematic of (a) transmission electron microscope and (b) light optical microscope..... | 63 |
| Fig. 3.14 | The picture of (a) FEGTEM and (b) FIB system (This picture download from High valued Instrument Center of NSYSU)..... | 64 |
| Fig. 3.15 | (a) The diagram of VSM measurement system. The typical $M - H$ loops measured parallel to (b) easy axis and (c) hard axis..... | 66 |
| Fig. 3.16 | The schematic of (a) VSM system and (b) the measurement set up of VSM. | 67 |
| Fig. 3.17 | The (a) photo and (b) schematic of Bruker EMX system. (c) The | |

| | |
|--|----|
| Magnetic and electric field patterns in a standard TE ₁₀₂ cavity | 68 |
| Fig. 3.18 The photo of (a) nano-voltmeter (b) sample holder..... | 69 |
| Fig. 3.19 The measurement set up of (a) FMR and (b) ISHE for reference sample, sample A and sample B, respectively..... | 70 |
| Fig. 4.1 The cross-section TEM images for Co (40)/Si samples. (a) the Co/ <i>undoped</i> -Si (b) Co/ <i>p</i> -Si-10 (c) Co/ <i>n</i> -Si-10 (d) Co/ <i>p</i> -Si-0.1 (e) Co/ <i>p</i> -Si-0.005. | 74 |
| Fig. 4.2 The images of HRTEM and electron diffraction patterns for Co (40)/Si samples. (a) the Co/ <i>undoped</i> -Si (b) Co/ <i>p</i> -Si-10 (c) Co/ <i>n</i> -Si-10 (d) Co/ <i>p</i> -Si-0.1 (e) Co/ <i>p</i> -Si-0.005. | 74 |
| Fig. 4.3 The $M - H$ loops of Co (t_{Co})/ <i>undoped</i> -Si and the t_{Co} change from 5 nm to 40 nm. | 75 |
| Fig. 4.4 The $M - H$ loops of Co (t_{Co})/ <i>p</i> -Si-10 and the t_{Co} change from 5 nm to 40 nm. | 76 |
| Fig. 4.5 The $M - H$ loops of Co (t_{Co})/ <i>n</i> -Si-10 and the t_{Co} change from 5 nm to 40 nm. | 76 |
| Fig. 4.6 The $M - H$ loops of Co (t_{Co})/ <i>p</i> -Si-0.1 and the t_{Co} change from 5 nm to 40 nm. | 77 |
| Fig. 4.7 The $M - H$ loops of Co (t_{Co})/ <i>p</i> -Si-0.005 and the t_{Co} change from 5 nm to 40 nm. | 77 |
| Fig. 4.8 The $m_s - t_{Co}$ curve for sample A and the red solid line is a linear fitting result. | 78 |
| Fig. 4.9 The $H_k - t_{Co}$ curve for sample A..... | 79 |
| Fig. 4.10 The $K_{eff} \times t - t_{Co}$ curve for sample A and the red solid lines are linear fitting result. | 80 |
| Fig. 4.11 The value of $4\pi M_{eff}$ for sample A. | 81 |
| Fig. 4.12 (a) The FMR spectrum for Pt/Co (10)/ <i>undoped</i> sample (dI/dH vs. H) and the open circle is fitting result by differential form of Lorentzian (b) voltage signals (V vs. H) for Pt/Co (10)/ <i>undoped</i> sample (c) The black curve is experiment data; red dash and blue dash-dot curves are ISHE and AHE fits to Eq.4.6..... | 82 |
| Fig. 4.13 The P_{MW} dependent (a) FMR spectra and (b) voltage signals for Pt/Co (10)/ <i>undoped</i> sample. | 83 |

| | | |
|-----------|--|----|
| Fig. 4.14 | The plot of V_{ISHE} v.s. P_{MW} for Pt/Co (10)/undoped sample which P_{MW} is varied from 20 to 100 mW and the red solid line is the linear fitting result. | 84 |
| Fig. 4.15 | The data of $I_c - t_{Co}$ curves for reference samples and the red solid curve is the fits to Eq. 2.46, Eq. 4.7 and Eq. 4.8. | 85 |
| Fig. 4.16 | The FMR spectra (dI/dH vs. H) for Pt/Co (10)/undopen and all Co (10)/Si samples. The open circle is fitting result using differential form of Lorentzian..... | 86 |
| Fig. 4.17 | The (a) H_r and (b) ΔH versus t_{Co} changing from 5 nm to 40 nm for reference and sample A, respectively. | 87 |
| Fig. 4.18 | The angular-dependence data of (a) H_r , calculational results of H_r (red line) and (b) ΔH for Pt/Co (10)/undopen and all Co (10)/Si samples, respectively. | 88 |
| Fig. 4.19 | The θ_M versus θ_H for Pt/Co (10)/undopen and all Co (10)/Si samples, respectively. | 89 |
| Fig. 4.20 | The value of (a) gyromagnetic ratio and (b) g-factor for sample A. | 90 |
| Fig. 4.21 | The α versus t_{Co} curve for reference sample and sample A. The red solid lines, blue and green dash-dot curves are described $\alpha_0 + \alpha_{SP} + \alpha_{EC}$, $\alpha_0 + \alpha_{SP}$ and $\alpha_0 + \alpha_{EC}$ fitting curves according to Eq. 4.8, respectively. | 92 |
| Fig. 4.22 | The $g_{eff}^{\uparrow\downarrow}$ v.s. N for reference sample and sample A. | 93 |
| Fig. 4.23 | The (a)~(f) FMR spectra with θ_H is 0° and (g)~(l) voltage signals θ_H are 0° and 180° for Pt/Co (10)/undoped and all Co (10)/Si samples, respectively. | 94 |
| Fig. 4.24 | The voltage signals with θ_H is 0° for Pt/Co (10)/undoped and all Co (10)/Si samples. The black, red dash and blue dash-dot curves are experiment data, ISHE and AHE fitting curves, respectively | 95 |
| Fig. 4.25 | The plot of V_{ISHE} with microwave power which is varied from 20 to 100 mW for all Pt/Co (10)/undoped and all Co (10)/Si samples..... | 96 |
| Fig. 4.26 | The thickness-dependence data of V_{ISHE} for reference sample and sample A. | 97 |

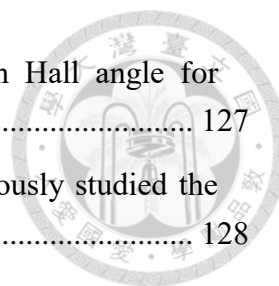
| | | |
|-----------|--|-----|
| Fig. 4.27 | The thickness-dependence data of I_c for reference sample and sample A. | 97 |
| Fig. 4.28 | The $V_{ISHE} - \theta_H$ curves for Pt/Co (10)/undoped and all Co (10)/Si samples. | 98 |
| Fig. 4.29 | The normalized value of $V_{ISHE}(\theta_H)$ [$V_{ISHE}(\theta_H)/V_{ISHE}(0)$] versus θ_H and the fitting result (red solid curves) for Co (10)/p-Si-10, Co (10)/n-Si-10, Co (10)/p-Si-0.1 and Co (10)/p-Si-0.005 samples. | 100 |
| Fig. 4.30 | (a) spin lifetime and (b) spin diffusion length versus resistivity of Si for Co (10)/p-Si-10, Co (10)/n-Si-10, Co (10)/p-Si-0.1 and Co (10)/p-Si-0.005 samples. | 102 |
| Fig. 4.31 | The plot of $I_c - t_{Co}$ curves and fitting result (red solid curve) for Co (10)/p-Si-10, Co (10)/n-Si-10, Co (10)/p-Si-0.1 and Co (10)/p-Si-0.005. | 105 |
| Fig. 4.32 | The plot of θ_{ISHE} with λ_s and the red line shows $\lambda_s \times \theta_{ISHE} \cong 17.2$ nm. The inset shows that $\lambda_s \times \theta_{ISHE} \cong 12.8$ for Py/Pt system studied by the FMR-SP technique and the data obtained from literature. ^{77,109-113} ... | 106 |
| Fig. 4.33 | The $M - H$ loops of Co (t_{Co})/p-GaAs and the t_{Co} is 5 nm, 10 nm, 30 nm and 40 nm. | 111 |
| Fig. 4.34 | The $M - H$ loops of Co (t_{Co})/n-GaAs and the t_{Co} is 5 nm, 10 nm, 30 nm and 40 nm. | 111 |
| Fig. 4.35 | The $m_s - t_{Co}$ curve for sample B and the red solid line is a linear fitting result. | 112 |
| Fig. 4.36 | The $K_{eff} \times t - t_{Co}$ curve for sample B and the red solid lines are linear fitting result. | 113 |
| Fig. 4.37 | The FMR spectra (dI/dH vs. H) for all Co (10)/GaAs samples. The open circle is fitting result using differential form of Lorentzian. | 114 |
| Fig. 4.38 | The (a) H_r and (b) ΔH versus t_{Co} changing from 5 nm to 40 nm for sample B. | 115 |
| Fig. 4.39 | The angular-dependence data of (a) H_r , calculational results of H_r (red line) and (b) ΔH for all Co (10)/GaAs samples. | 116 |
| Fig. 4.40 | The θ_M versus θ_H for all Co (10)/GaAs samples. | 116 |
| Fig. 4.41 | The α versus t_{Co} curve for sample B. The red solid lines, blue and green dash-dot curves are described $\alpha_0 + \alpha_{SP} + \alpha_{EC}$, $\alpha_0 + \alpha_{SP}$ and $\alpha_0 +$ | |

| | | |
|-----------|--|-----|
| | α_{EC} fitting curves according to Eq. 4.8, respectively..... | 118 |
| Fig. 4.42 | The $g_{eff}^{\uparrow\downarrow}$ v.s. N for reference sample, sample A and sample B. | 118 |
| Fig. 4.43 | (a) The FMR spectrum for Co (10)/ p -GaAs sample (b) voltage signals for Co (10)/ p -GaAs sample (c) The black, red dash and blue dash-dot curves are experiment data, ISHE and AHE fitting curves using Eq. 4.6. | 120 |
| Fig. 4.44 | (a) The FMR spectrum for Co (10)/ n -GaAs sample (b) voltage signals for Co (10)/ n -GaAs sample (c) The black, red dash and blue dash-dot curves are experiment data, ISHE and AHE fitting curves using Eq. 4.6. | 120 |
| Fig. 4.45 | The plot of V_{ISHE} with microwave power which is varied from 20 to 100 mW for all Co (10)/GaAs samples. | 121 |
| Fig. 4.46 | (a) and (b) The thickness-dependence data of V_{ISHE} and I_c , respectively for sample B. | 122 |
| Fig. 4.47 | The normalized value of $V_{ISHE}(\theta_H)$ [$V_{ISHE}(\theta_H)/V_{ISHE}(0)$] versus θ_H and the rea solid curves is fitting result for all Co (10)/GaAs samples.. | 123 |
| Fig. 4.48 | The plot of $I_c - t_{Co}$ curves for sample B and the red solid curves are the fitting result. | 124 |
| Fig. 4.49 | (a) Plot of the θ_{ISHE} vs. Z for various SCs listed in Table 4.11 and (b) for GaAs system with the black line being the fit of Z^2 | 126 |

List of tables

| | | |
|-----------|---|-----|
| Table 1.1 | The comparative analysis of STT- and SOT-MRAM..... | 16 |
| Table 3.1 | The special features of the four different deposition processes..... | 55 |
| Table 3.2 | Several methods of analysis are used in this work | 56 |
| Table 3.3 | The parameter and name of Si-substrate, and define the name for all samples. | 58 |
| Table 3.4 | The parameter and name of GaAs-substrate, and define the name for all samples. | 59 |
| Table 3.5 | The parameter of measurement for Hall effect, VSM, FMR and ISHE ... | 71 |
| Table 4.1 | The parameter of carrier concentration (N), resistivity (ρ), thickness (t_{Si}), Hall coefficient (R_H), mobility (μ) and diffusion constant (D_N) for silicon substrate. | 73 |
| Table 4.2 | The value of K_v and K_s of Sample A are extracted from intercept and slope of linear fitting result, respectively..... | 80 |
| Table 4.3 | The fitting results of damping constant and the value of effective spin mixing conductance for reference sample and sample A. | 93 |
| Table 4.4 | The calculation result and parameter of spin lifetime and spin diffusion length, respectively for Co (10)/ p -Si-10, Co (10)/ n -Si-10, Co (10)/ p -Si-0.1 and Co (10)/ p -Si-0.005 samples. | 101 |
| Table 4.5 | The calculation result and parameter of inverse spin Hall angle for reference sample and sample A. | 104 |
| Table 4.6 | The value of doping concentration, diffusion constant, spin-diffusion length, spin lifetime and spin Hall angle for p -Ge, p -Si, p -GaAs and n -GaAs. | 108 |
| Table 4.7 | The parameter of carrier concentration (N), resistivity (ρ), thickness (t_{GaAs}), Hall coefficient (R_H), mobility (μ) and diffusion constant (D_N) for GaAs substrate. | 110 |
| Table 4.8 | The value of M_s , K_v and K_s for Sample B, Co/ n -Si-10 and Co/ p -Si-10. | 113 |
| Table 4.9 | The fitting results of damping constant and the value of effective spin mixing conductance for sample B, Co/ p -Si-10 and Co/ n -Si-10..... | 119 |

| | |
|---|-----|
| Table 4.10 The calculation result and parameter of inverse spin Hall angle for sample B, Co/ <i>p</i> -Si-10, and Co/ <i>n</i> -Si-10..... | 127 |
| Table 4.11 The experimentally results of the team that simultaneously studied the θ_{ISHE} and λ_s of <i>n</i> - and <i>p</i> -type SC. | 128 |





Chapter 1 Introduction

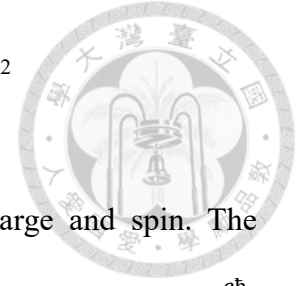
1.1 Development of spintronic devices

Spin is an “intrinsic” angular momentum of the particles in addition to the orbital angular momentum and it is a new degree of freedom for particles. In the pioneering work, Mott *et al.* reported that an unusual behavior of resistance in materials doped with magnetic impurities. This report provides a fundamental concept for understanding of spin-dependence transport and is also known as the two-current model, shown in Fig.1.1.¹⁻³ On the other hand, Paul A. M. Dirac exhibited that spin can be derived from the quantum mechanism and Einstein’s equation.⁴⁻⁶ However, spintronics is a multidisciplinary field whose important work is the effective control and application of spin degrees of freedom in solid-state systems.^{3,7-10}

| | Parallel configuration (P) | Anti-parallel configuration (AP) |
|--------------------|----------------------------|----------------------------------|
| CIP geometry | | |
| CPP geometry | | |
| Equivalent circuit | | |
| Resistance | $R = \frac{Rr}{R+r}$ | $R = \frac{R+r}{4}$ |

Fig. 1.1 The illustration of the two-current model. The transport paths of electrons spin up and down have two different cases in the ferromagnetic multilayer: current-in-plane (CIP) and current-perpendicular-to-plane (CPP) transport. The equivalent resistance of

circuit depends on the configuration of two adjacent magnetizations.²



An electron possesses two intrinsic degrees of freedom: charge and spin. The electron spin \mathbf{s} can be detected by its magnetic moment $\mu_s = -g\mu_B\mathbf{s}$, where $\mu_B = \frac{e\hbar}{2m_e}$ is the Bohr magneton and g-factor (g) is 2.0023 for electron. The electron spin projection on any direction can take only two values: $+\frac{1}{2}$ and $-\frac{1}{2}$. The normal electric current (unpolarized charge current) is described that the electrons flow with disordered spins. However, the spin current can be divided into several different types: spin polarized current, fully spin polarized current and pure spin current. The motion of charger with the different numbers of opposite spin (only one spin direction) called as spin polarized current (fully spin polarized current). On the other hand, pure spin current is described that the opposite spin flow to the different direction and without the net charge current. The schematic diagram of the charge and spin current is shown in the Fig. 1.2.

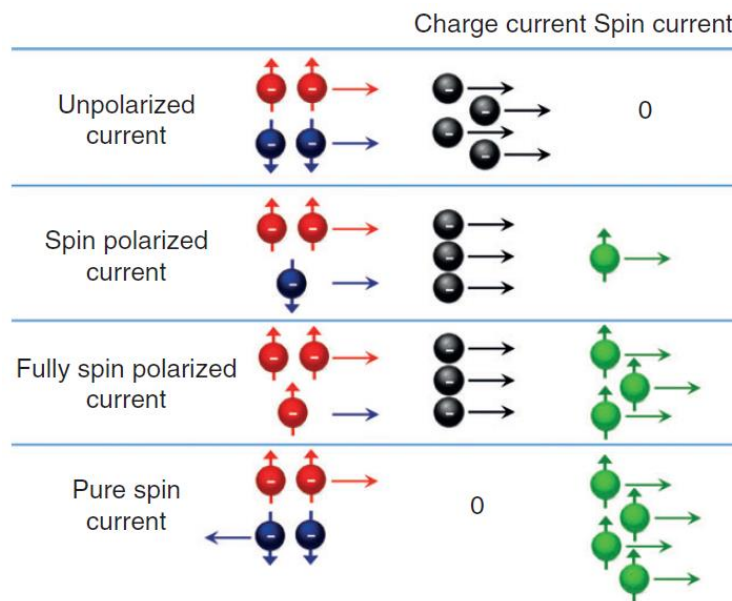
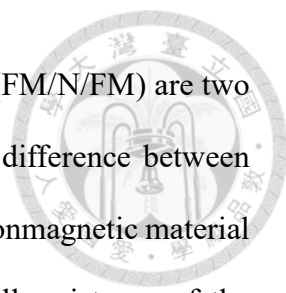


Fig. 1.2 The illustration of the charge and spin current.¹¹



The Magnetic tunnel junction (MTJ, FM/I/FM) and spin valve (FM/N/FM) are two important structures for the spintronic memory devices. The main difference between MTJ and spin valve is material of the spacer layer; An insulator and nonmagnetic material (NM) is used in the MTJ and spin valve, respectively.⁷ The overall resistance of the junction depends on the configuration of magnetization for the two adjacent ferromagnetic (FM) layers: parallel (P) and antiparallel (AP) configuration. This phenomenon called as the magnetoresistance (MR) effect, which is called as tunnel magnetoresistance (TMR) in the MTJ structure and giant magnetoresistance (GMR) in the spin valve structure.

In 1975, TMR effect was first measured in Fe/Ge/Pd and Fe/Ge/Co tunnel junction at 4.2K by Julliere.¹² In 1988, GMR was discovered in the three different Fe/Cr(*t*) superlattices by Baibich *et al.*¹³ and the GMR ratio approach to 80% at 4.2K. Furthermore, they found that the magnetic coupling between the adjacent Fe layers is determined by the thickness of Cr layer, shown in Fig. 1.3. After three years later, the GMR effect was first observed in the spin valve structure (NiFe/Cu/NiFe) by Dieny *et al.* and the GMR ratio is more than 4% at room temperature (RT).¹⁴ In 1995, TMR was first measured in CoFe/Al₂O₃/Co at RT by Moodera *et al.* and the TMR ratio is high than 11%.¹⁵

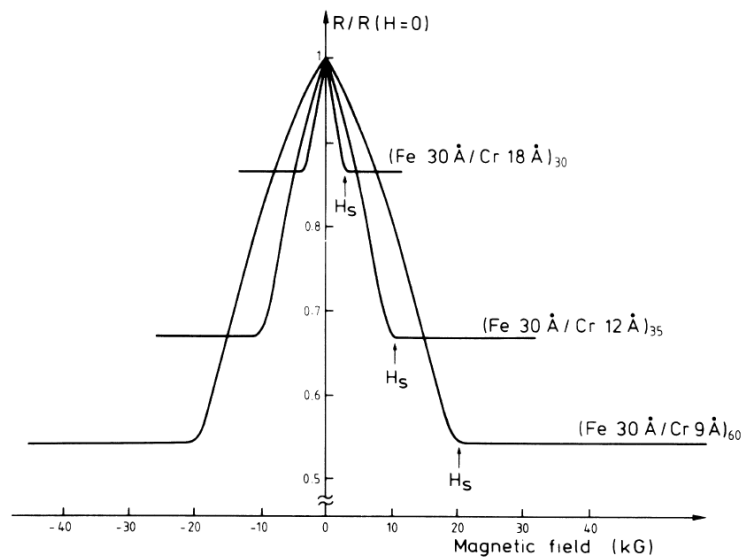


Fig. 1.3 MR of three different Fe/Cr superlattices and the MR ratio is depended on the superlattices structure.¹³

After 1995, the space layer of MTJ was replaced from amorphous Al_2O_3 (Al_2O_3 -MTJ) to single-crystal MgO (MgO-MTJ). Because first-principle predicted that over 1000% TMR ratio can be obtained in an epitaxial MTJ with a crystalline MgO (001) tunnel barrier.¹⁶⁻¹⁸ In 2001, the TMR was first measured in the MgO-MTJ structure by Bowen *et al.*¹⁹ and its ratio (60%) is larger than TMR ratio of Al_2O_3 -MTJ (13%). The important breakthrough came in 2004, over 200% TMR ratio at RT was achieved in CoFe/MgO/CoFe and Fe/MgO/Fe by Parkin *et al.*²⁰ and Yuasa *et al.*²¹, respectively. After four years later, giant TMR ratio at RT as large as 604% has been observed in a MTJ consisting of CoFeB/MgO/CoFeB.^{8,22,23}

1.2 Injection and detection techniques of spin current

The magnetization configuration of MTJ (or spin value) can be switched by two different methods: external magnetic field (H) and spin torque. Since the pure spin current

is without Joule heating during the transport, spin torque is the best choice used to switch the magnetization. The spin Hall effect (SHE) and inverse spin Hall effect (ISHE) are the mechanism used to generate and detect spin current, respectively. SHE describes the conversion process of a charge current to a transverse spin current via the spin-orbit interaction (SOI) in the NM without the application of a magnetic field. On the contrary, a spin current can also converse a charge current without the application of charge current and magnetic field, called as ISHE. The schematic diagram of SHE and ISHE are shown in Fig. 1.4 (a) and (b), respectively.^{8,9}

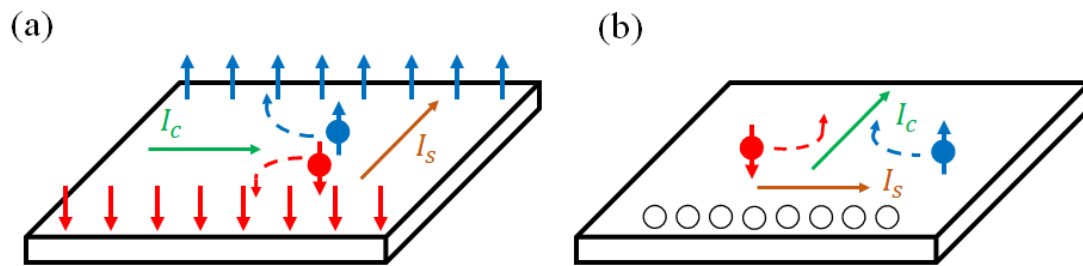


Fig. 1.4 The illustration of (a) spin Hall effect and (b) Inverse spin Hall effect

SHE was predicted theoretically by D'yakonov and Perel' in 1971 and was first measured by Kato *et al.* in 2004.^{24,25} SHE has first been observed in the GaAs and InGaAs thin film by magneto-optical Kerr measurement at 30 K. The opposite electron spin accumulate at the two different edge of the film via SOI and was detected by scanning Kerr rotation measurement. The measurement configuration of Kerr effect and the result are shown in the Fig. 1.5 (a) and (b), respectively. The signal of spin reduces with increasing transverse magnetic field because of spin precession. The Fig. 1.5 (c) shows that the two-dimensional images of spin density and resistivity for GaAs sample.²⁵

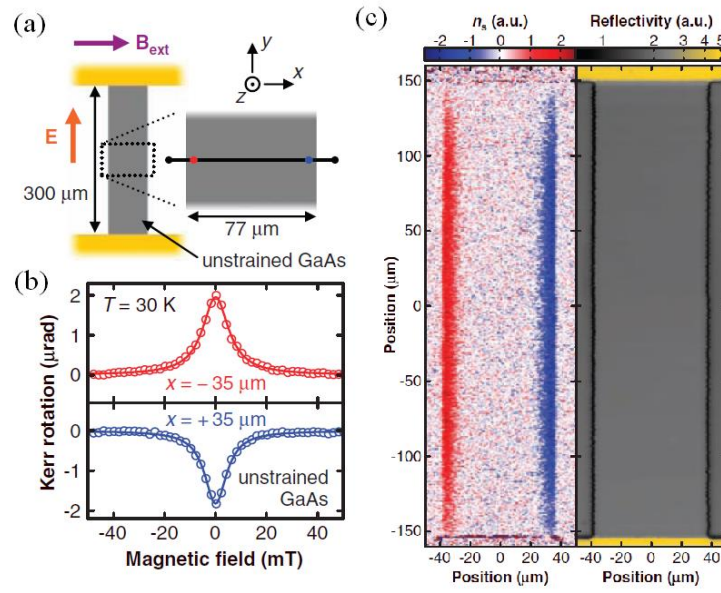


Fig. 1.5 (a) The experimental setup of SHE measurement for GaAs sample. (b) The typical spectra of KR as a function of magnetic field for $x = 35$ and $-35 \mu\text{m}$ and the signal changes sign for the two edges of the sample. (c) Two-dimensional images of spin density and reflectivity for GaAs sample with $E = 10 \text{ mV } \mu\text{m}^{-1}$. This result show that an accumulation of electron spin polarized in the $+z$ ($-z$) at $x = 35$ (-35) μm .²⁵

The Valenzuela *et al.* achieved the direct electrical measurement of SHE in 2006.²⁶ In their experiment, a ferromagnetic/insulator structure (FM/ Al_2O_3) was used to inject spin polarized current in one side of aluminum (Al) Hall cross. The spin polarized current flows into the Al strip and induces a transverse spin-Hall charge imbalance (V_{SH}) via SOI. The two transverse probes are placed at a distance from the spin injector (L_{SH}) and are used to detect the voltage due to SHE (V_{SH}). Fig. 1.6 (a), (b) and (c) show the atomic force microscope image, setup of measurement for SHE and measurement result of R_{SH} , respectively. The results show that R_{SH} linear increase around external magnetic field (B_{\perp}) and saturation at larger external magnetic field (B_{\perp}^{Sat}). The saturation in R_{SH} for $|B_{\perp}| > B_{\perp}^{Sat}$ strongly suggests that the R_{SH} is related to the direction of magnetization

and the SHE. The spin Hall angle of Al was measured in this work and the value about $1-3 \times 10^{-4}$.

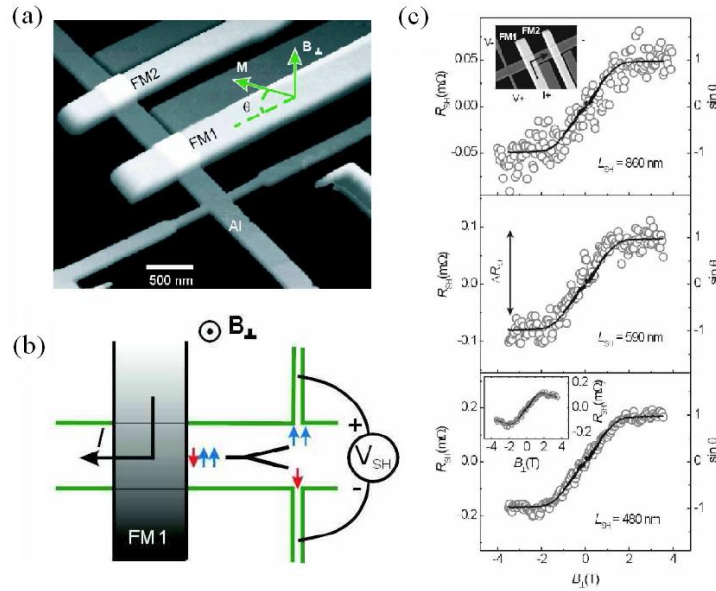


Fig. 1.6 (a) Image of atomic force microscope for device (b) The measurement scheme of SHE measurement (c) Result of R_{SH} vs. B_{\perp} for $t_{Al} = 12$ nm and $L_{SH} = 860$ nm (top), 590 nm (middle) and 480 nm (bottom).²⁶

In the same year, Saitoh *et al.* published that a large ISHE signal was probed in the platinum (Pt)/permalloy (Py) bilayer system by spin pumping technique.²⁷ In their work, ferromagnetic resonance (FMR) serves as an effective spin injector via transferring the angular momentum of magnetization (Py) to conduction electron of adjacent metal (Pt). The pure spin currents are generated at interface and can be detected in the Pt layer via ISHE; called as spin pumping. The setup of measurement and the voltage signals of ISHE (FMR) are shown in Fig. 1.7 (a) and (b), respectively.

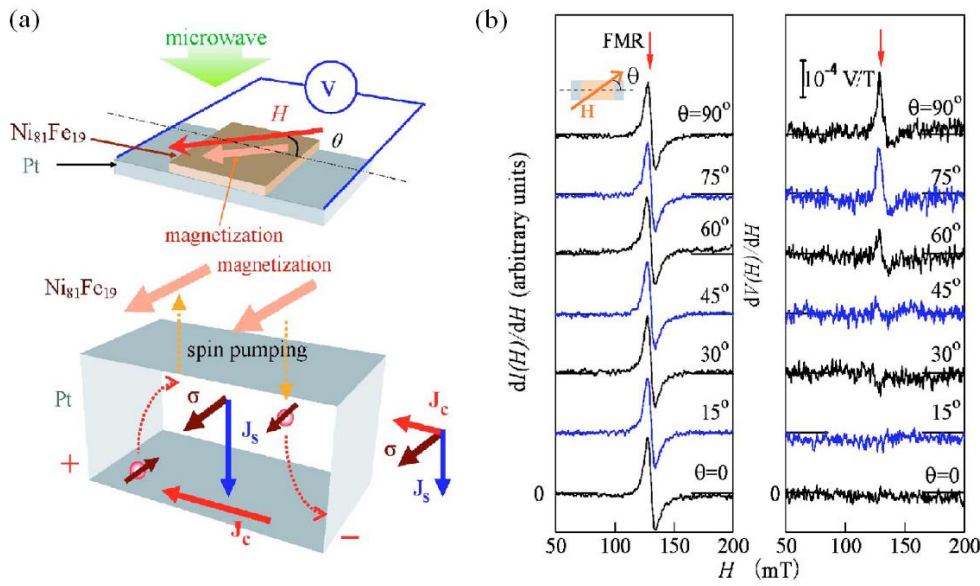


Fig. 1.7 (a) The schematic diagram of spin pumping measurement. (b) The FMR and ISHE spectra of Py/Pt bilayer with different field direction (θ). The signal of ISHE is decrease with changing θ from 90° to 0° ; this result consistent with the relation between j_c and j_s ($j_c \propto \theta_{ISHE} j_s \times \sigma$).²⁷

A different method of generating and detecting the spin current in FM/NM bilayer was proposed by Liu *et al.* in 2011, which is called as spin-torque ferromagnetic resonance (ST-FMR).²⁸ When a microwave-frequency (rf) drives a charge current in the Pt/Py bilayer, an oscillating pure spin current is created in the Pt layer due to SHE. The pure spin current is injected into adjacent Py layer and exerts oscillating spin torque on the magnetization and induce magnetization precession. The precession of magnetization leads to the resistance of the bilayer oscillating with field via anisotropic magnetoresistance (AMR) of Py. A DC voltage generated across the bilayer, including two contributions, one is rf current and other is the oscillating resistance. The schematic circuit for the ST-FMR measurement and the voltage signals of ST-FMR are shown in Fig. 1.8 (a) and (b), respectively. In this work, the spin Hall angle was derived by analysis

the DC voltage signal and the value is 0.067 for Pt layer.

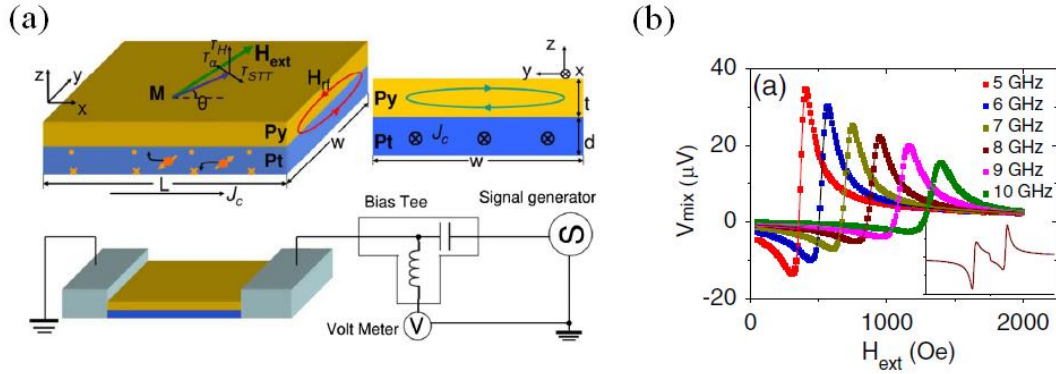


Fig. 1.8 (a) Schematic illustration of the spin transfer torque extra on the magnetization of Py and setup of ST-FMR measurement. The dimension of sample is $20 \mu m$ wide and $110 \mu m$ long. (b) the DC voltage signal of ST-FMR for Pt(6 nm)/Py(4 nm) sample measured under frequencies of 5-10 GHz.²⁸

An important but difficult work is that injection of spin current into the semiconductor (SC); Because SC has been playing an important role for computing and memory devices, ex: Metal-Oxide-Semiconductor field-effect transistor (MOSFET). The impedance mismatch between FM metals and semiconductors severely limits the spin-injection efficiency.^{29,30} Recently, this problem has been solved by the FMR technique. In early 2010, Saitoh's group successfully injected pure spin current into gallium arsenide (GaAs) and silicon (Si).^{29,30} In their study, the various critical parameters, such as inverse spin Hall angle (θ_{ISHE}), spin lifetime (τ_s) and spin diffusion length (λ_s), probed by spin pumping technique. The θ_{ISHE} and τ_s are 1×10^{-4} and 9 ps, respectively, for heavy doping p -Si (concentration $\sim 10^{19}$). Fig. 1.9 (a) and (b) show the setup of measurement and the voltage signals of ISHE, respectively.

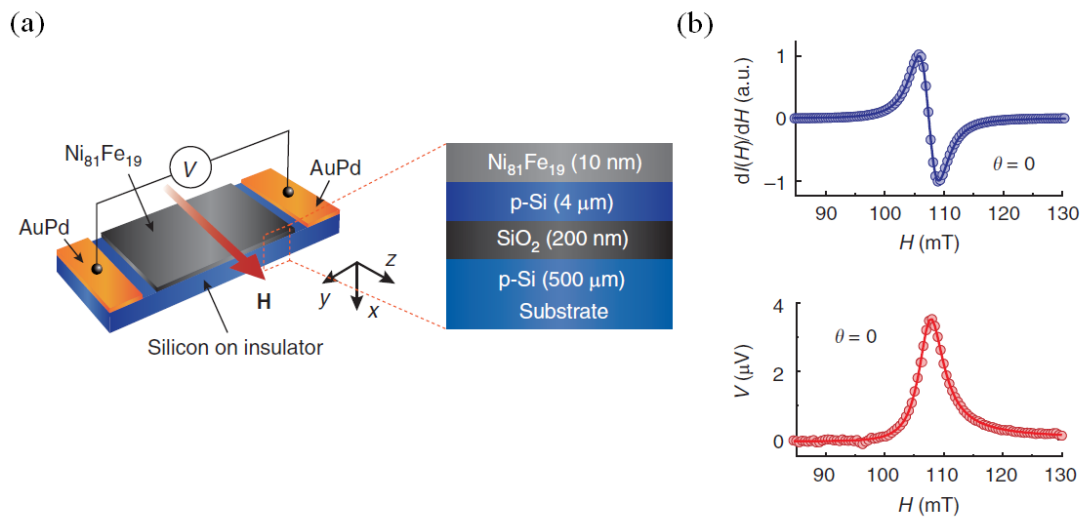


Fig. 1.9 (a) The schematic diagram of the Py/p-Si film. (b) The FMR and ISHE spectra of Py/p-Si film.³⁰

1.3 Types of spintronic devices

The semiconductor transistor is an important and typical charge-based electronic device. Because of the rapid development of chips, the thermal fluctuation-induced noises and energy loss due to Joule heating are the fatal issues while the devices are being miniaturized. Recently, the exploration of spintronic device has attracted great interest owing to their important applications in energy efficient information technology. Instead of transmitting the information by electrical current, the new spintronic technology allows the information being carried by spin current which is without Joule heating during the transport. The spintronic devices can be decomposed into two types due to different transport mechanisms: electron/hole spin and spin/orbit moments, called as Mott- and Dirac-types spintronic devices. The GMR and TMR are important phenomena used in the Mott- types spintronic devices, ex spin memories. On the other hand, spin-orbit

interactions are the fundamental mechanism used in Dirac-types spintronic devices, ex spin transistors.⁸ The summary of Mott- and Dirac-types spintronic devices is listed in the Fig. 1.10. The Magnetoresistive random access memory (MRAM) is typical Mott-types spintronic devices. However, a unit cell of MRAM consists of an MTJ structure and spin-based complementary MOSFET (spin-based MOSFET). The detailed introduction of important spintronic memory devices (MRAM and spin-based MOSFET) shows on next section.^{2,31-33}

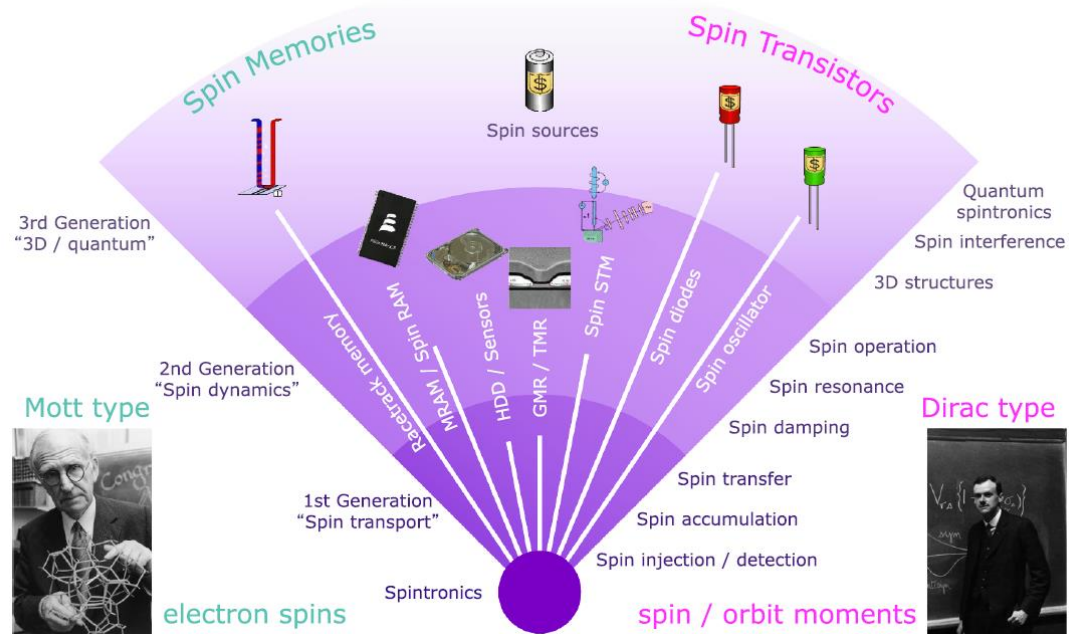


Fig. 1.10 The summary of Mott- and Dirac-types spintronic devices.⁸

1.3.1 Magnetoresistive random access memory (MRAM) device

The MTJ structure is described that a very thin non-magnetic insulator spacer sandwiched between two adjacent FM layers. The overall resistance of MTJ structure depends on the configuration of magnetization. The resistance of MTJ is minimum and

maximum for the P and AP configuration, respectively. This phenomenon can be used on the memory device, called as MRAM. In the MRAM Cell, the magnetization of one of FM layer can be switched, called as free layer (FL), and the magnetization of other is fixed, called as pinned layer (PL). The first MRAM of MTJ was achieved by Wang *et al.* in 1996 and the MTJ of Co/Al₂O₃/NiFi was used in this work.³⁴

In the first generation MRAM (show in Fig. 1.11(a)), The H are induced by a current passing through write word line (WWL) and switch the magnetizations of FL. This method has two main disadvantages: lower efficiency and larger size of cell. However, these problems can be solved in the spin torque based MRAM and it have emerged as the next generation memory technologies.

In the spin torque based MRAM, the methods of magnetization switching can be discriminated by the two different mechanisms: spin transfer torque and spin orbit torque. The Schematic diagram of STT- and SOT-MRAM are display in Fig. 1.11 (b) and (c), respectively. The detail introduction of spin torque based MRAM are shown in the next section.

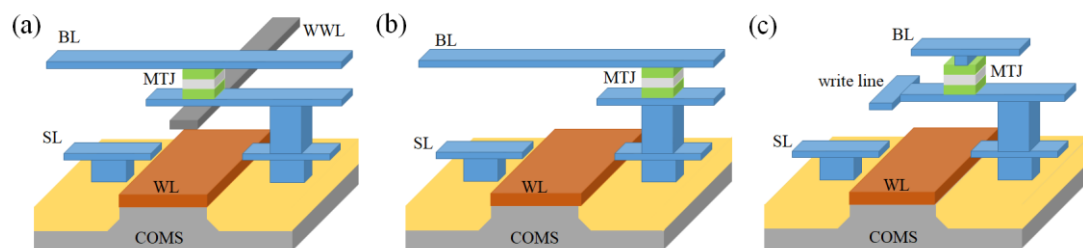


Fig. 1.11 The Schematic diagram of (a) first generation MRAM. The next generation MARAM (b) STT-MRAM and (c) SOT-MRAM.

1.3.2 Spin transfer torque MRAM (STT-MRAM)



The STT effect is described that the spin polarized current is produced by a charge current traversing the first FM layer and exert STT on magnetization during the spin polarized current flowing through second FM layer.

In the STT-MRAM cell, the electrons are applied from PL to FL in the AP to P switching process and the spin polarization is parallel to magnetization of PL after electron flowing through PL. The STT exert on the magnetization of FL and switch the magnetization during electron passing through FL. On the other hand, the electrons are applied from FL to PL in the P to AP switching process and the spin polarization is parallel to magnetization of FL after electron flowing through FL. If the electrons can pass through PL when the spin polarization is parallel with magnetization of PL. However, the electrons with opposite spin polarization are reflected into FL at insulator/PL interface. The reflected electrons if the large in the number, exert the STT on the magnetization of FL and switch the magnetization during electron passing through FL. This result shows that the P to AP switching need a larger energy compared with AP to P counterpart. The illustrate of AP to P switching and P to AP switching process are shown in the Fig. 1.12 (a) and (b), respectively.

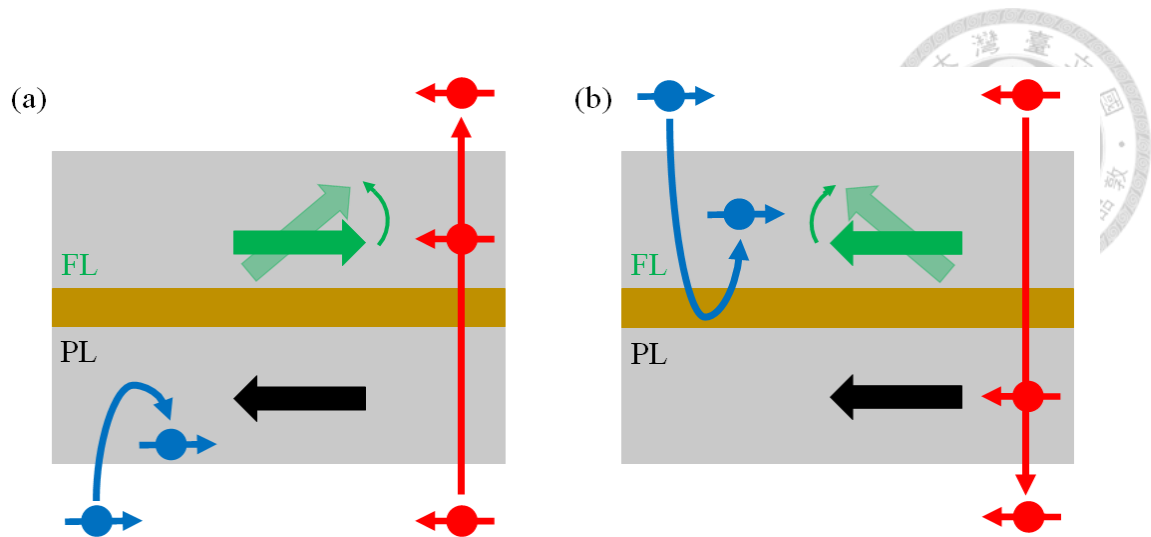


Fig. 1.12 The Schematic diagram of switching magnetization by STT in the MRAM cell.

(a) switch from AP to P (b) switch from AP to P.

1.3.3 Spin orbit torque MRAM (SOT-MRAM)

In the FM/NM bilayer structure, the charge current can be transformed to pure spin current via SOI in the NM layer. The pure spin current can be injected into the FM layer and the SOT are exerted on the magnetization of FM layer. The SOT effect includes two different parts: spin orbit torque [SOT, $\tau_{SO} \propto \hat{M} \times (\hat{\sigma} \times \hat{M})$] and fieldlike torque (FLT, $\tau_{FL} \propto \hat{M} \times \hat{\sigma}$). An illustration of the SOT effects on magnetization is shown in Fig. 1.13.

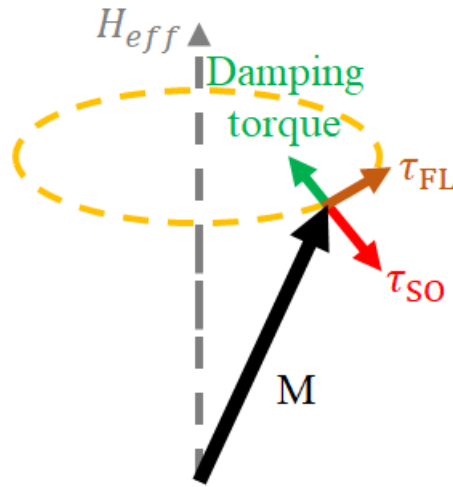


Fig. 1.13 The illustration of the SOT effect on the magnetization. The direction of τ_{SO} is parallel or antiparallel to the damping torque and the τ_{FL} is perpendicular to the damping torque.

In the SOT-MRAM cell, a NM layer is attached at the FL of MTJ structure and the charge current is transformed to spin current via SOI in the NM. The SOT is exerted on the magnetization of FL during the spin current flow into the FL and a sufficient strength SOT can switch the magnetization. The strength of the SOT depends on the magnitude of the current density passing through the NM which implies that the AP to P and P to AP switching can be achieved using a similar current density. The SOT-MRAM is presented to solve the problems in the STT-MRAM, which the reliability issues of read and write performances of the cell. The comparative analysis of STT- and ST-MRAM is shown in the Table 1.1.



Table 1.1 The comparative analysis of STT- and SOT-MRAM.³²

| Parameter | STT-MRAM | SOT-MRAM |
|---------------------------|---------------------|----------|
| Data storage | FL of MTJ structure | |
| Read latency (ns) | 1.2 | 1.13 |
| Write latency (ns) | 11.22 | 1.36 |
| Read energy (pJ) | 260 | 247 |
| Write energy (pJ) | 2337 | 334 |
| Leakage power (mW) | 387 | 254 |
| Features | Non-volatility | |
| | Scalability | |
| | Endurance | |
| | Radiation immune | |

1.3.4 Spin-based Metal-Oxide-Semiconductor field-effect transistor

(Spin-based MOSFET)

The Spin-based MOSFET is a novel MOSFET and the typical spin-based MOSFET is shown in Fig. 1.14.^{7,35,36} The spin-based MOSFET was reported by Sugahara *et al.* in 2004.³⁷ In the spin-based MOSFET call, a FM materials or multilayers contact is placed on source side and the MTJ structure is placed on drain side of MOSFET. If the magnetizations of the FM source and drain are parallel (antiparallel), the channel of transistor is open (closed) and spin current injected from source to SC channel are

transported into (blocked by) the drain.^{7,37-39}

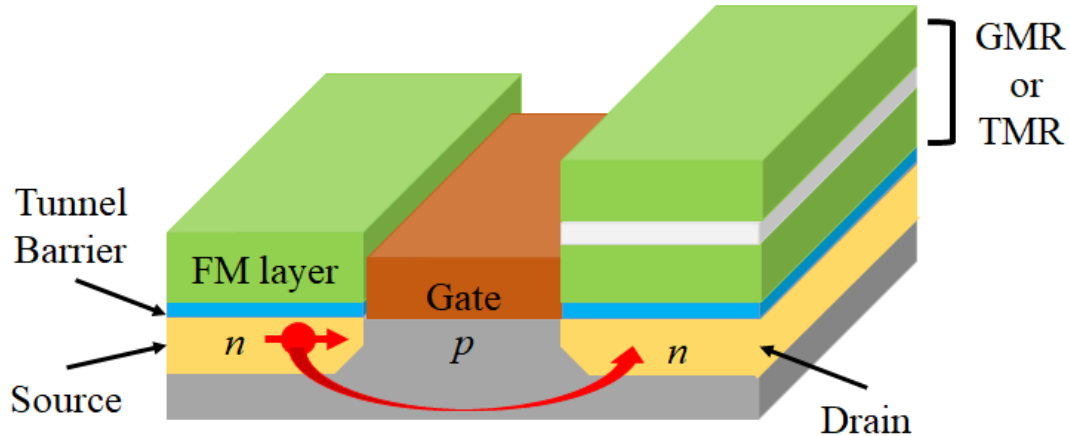


Fig. 1.14 The illustration of spin-based MOSFET. Spin current transport from the source to the drain through a SC channel and the transmission properties of channel can be controlled by applying a voltage bias.

The spin-based MOSFET can be directly coupled with the logic element of the nonvolatile memory element (ex. GMR, MTJ structure), opening up a path to a new kind of logic-in-memory architecture. The MTJ on the drain side stores information via spin current and the information is detected by the output current of the transistor.^{35,40} This device has the advantages such as

1. Nonvolatile storage function
2. Logic functions with CMOS compatibility
3. High endurance and fast write time
4. Low power consumption due to the dramatic reduction of the circuit area

However, several problems have to be resolved in the development of spin-based MOSFET, such as

1. Spin injection and detection at room temperature are difficult for the SC.

2. Effective manipulation and control spin in the SC channel.



1.4 Motivation

Recently, the exploration of spintronic materials especially among semiconductors has attracted great interest owing to their important applications in energy efficient information technology. Instead of transmitting the information by electrical current, the new spintronic technology allows the information to be carried by spin current, which is without Joule heating during the transport. In the due process of spin current transmission, the generation (injection), detection, and control of spin current are the key steps for the practical design in spintronic devices. In addition, SC material has been playing an important role for computing and memory devices, ex: MOSFET. Among various SC materials, Si and GaAs are used because they are two important semiconducting materials for the applications of spintronics due to either long spin lifetime (for Si) or large inverse spin Hall angle (for GaAs) compared to those of other SCs.^{41,42}

In earlier reports, the studies of SC in the field of spintronic have been reported but these results were incomplete. For example, these studies of Si were mainly focused on highly doped *n*-type Si and two methods are used: electron paramagnetic resonance (ESR) and Hanle effect. The results show that the τ_s depends on the doping concentration ($10^{18} < N < 10^{20}$) and doping atom (P, As and Sb) for *n*-type Si.^{43,44} However, using the conventional method, the spin injection from FM into SC is difficult because of the impedance-mismatch problem at the FM/SC interface. Recently, this problem has been solved by the FMR technique. Via FMR-driven spin pumping (FMR-SP), the angular momentum is transferred from the FM layer to conduction electrons of the SC by magnetization precession (dynamic exchange interaction), inducing a pure spin current in

the SC without any net carrier flow. On the other hand, the ISHE is a powerful technique to detect the spin transport signals such as θ_{ISHE} and τ_s . According to the early reports, the spin current is successfully injected into highly doped ($10^{18} < N_d < 10^{19}$) SCs, ex: *n*-GaAs, *p*-GaAs, *p*-Ge, *p*-Si, via FMR-SP.^{29,30,45,46} However, the experimental results on the magnitude and the sign of θ_{ISHE} in the *n*- and *p*-type SCs are rather diversified due to the fact that the dopants in *n*-type and *p*-type are always different.

In this work, cobalt (Co)/SC structure is used to systematically study the behavior of spintronic transport and the dopant effect on spin-orbit interaction in Si and GaAs single crystals, respectively, by FMR-SP and ISHE technique. By applying the proper models, the τ_s value, the λ_s , and the θ_{ISHE} of SC are accurately obtained. The main focus is on the spintronic properties of SC, while the Co layer is used as a spin pumping layer. The Co is chosen as the FM layer because the spin transparency of Co/NM interface is higher than the Py/NM interface.⁴⁷ This thesis contains two parts: (1) Investigation of the behavior of spintronic transport and spin-charge conversion efficiency in Si with different doping concentration and dopants. (2) The dopant effect on spin-orbit interaction in GaAs with different dopants but similar doping concentration.

In part (1), the Co (5 to 40 nm)/Si structure is used to systematically study the behavior of spintronic transport and spin-charge conversion efficiency in Si with different doping concentration and dopants. The Si single crystals with a wide range of doping concentrations from $10^{13} < N < 10^{19}$ and different dopants (B doped for *p*-type and P doped for *n*-type) with similar doping concentration $N \sim 10^{15}$ are used. The primary goal of this study is to obtain the correlation between the doping concentration and spin-charge conversion efficiency in Si, which serves as a guidance to tune the designated properties in Si-based spintronic devices.

In part (2), the Co (5 to 40 nm)/GaAs structures are used to study the dopant effect

on spin-orbit interaction in GaAs system. The GaAs single crystals with different dopants (Zn doped for *p*-type and Si doped for *n*-type) but similar doping concentration are used in this work. The goal of this work is to investigate the magnitude and the sign of θ_{ISHE} of GaAs with different dopant atoms, in order to understand the influence of dopant on the spin-charge conversion in doped SCs, which benefits the future applications of energy-saving spintronic devices.

Chapter 2 Theoretical background



2.1 Quantum description of spin-orbit interaction

The spin-orbit interaction (SOI) is an important mechanism in the fundamental physics and application of spintronics. It can be discussed starting from the Dirac equation. Dirac proposed that the electron of spin could be derived by combining the quantum mechanism and special relativity.^{48,49} The Schrödinger equation is described that an equation of motion particle in the quantum mechanical. The Schrödinger equation is written as⁵⁰

$$i\hbar \frac{\partial}{\partial t} \psi(x, t) = -\frac{\hbar^2}{2m} \nabla^2 \psi(x, t) \quad \text{Eq. 2.1}$$

where \hbar is the Plank constant, $\psi(x, t)$ is the wave function. The energy dispersion relation with considering the special theory of relativity is given as

$$E^2 = c^2 p^2 + m^2 c^4 \quad \text{Eq. 2.2}$$

where p and m is the momentum and the mass of the particle, respectively. The Hamiltonian operator (H) can be described as

$$H = c\alpha p + \beta mc^2 \quad \text{Eq. 2.3}$$

the coefficients α and β should satisfy the following relation

$$\alpha_i^2 = \beta^2 = 1 \quad (i = x, y, z)$$

$$\alpha_i \alpha_j + \alpha_j \alpha_i = 0 \quad (i \neq j) \quad \text{Eq. 2.4}$$

$$\alpha_i \beta + \beta \alpha_i = 0$$

the α and β must be 4×4 matrices for satisfying the relation of Eq. 2.4 and it is called as Dirac realization.

$$\alpha_x = \begin{pmatrix} 0 & 0 & 0 & 1 \\ 0 & 0 & 1 & 0 \\ 0 & 1 & 0 & 0 \\ 1 & 0 & 0 & 0 \end{pmatrix}, \alpha_y = \begin{pmatrix} 0 & 0 & 0 & -i \\ 0 & 0 & i & 0 \\ 0 & -i & 0 & 0 \\ i & 0 & 0 & 0 \end{pmatrix}, \alpha_z = \begin{pmatrix} 0 & 0 & 1 & 0 \\ 0 & 0 & 0 & -1 \\ -1 & 0 & 0 & 0 \\ 0 & -1 & 0 & 0 \end{pmatrix}$$



$$\beta = \begin{pmatrix} 1 & 0 & 0 & 0 \\ 0 & 1 & 0 & 0 \\ 0 & 0 & -1 & 0 \\ 0 & 0 & 0 & -1 \end{pmatrix} \quad \text{Eq. 2.5}$$

The Dirac equation of free particle is obtained

$$i\hbar \frac{\partial}{\partial t} \psi(x, t) = (c\boldsymbol{\alpha} \cdot \mathbf{p} + \beta mc^2) \psi(x, t) \quad \text{Eq. 2.6}$$

The solution of $\psi(x, t)$ has four components because α and β are 4×4 matrices. When the electron is placed in an electromagnetic field, the \mathbf{p} can be substituted by $\mathbf{p} - \frac{e}{c}\mathbf{A}$ and a potential $e\phi$ enter the Eq. 2.6. The Eq. 2.6 can be rewrote as

$$\left[i\hbar \frac{\partial}{\partial t} - c\boldsymbol{\alpha} \cdot \left(\mathbf{p} - \frac{e}{c}\mathbf{A} \right) - \beta mc^2 - e\phi \right] \psi(x, t) = 0 \quad \text{Eq. 2.7}$$

multiplying the operator $\left[i\hbar \frac{\partial}{\partial t} - c\boldsymbol{\alpha} \cdot \left(\mathbf{p} - \frac{e}{c}\mathbf{A} \right) + \beta mc^2 + e\phi \right]$ into the Eq. 2.7 and equation finally form show as

$$\left[\frac{1}{2m} \left(\mathbf{p} - \frac{e}{c}\mathbf{A} \right)^2 + e\phi - \frac{e\hbar}{2mc} \boldsymbol{\sigma} \cdot \mathbf{B} + i \frac{e\hbar}{4m^2c^2} \mathbf{E} \cdot \mathbf{P} - \frac{e\hbar}{4m^2c^2} \boldsymbol{\sigma} \cdot (\mathbf{E} \times \mathbf{P}) \right] \psi(x, t) = W\psi(x, t) \quad \text{Eq. 2.8}$$

In the Eq. 2.8, the first and second terms are due to the Schrödinger equation in the external field. The third and fourth terms are the interaction energy of magnetic dipole and the energy correction of relativity, respectively. Finally, the last term is described the SOI.

2.2 Spin-orbit interaction in the semiconductors

2.2.1 The band structure with spin-orbit interaction

Firstly, we discuss the band structure without SOI for cubic semiconductors. The

conduction band is *s-type* state ($l = 0$) and there is only one state with $m_l = 0$. The valence band is *p-type* state ($l = 1$) and there are three states with $m_l = 0, \pm 1$ (triply degenerate). Moreover, there are two different types of hole in the valence band, the heavy holes ($m_l = \pm 1$) and light holes ($m_l = 0$). Here l is the atomic orbital angular momentum and m_l is its projection on an arbitrary axis.⁵¹

Now, we discuss the band structure with SOI for cubic semiconductors. The addition of spin angular momentum (S) with an orbital angular momentum (L) is important for the atomic physics and the total angular momentum is shown as $J = L + S$. The eigenvalues of J^2 and J_z are $j(j+1)$ with $|l-s| \leq j \leq l+s$ and j_z with $j_z = j, j-1, j-2, \dots, -j$, respectively.

For the conduction band, the value of j is $\frac{1}{2}$, where the values of j_z are $\pm \frac{1}{2}$. This result shows that the conduction band is not affected (spin is $\pm \frac{1}{2}$). For valence band, the values of j are $\frac{1}{2}$ and $\frac{3}{2}$. Moreover, the values of j_z are $\pm \frac{1}{2}$ for $j = \frac{1}{2}$ state and the values of j_z are $\pm \frac{1}{2}$ and $\pm \frac{3}{2}$ for $j = \frac{3}{2}$ state, respectively. The SOI splits the six-fold degeneracy of the valence band at $k = 0$, a four-fold degeneracy for $j = \frac{3}{2}$ state (the heavy and light hole band) and a doubly degeneracy for $j = \frac{1}{2}$ state (the split-off hole band). However, these two state is separated by a *spin-orbit splitting* energy (Δ_{so}) at $k = 0$. The spin of heavy hole, light hole and spin of split-off hole is $\pm \frac{3}{2}$ ($j = \frac{3}{2}$), $\pm \frac{1}{2}$ ($j = \frac{3}{2}$) and $\pm \frac{1}{2}$ ($j = \frac{1}{2}$), respectively. This result shows that the SOI essentially changes energy spectrum of the valence band. Fig. 2.1 shows the Schematic diagram of a direct band-gap structure near $k = 0$ for bulk semiconductor.^{51,52}

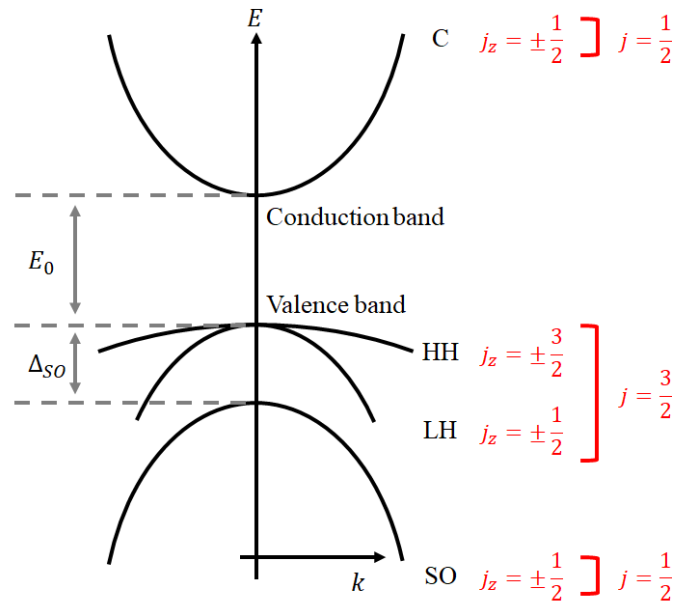


Fig. 2.1 Schematic diagram of a direct band-gap structure near $k = 0$ for bulk semiconductor.

2.2.2 The Spin relaxation in multivalley semiconductor

From earlier experiments of electron paramagnetic resonance (ESR), a salient feature of spin relaxation in n -type Si is a strong dependence on the dopants and doping concentration.⁵³ In the n -type bulk Si, the spin lifetime varies by more than 12 orders of magnitude with changing the doping concentration and temperature.⁵⁴ On the other hand, the spin lifetime is about 2 orders shorter in Sb-doped silicon than in P-doped Si with comparable doping concentration and charge mobility.⁵³ This result is different from the Elliott mechanism for spin relaxation. Fig. 2.2 is shown that the mechanisms of spin relaxation in n -type Si are dependent on doping concentration and temperature. However, a general mechanism was proposed by Hanan Dery group in 2014, which explain the spin relaxation in multivalley materials (ex: Si or GaAs).⁵³

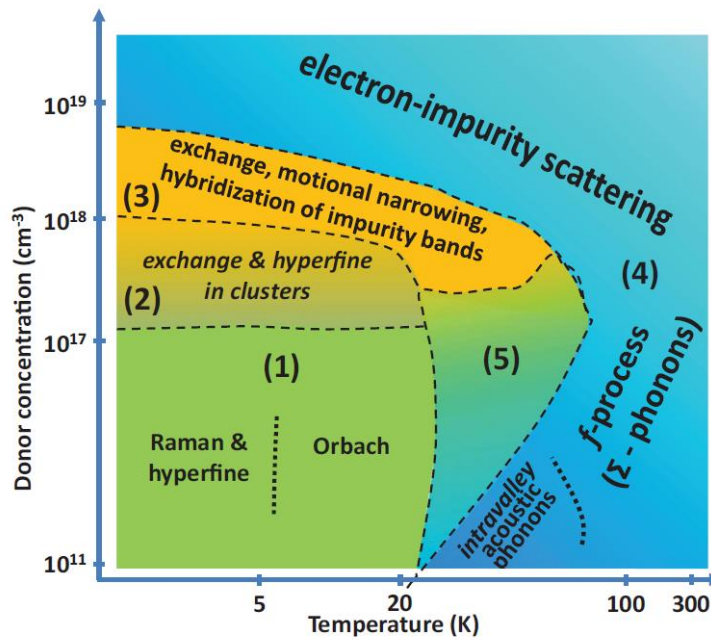


Fig. 2.2 Diagram of dominant spin relaxation mechanisms in *n*-type silicon as a function of doping concentration and temperature.⁵⁴

In this paper, they assume that the short-range potential of impurities governs the strong dopant-dependent spin relaxation in the *n*-type Si material. This effect called as Donor-driven spin relaxation. This effect is dominated by the difference between the potentials of impurity (dopant atoms) and host atoms in the central-cell region, due to SOI within the immediate vicinity of the impurity atomic core.⁵³ Fig. 2.3 (a) shows that an impurity atom is doped in the diamond structure. The impurity atom surrounded by four host atoms in a tetrahedral molecular geometry and it accompany the T_d point-group symmetry. From T_d symmetry and the multivalley of the conduction band, the *f*-process intervalley scattering is the only nonvanishing spin-flip scattering mechanism [i.e., spin flip between two valleys residing on the different crystallographic axes, see Fig. 2.3 (b)]. The left-hand side of Fig. 2.3 (c) shows the energy levels of donor states for Si. The $1s$ state is split into spin-independent nondegenerate (A_1), doubly degenerate (E), triply degenerate (T_2) by valleyorbit coupling with T_d symmetry. The right-hand side of Fig.

2.3 shows that the energy levels are split by SOI. The T_2 is split to fourfold (\bar{F}) and twofold (\bar{E}_2) spin dependent states. Furthermore, the E is split by a small added contribution Δ'_{so} and comes from spin dependent interaction between the \bar{F} state, stemming from E state and T_2 state, respectively.

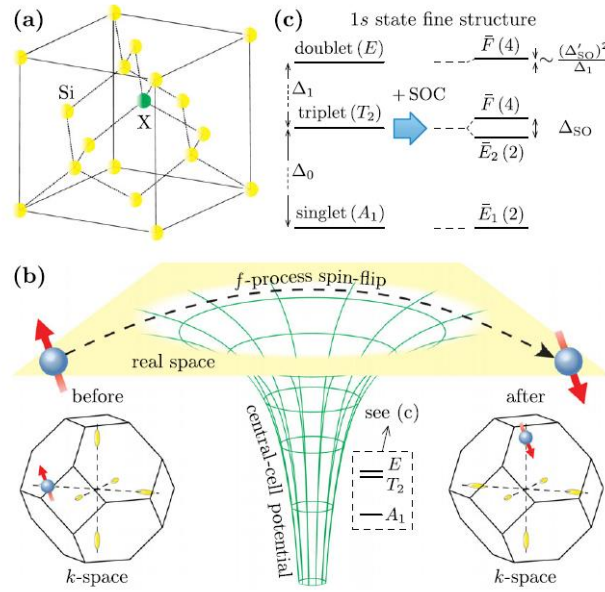


Fig. 2.3 (a) Substitutional impurity atom in a Si crystal host. (b) Scheme of the dominant impurity-driven spin relaxation mechanism (f -process intervalley scattering) (c) Energy levels of donor states for Silicon of the 1s state due to valley-orbit coupling with T_d symmetry.⁵³

The spin relaxation due to scattering off the impurity central-cell potential can be calculated using Δ_{so} and η . The f -process dominant spin-flip scattering amplitude shows as

$$U_s^f = \frac{\pi \alpha_B^3}{V} \left[\frac{i e^{i\theta}}{6} \sin \theta + \frac{\eta(1+i)}{\sqrt{12}} \left(\cos^2 \frac{\theta}{2} - i \sin^2 \frac{\theta}{2} e^{2i\theta} \right) \right] \Delta_{so} \quad \text{Eq. 2.9}$$

where V is the crystal volume, α_B is Bohr radius, Δ_{so} is SOC-induced splitting and

$\eta \equiv \left| \frac{\Delta'_{so}}{\Delta_{so}} \right|$. The polar and azimuthal angles define the spin orientation. The spin-flip amplitude is calculated by assigning $\theta = 0$ and $\phi = \frac{\pi}{2}$, $\theta = \frac{\pi}{2}$ and $\phi = 0$, $\theta = \frac{\pi}{2}$ and $\phi = \frac{\pi}{2}$ for scattering between $\pm x$ and $\pm y$, $\pm z$ and $\pm x$, $\pm z$ and $\pm y$, respectively.

After averaging over all valley configurations and summing over final states, the spin relaxation of a conduction electron with energy ε_k above the band edge is

$$\frac{1}{\tau_s(\varepsilon_k)} = \frac{4\pi N_d V^2}{\hbar (2\pi)^3} \int d^3k' |U_{sf}^f(s)|^2 \delta(E_{k'} - \varepsilon_k) = \frac{4\pi N_d m_e a_B^6}{27\hbar^4} \sqrt{2m_e \varepsilon_k} (6|\eta|^2 + 1) \Delta_{so}^2$$

Eq. 2.10

where N_d is the donor concentration and m_e is the effective mass for electron. The value of Δ_{so} is dependent on both the SC itself and dopant. For example, the Δ_{so} values are 0.03, 0.1, and 0.3 meV for Si doped with P, As, and Sb, respectively, while Δ_{so} is 0.35 meV for GaAs. Fig. 2.4 shows the calculation value of spin lifetime (solid lines) using Eq. 2.10 and it excellently agrees with experiment result (other marks).

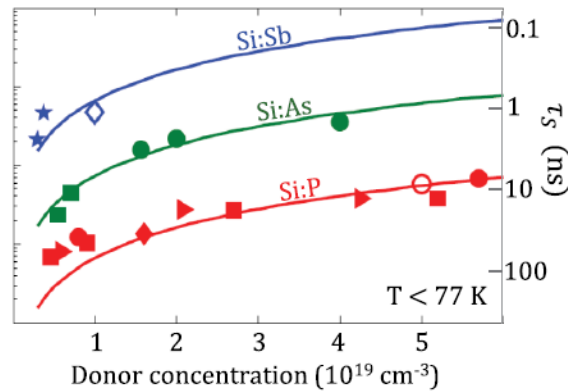


Fig. 2.4 Spin relaxation time in heavily doped *n*-type Si for three common donor type at low temperature. Solid line denotes the theory result and other marks denote experiment results.⁵³



2.3 Spin Hall effect (SHE)

2.3.1 Phenomenological description

The SHE was predicted theoretically by D'yakonov and Perel' in 1971.⁵⁵ The SHE describe that an electric current can generate a transverse spin current via the SOI in the material and the spin polarization is perpendicular to the plane of the two currents.⁵⁵⁻⁵⁷ This phenomenon can be discussed starting from the diffusion equation of charge current and spin current, which shows as⁵⁷

$$\frac{j^c}{e} = \mu n \mathbf{E} + D \nabla n \quad \text{Eq. 2.11}$$

$$\frac{j_{ij}^s}{\hbar} = -\mu n E_i P_j + D \frac{\partial P_j}{\partial x_i} \quad \text{Eq. 2.12}$$

where μ is the electron mobility, \mathbf{E} is the electric field, n is the electron density and D is the electron diffusion constant. The diffusion equation with SOI can be described as

$$\frac{j^c}{e} = \mu n \mathbf{E} + D \nabla n + \theta_{SHE} (\mathbf{E} \times \mathbf{P}) + \theta_{SHE} D (\nabla \times \mathbf{P}) \quad \text{Eq. 2.13}$$

$$\frac{j_{ij}^s}{\hbar} = -\mu n E_i P_j + D \frac{\partial P_j}{\partial x_i} - \varepsilon_{ijk} \left(\theta_{SHE} \mu n E_k + \theta_{SHE} D \frac{\partial n}{\partial x_k} \right) \quad \text{Eq. 2.14}$$

where θ_{SHE} is the spin Hall angle, ε_{ijk} is the unit antisymmetric tensor. The SEH is descried by third term in the Eq. 2.14. Furthermore, the third and fourth terms in the Eq. 2.13 describe the anomalous Hall effect (AHE) and ISHE, respectively. The schematic diagram of spin-dependent Hall effect (AHE, SHE and ISHE) is display in Fig. 2.5. The AHE describes that the charge current generates a transverse spin polarized current via SOI in the magnetic material. The SHE describes that unpolarized charge current generates a transverse pure spin current via SOI in the NM. The ISHE is an inverse process of SHE and it shows that the pure spin current generates a transverse charge current via SOI in the NM.



The θ_{SHE} is the ratio of j_s to j_c and it is described by

$$\theta_{SHE} = \frac{\sigma_{xy}^s}{\sigma_{xx}^c} \frac{e}{h} \quad \text{Eq. 2.15}$$

where $\sigma_{xy}^s = n\hbar\mu\theta_{SHE}$ is the total spin Hall conductivity along transverse direction and $\sigma_{xx}^c = ne\mu$ is the total charge conductivity along longitudinal direction.

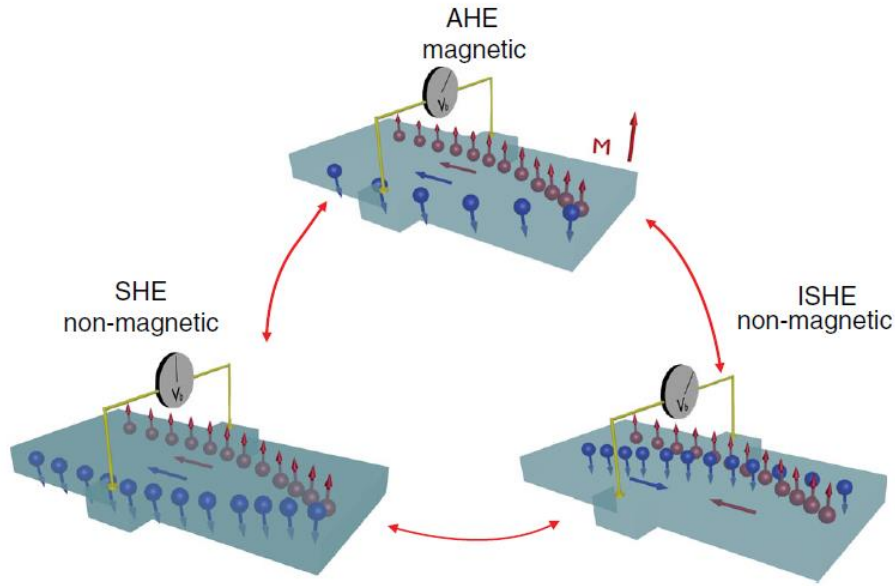


Fig. 2.5 Schematic diagram of spin-dependent Hall effect.⁵⁸

2.3.2 Physical mechanism of spin Hall effect

The spin-dependent Hall effect originates from three different scattering mechanisms: intrinsic, skew scattering and side jump mechanism.⁵⁷⁻⁶⁰ The total spin Hall conductivity can be decomposed into three parts

$$\sigma_{xy}^s = \sigma_{xy}^{s-int} + \sigma_{xy}^{s-skew} + \sigma_{xy}^{s-Side} \quad \text{Eq. 2.16}$$

where σ_{xy}^{s-int} , σ_{xy}^{s-skew} and σ_{xy}^{s-Side} are spin Hall conductivity due to intrinsic, skew scattering and side jump scattering mechanism, respectively. The skew scattering and side jump are called as extrinsic mechanisms and they can be controlled by the SOI of

impurities. The detailed introduction of each mechanisms is as follows

1. Intrinsic mechanism

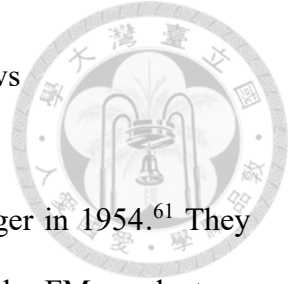
The intrinsic mechanism was proposed by Karplus and Luttinger in 1954.⁶¹ They showed that an anomalous Hall current is generated by the SOI in the FM conductors. Among the three contributions, the intrinsic contribution can be easiest to evaluated. The intrinsic mechanism is due to the SOI on the electric band structure. The value of σ_{xy}^{s-int} is proportional to the spin-orbit polarization at Fermi level $\langle l \cdot s \rangle_{FS}$. The σ_{xy}^{s-int} shown as

$$\sigma_{xy}^{s-int} \approx \frac{e}{4a} \frac{\langle l \cdot s \rangle_{FS}}{\hbar^2} \quad \text{Eq. 2.17}$$

$$l \cdot s = \frac{1}{2} \{j(j+1) - l(l+1) - s(s+1)\}$$

where the a is the lattice constant. The sign of the σ_{xy}^{s-int} is dependence on the sign of $\langle l \cdot s \rangle_{FS}$. According to Hund's rule, the σ_{xy}^{s-int} is expected to be positive for more than half-filling and negative for less than half-filling of the d -bands in the transition metals.^{57,62,63}

From earlier literature report,^{64,65} the σ_{xy}^{s-int} of various transition metals were calculated using the tight binding model. Another one, the θ_{SHE} of various transition metals were detected by spin pumping technique. Their results show that the sign of SHE is positive for Pt (Au) and sign of SHE is negative for Ta (W), as shown in the Fig 2.6 (a) and (b). The sign of SHE depend on the electric band structure and the sign-change is consistent with expected from Eq. 2.17.



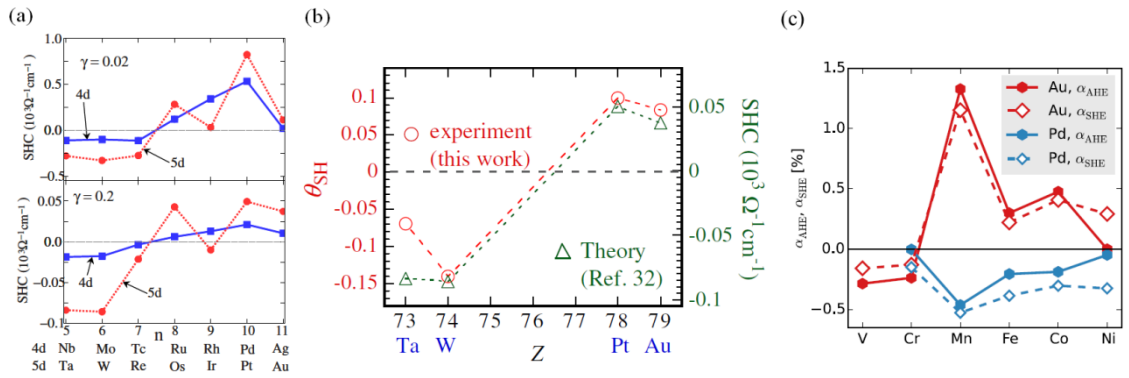


Fig. 2.6 (a) The intrinsic spin Hall conductivity of transition metals are calculated by tight binding mode.⁶⁴ (b) The spin Hall angle of the 5d transition metals are detected by spin pumping technique.⁶⁵ (c) The anomalous Hall angle and the spin Hall angle of nonmagnetic Au and Pd hosts with magnetic 3d impurities from V to Ni.⁶⁶

2. Skew scattering mechanism

The skew scattering mechanism was first proposed by Smit in 1958,⁶⁷ and it originates from Mott scattering in the relativistic physics.⁶⁸ The skew scattering is described as spin-carrier particles scattered asymmetrically by a central potential (effective magnetic field) due to the SOI between host and impurity. The value of σ_{xy}^{S-skew} is proportional to the σ_{xx}^C in the metal.

The SHE due to skew scattering is related to the SOI between the host and impurity. The large SHE can be produced by two different methods: one with the heavy element impurities in the light element hosts (ex. Pt in Cu), and the other with light element impurities in the heavy element hosts (ex. Cu in Pt).⁶⁹ The Fig. 2.6 (c) shows that the skew scattering induces different magnitudes of the anomalous Hall angle (θ_{AHE}) and θ_{SHE} in alloys, based on the nonmagnetic hosts (Au and Pd) with 1% concentration of 3d impurities (Cr, Mn, Fe, Co, and Ni).⁶⁶

3. Side jump mechanism

The side jump mechanism was first proposed by Berger in 1970.⁷⁰ The side jump originates from the different acceleration and deceleration of spin-carrier particles during the scattering with impurities. The contribution of side jumping to the SHE is usually smaller than the intrinsic and the skew scattering contribution. However, the side jumping dominates the SHE at high enough concentrations because the value of σ_{xy}^{s-side} from the side jump is proportional to impurity concentration.⁵⁷ According to experimental reports, if the concentration of the rare earth elements in the gadolinium alloyed system exceeds 5%, the concentration dependence indicates a strong side jump contribution.⁷¹

In general, the SHE cannot be attributed to a single mechanism and several different mechanisms can operate simultaneously.⁵⁹ Fig. 2.7 shows that the mechanism of SHE is depended on the parameter of $\frac{\hbar\tau}{m^*}$, where the τ is spin lifetime, m^* is effective mass.

The $\frac{\hbar\tau}{m^*}$ is directly related to the mobility (μ) and it is approximately equal to 6μ . The

three different ranges can be defined in this picture: (i) $\frac{\hbar\tau}{m^*} < a^2$, call as Dirty (ii) $a^2 \ll$

$\frac{\hbar\tau}{m^*} \ll \frac{a^4}{\lambda_c^2}$, call as Clean (iii) $\frac{a^4}{\lambda_c^2} \ll \frac{\hbar\tau}{m^*}$, call as Ultraclean, where a is effective Bohr radius

and the λ_c^2 is the spin-orbit coupling constant. Firstly, the intrinsic mechanism dominates

in the Clean range. Secondly, the side jump mechanism dominates in the range of $\frac{a^4}{\lambda_c^2} <$

$10^3 \lambda_c^2$. Lastly, the skew scattering mechanism dominates in the range of $10^3 \lambda_c^2 < \frac{a^4}{\lambda_c^2}$. For

example, the a of GaAs is 100 Å and the value of $\frac{a^4}{\lambda_c^2}$ ($\sim 4 \times 10^6 \lambda_c^2$) is much larger than

the $10^3 \lambda_c^2$. This result shows that the SHE of GaAs is dominated by the skew scattering mechanism and the transition from skew scattering to intrinsic by decreasing the mobility.

On the other hand, the a of Pt is 0.5 Å and the value of $\frac{a^4}{\lambda_c^2}$ ($\sim 70 \lambda_c^2$) is much smaller

than the $10^3 \lambda_c^2$. This result shows that the SHE of Pt is dominated by the side jump mechanism and the transition to intrinsic by decreasing the mobility.⁵⁹

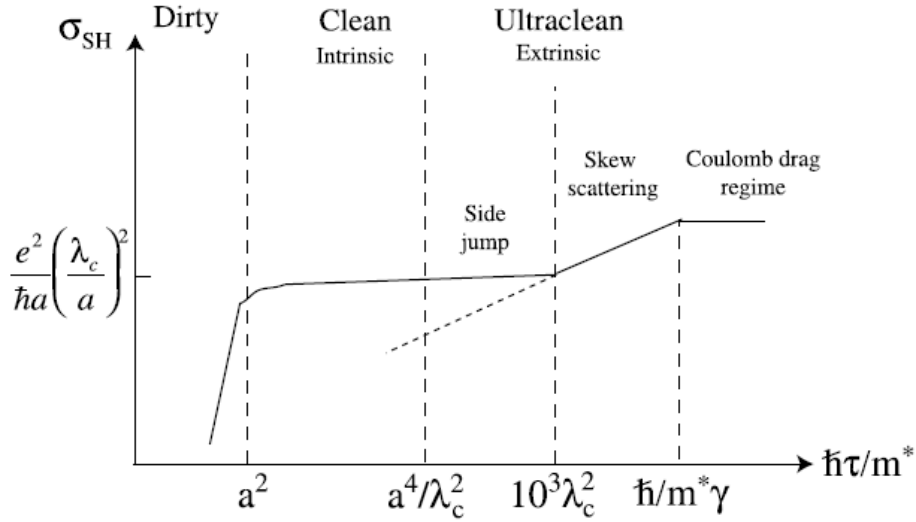


Fig. 2.7 The Schematic diagram of mechanism contribution in the different range and the mechanism of SHE as a function of $\frac{\hbar\tau}{m^*}$. The value of $\frac{\hbar\tau}{m^*}$ is approximately equal to 6 times the value of the mobility.⁵⁹

2.4 Magnetization dynamics and ferromagnetic resonance

(FMR)

Griffiths is the first person who observed the FMR on experiment in 1946.⁷² After one year, the theory of resonance and explained the dynamic behaviors of magnetization in FM materials were proposed by Kittel.⁷³ The FMR is a powerful tool used to analyze the important parameter of FM materials (ex. resonance field, damping constant, effective demagnetization field and etc.).

The magnetization dynamics describes that the precession of magnetic moments

under the influence of effective magnetic fields (\mathbf{H}_{eff}) and the frequency $\omega_0 = \gamma\mu_0 H_r$ at the resonance conditions. The \mathbf{H}_{eff} includes external field (DC and AC H) and internal field (anisotropy, exchange and demagnetization field and etc.). The equation of precession motion first derived by Landau and Lifshitz in the 1935 and as^{2,74-76}

$$\frac{1}{\gamma} \frac{d\mathbf{M}}{dt} = \mathbf{M} \times \mathbf{H}_{eff} \quad \text{Eq. 2.18}$$

when $\gamma = g\mu_B/\hbar$ is gyromagnetic ratio, g is g -factor, μ_B is Bohr magneton number, \hbar is Plank constant. This equation shows that the magnetization keeps a precession around effective field (equilibrium axis). This result is not consistent with experimental results because the magnetization aligns with the equilibrium axis after a finite time. According to it, an additional damping term is needed to support experimental results. However, a time-dependent Landau-Lifshitz equation was reformulated by Gilbert in 1955 and call as Landau-Lifshitz-Gilbert (LLG) equation.

$$\frac{1}{\gamma} \frac{d\mathbf{M}}{dt} = \mathbf{M} \times \mathbf{H}_{eff} + \frac{\alpha}{M} \left(\mathbf{M} \times \frac{d\mathbf{M}}{dt} \right) \quad \text{Eq. 2.19}$$

when α is damping constant. The damping behavior is described by second term at right hand side and call as Gilbert damping parameter. The damping effect leads to the magnetization moves toward and finally align with the equilibrium axis. Fig. 2.8 (a) is shows that an illustration of the magnetization precession with a damping effect.

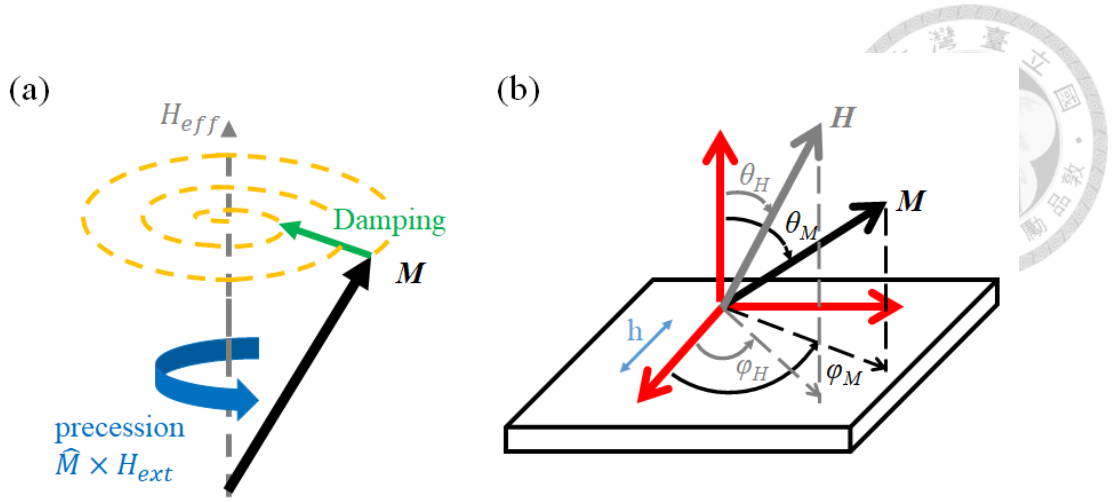


Fig. 2.8 (a) The illustration of the magnetization precession with a damping effect. (b) The configuration of coordinate system for thin film.

The sample absorbs the energy from the transverse microwave and the magnetizations make a precession around the equilibrium axis at resonant condition during the measurement of FMR spectra. In the thin film system, the behavior of precession can be described by the LLG equation and the free energy includes Zeeman energy (E_{zee}), demagnetization energy (E_d), perpendicular anisotropy energy (E_{perp}). The total free energy per unit volume of magnetization can be written as⁷⁷

$$E = E_{zee} + E_d + E_{perp} \quad \text{Eq. 2.20}$$

$$E = -\mathbf{M}_s \mathbf{H} [\sin \theta_H \sin \theta_M \cos(\varphi_H + \varphi_M) + \cos(\theta_H + \theta_M)] + 2\pi \mathbf{M}_s^2 \cos^2 \theta_M - K_{\perp} \cos^2 \theta_M \quad \text{Eq. 2.21}$$

which \mathbf{H} , \mathbf{M}_s is saturation magnetization, K_{\perp} is perpendicular anisotropy constant. The coordinate of thin film system is shown in Fig. 2.8 (b). The resonance condition can be used to determine the resonance frequency and field, which is generally given by

$$\left(\frac{\omega}{\gamma}\right)^2 = \frac{1}{(M_s \sin \theta_M)^2} (E_{\theta_M \theta_M} E_{\varphi_M \varphi_M} - E_{\theta_M \varphi_M}^2) \quad \text{Eq. 2.22}$$

when E_{ij} is the partial derivative of E. The θ_M on resonance can be given by $\frac{\partial E}{\partial \theta_M} = 0$

and $\frac{\partial E}{\partial \varphi_M} = 0$ and show as

$$2H_r \sin(\theta_H - \theta_M) + 4\pi M_s \sin 2\theta_M = 0 \quad \text{Eq. 2.23}$$

$$4\pi M_{eff} = 4\pi M_s + \frac{2K_{\perp}}{M_s t_{FM}}$$

when H_r is resonance field, t_{FM} is thickness of FM layer and $4\pi M_{eff}$ is effective demagnetization field. A simplified resonance condition is obtain by deducing E_{ij} from Eq. 2.21; express as

$$\left(\frac{\omega}{\gamma}\right)^2 = H_1 \times H_2 \quad \text{Eq. 2.24}$$

$$H_1 = [H_r \cos(\theta_H - \theta_M) - 4\pi M_{eff} \cos^2 \theta_M]$$

$$H_2 = [H_r \cos(\theta_H - \theta_M) - 4\pi M_{eff} \cos 2\theta_M]$$

the H_r as a function of θ_H and can be calculated using Eq. 2.23 and Eq. 2.24 with $4\pi M_{eff}$ and g-factor.

The total linewidth (ΔH_{pp}) of FMR spectrum is the contribution from the two different mechanisms: homogeneities damping (ΔH_{pp}^{hom}) and inhomogeneities damping (ΔH_{pp}^{inhomo}). The ΔH_{pp} mainly comes from ΔH_{pp}^{hom} in the FMR experiment.

The ΔH_{pp}^{hom} can be described as

$$\Delta H_{pp}^{hom} = \frac{1}{\sqrt{3}} \alpha (H_1 + H_2) \left| \frac{d(\frac{\omega}{\gamma})}{dH_r} \right|^{-1} \quad \text{Eq. 2.24}$$

On the other hand, the ΔH_{pp}^{inhomo} is approximately expressed as

$$\Delta H_{pp}^{inhomo} = \Delta H_r^{4\pi M_{eff}} + \Delta H_r^{\theta_H} = \left| \frac{dH_r}{d(4\pi M_{eff})} \right| \Delta(4\pi M_{eff}) + \left| \frac{dH_r}{d\theta_H} \right| \Delta\theta_H \quad \text{Eq. 2.25}$$

when $\Delta(4\pi M_{eff})$ and $\Delta\theta_H$ are the distribution of $\Delta(4\pi M_{eff})$ and $\Delta\theta_H$, respectively.

If the inhomogeneities damping can be negligible in the thin film, the α can be derived from the linewidth and is gave by the simplified formula

$$\Delta H_{pp} = \frac{2\omega}{\sqrt{3}\gamma} \alpha$$



2.5 Phenomenological model of Spin pumping



2.5.1 Spin pumping and inverse spin Hall effect (ISHE)

The generation (injection), detection, and control of spin current are the key steps for the practical function in devices, for example, magnetic memory and spin-based MOSFET. The FMR-SP is a technique for generating spin current in a FM/ NM bilayer structure and could be operated under the FMR condition.⁷⁸ The angular momentum is transferred from magnetization to conduction electron by magnetization precession (dynamic exchange interaction) and induce a pure spin current in the adjacent NM layer without any net carrier flow. The ISHE is a powerful tool used to detection of pure spin current, called as ISHE-probe because the pure spin current can be converted to a transverse charge current via ISHE. The relation between spin current density (j_s) and charge current density (j_c) can be written as²⁷

$$j_c \propto \theta_{ISHE} j_s \times \sigma \quad \text{Eq. 2.26}$$

when the σ is spin polarization vector of spin current and it is parallel to the direction of the \mathbf{H} . In early reports on FM/NM bilayers, researchers have used Co, Ni, Fe, Py, Fe₃O₄, LSMO, and so on, as the FM layer and 4d or 5d transition metals as the NM layer because of their strong SOI.^{27,79-81} Fig. 2.9 (a) is shown that Schematic diagram of spin pumping under the FMR condition.

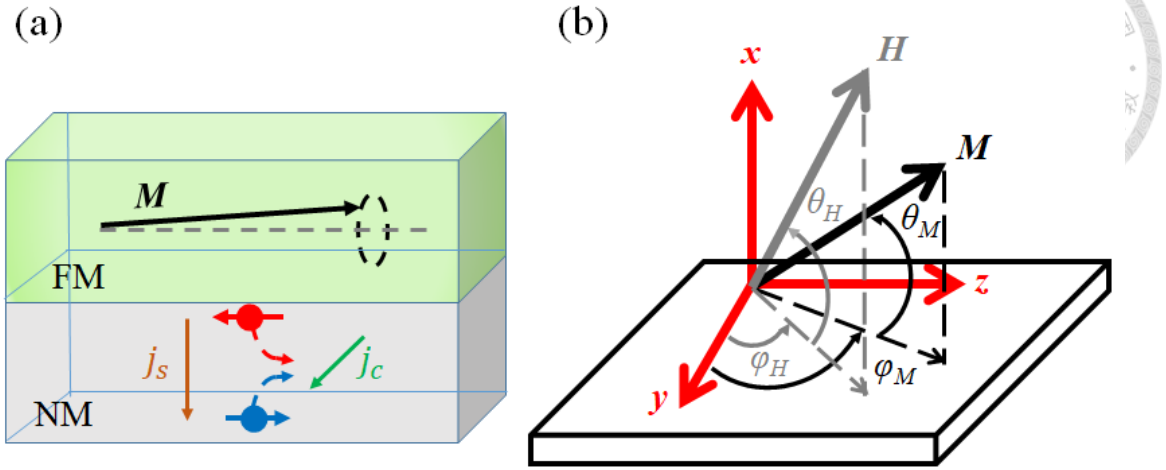


Fig. 2.9 (a) The schematic diagram of spin pumping under the FMR condition. (b) The schematic illustration of the coordinate system.

The spin pumping theoretical models were proposed by Arne Brataas in 2002.^{82,83} In the spin pumping system, the spin current emission deprives the magnetization of angular momentum and enhance the magnetization-precession damping.⁷⁸ The dynamic of magnetization can be described by LLG equation^{78,84}

$$\frac{d\mathbf{M}(t)}{dt} = -\gamma \mathbf{M}(t) \times \mathbf{H}_{eff} + \frac{\alpha}{M_s} \mathbf{M}(t) \times \frac{d\mathbf{M}(t)}{dt} + \frac{\gamma}{v} I_s \quad \text{Eq. 2.27}$$

where γ , α and v are the gyromagnetic ratio, damping constant, and volume of FM respectively. The Schematic diagram of the coordinate system is shown in Fig. 2.9 (b). The I_s is spin current due to spin pumping effect and the spin current density at interface (j_s^0 , I_s divides by interface area) is described as

$$j_s^0 = \frac{\omega}{2\pi} \int_0^{2\pi/\omega} \frac{\hbar}{4\pi} g_{eff}^{\uparrow\downarrow} \frac{1}{M_s^2} \left[\mathbf{M}(t) \times \frac{d\mathbf{M}(t)}{dt} \right]_z dt \quad \text{Eq. 2.28}$$

where ω , $g_{eff}^{\uparrow\downarrow}$ and M_s are the precession frequency of magnetization, the effective spin mixing conductance and saturation magnetization of FM layer, respectively. The $\left[\mathbf{M}(t) \times \frac{d\mathbf{M}(t)}{dt} \right]_z$ is the z component of $\mathbf{M}(t) \times \frac{d\mathbf{M}(t)}{dt}$, which is directed along the axis of the processed magnetization. The $g_{eff}^{\uparrow\downarrow}$ is described as the spin pumping efficiency and

the value of $g_{eff}^{\uparrow\downarrow}$ can be extracted from variation of damping constant ($\Delta\alpha$).^{82,83}

$$g_{eff}^{\uparrow\downarrow} = \frac{4\pi M_s}{\gamma\hbar} t_{FM} \Delta\alpha = \frac{4\pi M_s}{\gamma\hbar} t_{FM} (\alpha_{FN} - \alpha_F) \quad \text{Eq. 2.29}$$

where t_{FM} is the thickness of FM.

At an equilibrium condition ($\mathbf{M}(t) \times \mathbf{H}_{eff} = 0$), the \mathbf{H}_{eff} includes \mathbf{H} and the static demagnetizing field (\mathbf{H}_D) for soft FM thin film. The \mathbf{H} and \mathbf{H}_D are shown as

$$\mathbf{H} = H \begin{pmatrix} 0 \\ \cos(\theta_M - \theta_H) \\ \sin(\theta_M - \theta_H) \end{pmatrix} \quad \text{Eq. 2.30}$$

$$\mathbf{H}_D = -4\pi M_s \cos \theta_M \begin{pmatrix} 0 \\ \cos \theta_M \\ \sin \theta_M \end{pmatrix} \quad \text{Eq. 2.31}$$

where θ_H and θ_M are angle between the external magnetic field and magnetization to film plane, respectively. The relation of θ_H and θ_M is shown as

$$2H \sin(\theta_H - \theta_M) + 4\pi M_s \sin 2\theta_M = 0 \quad \text{Eq. 2.32}$$

At a precession condition ($\mathbf{M}(t) \times \mathbf{H}_{eff} \neq 0$), the magnetization makes a processes around the equilibrium axis. The \mathbf{H}_{eff} and time dependent magnetization ($\mathbf{M}(t)$) are described by

$$\mathbf{H}_{eff}(t) = \mathbf{H} + \mathbf{H}_D + \mathbf{H}_D(t) + \mathbf{h}(t) \quad \text{Eq. 2.33}$$

$$\mathbf{M}(t) = \mathbf{M} + \mathbf{m}(t) \quad \text{Eq. 2.34}$$

$$\mathbf{H}_D(t) = -4\pi m_y(t) \sin \theta_M \begin{pmatrix} 0 \\ \cos \theta_M \\ \sin \theta_M \end{pmatrix} \quad \text{Eq. 2.35}$$

$$\mathbf{h}(t) = \begin{pmatrix} h e^{i\omega t} \\ 0 \\ 0 \end{pmatrix} \quad \text{Eq. 2.36}$$

$$\mathbf{m}(t) = \begin{pmatrix} m_x e^{i\omega t} \\ m_y e^{i\omega t} \\ 0 \end{pmatrix} \quad \text{Eq. 2.37}$$

where $\mathbf{H}_D(t)$, $\mathbf{h}(t)$ and ω are dynamic demagnetizing field induce by $\mathbf{m}(t)$, external AC field and $\omega = 2\pi f$, respectively. The FMR condition is shown

$$\left(\frac{\omega}{\gamma}\right)^2 = H_1 \times H_2$$



Eq. 2.38

$$H_1 = [H_r \cos(\theta_H - \theta_M) - 4\pi M_{eff} \cos^2 \theta_M]$$

$$H_2 = [H_r \cos(\theta_H - \theta_M) - 4\pi M_{eff} \cos 2\theta_M]$$

the dynamic components of magnetization $\mathbf{m}(t)$ in FMR condition are extracted by solving Eq. 2.27 combined with Eq. 2.30, Eq. 2.31, Eq. 2.33 and Eq. 2.35. The $\mathbf{m}(t)$ shown as

$$m_y(t)$$

$$= \frac{4\pi M_s \gamma h_{rf} \{2\alpha\omega \sin \omega t + [4\pi M_s \gamma \cos^2 \theta_M + \sqrt{(4\pi M_s)^2 \gamma^2 \cos^4 \theta_M + 4\omega^2}] \cos \omega t\}}{8\pi\alpha\omega \sqrt{(4\pi M_s)^2 \gamma^2 \cos^4 \theta_M + 4\omega^2}}$$

Eq. 2.39

$$m_x(t) = -\frac{4\pi M_s \gamma h_{rf} \cos \omega t}{4\pi\alpha \sqrt{(4\pi M_s)^2 \gamma^2 \cos^4 \theta_M + 4\omega^2}}$$

Eq. 2.40

Using Eq. 2.28, Eq. 2.39 and Eq. 2.40, the spin current density at interface show as

$$j_s^0 = \frac{g_r^{\uparrow\downarrow} \gamma^2 h_{rf}^2 [4\pi M_s \gamma \cos^2 \theta_M + \sqrt{(4\pi M_s)^2 \gamma^2 \cos^4 \theta_M + 4\omega^2}]}{8\pi\alpha^2 [(4\pi M_s)^2 \gamma^2 \cos^4 \theta_M + 4\omega^2]}$$

Eq. 2.41

the j_s^0 is injected from the FM layer into NM layer and it decays along the x direction due to spin relaxation as

$$j_s(x) = \frac{\cosh\left(\frac{d_N - x}{\lambda_s}\right)}{\coth\left(\frac{d_N}{\lambda_s}\right)} j_s^0 \quad \text{Eq. 2.42}$$

where $j_s(x)$, d_N and λ_s are spin current density in NM layer, the thickness and spin diffusion length of NM layer, respectively.

The j_s is converted into a j_c via ISHE as

$$\mathbf{j}_c = \theta_{ISHE} \left(\frac{2e}{\hbar}\right) \mathbf{j}_s \times \boldsymbol{\sigma} \quad \text{Eq. 2.43}$$

using Eq. 2.42 and Eq. 2.43, the average charge current defined as

$$\langle j_c \rangle = \left(\frac{1}{t_N} \right) \int_0^{t_N} j_c(y) dy$$

$$\langle j_c \rangle = \theta_{ISHE} \left(\frac{2e}{\hbar} \right) \left(\frac{\lambda_s}{t_N} \right) \tanh \left(\frac{t_N}{2\lambda_s} \right) j_s^0 \quad \text{Eq. 2.44}$$



after considering the geometry, we obtain the voltage and charge current generated by ISHE in the NM layer as

$$V_{ISHE} = \frac{\theta_{ISHE} w \lambda_s}{d_N \sigma_N + d_F \sigma_F} \left(\frac{2e}{\hbar} \right) \tanh \left(\frac{t_N}{2\lambda_s} \right) j_s^0 \quad \text{Eq. 2.45}$$

$$I_c = \theta_{ISHE} w \left(\frac{2e}{\hbar} \right) \lambda_s \tanh \left(\frac{t_N}{2\lambda_s} \right) j_s^0 \quad \text{Eq. 2.46}$$

according to the Eq. 2.46, Eq. 2.41 and Eq. 2.29, the value of I_c is dependent on t_{FM} and the θ_{ISHE} can be extracted by fitting the thickness-dependence data of I_c . Lastly, the angular-dependence data of voltage [$V_{ISHE}(\theta)$] is obtained by Eq. 2.26 and Eq. 2.41. The Eq. 2.26 show that the $V_{ISHE}(\theta)$ is proportional to $j_s \cos \theta_M$ and the $V_{ISHE}(\theta)$ are described by

$$V_{ISHE}(\theta) \propto \frac{g_r^{\uparrow\downarrow} \gamma^2 h_{rf}^2 \cos \theta_M [4\pi M_s \gamma \cos^2 \theta_M + \sqrt{(4\pi M_s)^2 \gamma^2 \cos^4 \theta_M + 4\omega^2}]}{8\pi \alpha^2 [(4\pi M_s)^2 \gamma^2 \cos^4 \theta_M + 4\omega^2]}$$

Eq. 2.47

2.5.2 Spin precession

Spin precession is a phenomenon that the spin makes a precession around the direction of the magnetic field and gradually relax during precession time. This phenomenon is observed in long spin lifetime material and has been discussed in the spin device with a FM/SC interface.^{29,30,85}

In the resonance condition with \mathbf{H} applying oblique to the film plane (the schematic diagram is shown in Fig. 2.10, the pure spin current is injected into the SC layer and the spin polarization vector is parallel to precession axis of magnetization. Consequently, the

free spins in SC make a precession around the axis parallel to H and gradually relax back to a static state after some time, as called the spin lifetime.

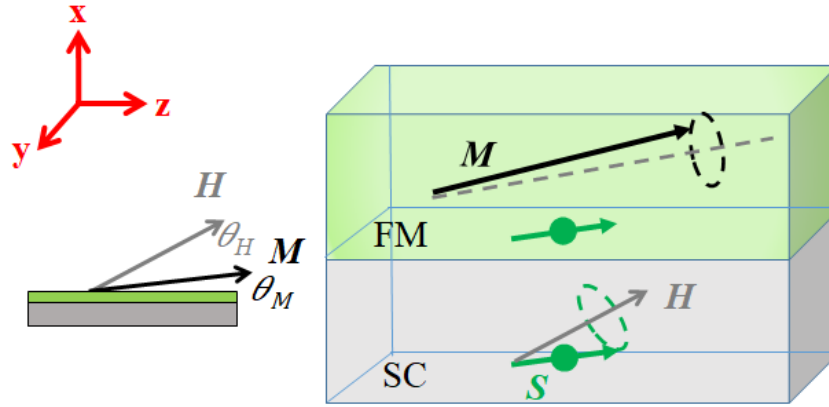


Fig. 2.10 The Schematic diagram of spin precession under the FMR condition.

In the FM/SC spin pumping system, the spin precession of free spin in SC layer can be described by Bloch equation with spin diffusion model³⁰

$$\frac{\partial m(x,t)}{\partial t} = -\gamma[m(x,t) \times H] - \frac{m(x,t)}{\tau_s} + D_N \nabla^2 m(x,t) + 2(j_{s,x}^x e_x + j_{s,x}^z e_z) \delta(x)$$

Eq. 2.48

where $m(x,t)$ is the magnetization of carriers, γ is gyromagnetic ratio, τ_s and D_N are the spin lifetime and diffusion constant of carriers, respectively, in the SC. The $j_{s,p}^p$ is the spin current density with the spin polarization vector p and flow direction q at $x=0$. The $\delta(x)$ is delta function. The $j_{s,x}^x = -j_s \sin \varphi$ and $j_{s,x}^z = -j_s \cos \varphi$ in our measurement. By solving the Eq. 2.48 for equilibrium condition ($\frac{\partial m(x,t)}{\partial t} = 0$), the spin current density is shown as

$$\begin{bmatrix} j_{s,x}^x e_z \\ j_{s,x}^y e_z \\ j_{s,x}^z e_z \end{bmatrix} = \begin{bmatrix} -j_s^0 \sin \theta \cos(\theta_H - \theta_M) e^{-x/\lambda_s} + j_s \cos \theta \sin(\theta_H - \theta_M) \text{Re}(e^{-x/\lambda_\omega}) \\ -j_s^0 \sin(\theta_H - \theta_M) \text{Im}(e^{-x/\lambda_\omega}) \\ j_s^0 \cos \theta \cos(\theta_H - \theta_M) e^{-x/\lambda_s} + j_s \sin \theta \sin(\theta_H - \theta_M) \text{Re}(e^{-x/\lambda_\omega}) \end{bmatrix}$$

Eq. 2.49

where j_s^0 is spin current density at FN/NM interface (Eq. 2.41).

According to theory of spin pumping ($j_c \propto j_s \times \sigma$), a y-axis charge current is induced by an x-axis spin current with z-axis polarization ($j_{s,x}^z$) and the $V_{ISHE}(\theta)$ is obtained by

$V_{ISHE} \propto \int_0^{t_{sc}} j_{s,x}^z(x) dx$, show as

$$V_{ISHE}(\theta) = A \times j_s^0 \times \left[\cos \theta_H \cos(\theta_H - \theta_M) \int_0^{t_{sc}} e^{-x/\lambda_s} dx + \sin \theta_H \sin(\theta_H - \theta_M) \int_0^{t_{sc}} e^{-x/\lambda_\omega} dx \right]$$

Eq. 2.50

where A is a constant, $\lambda_s = \sqrt{D_N \tau_s}$ is spin diffusion length, $\lambda_\omega = \frac{\lambda_s}{\sqrt{1+i\omega_L \tau_s}}$, $\omega_L = \gamma_c H_{FMR}$ and the t_{sc} is thickness of SC. From literature report, the normal value of $V_{ISHE}(\theta)$ is dependence on τ_s and the calculation values of $V_{ISHE}(80^\circ)$ with different τ_s are show in the Fig. 2.11 These results show that the spin precession is one method using to detected spin lifetime in FM/SC spin pumping system.³⁰

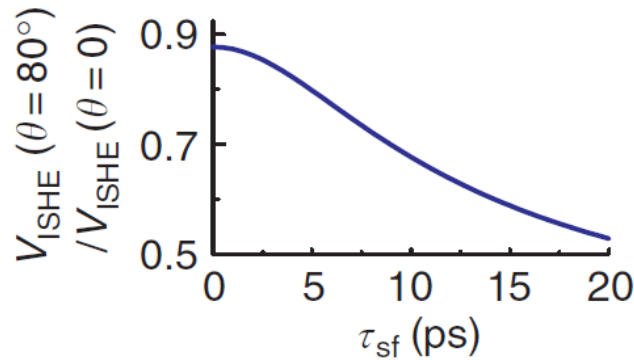


Fig. 2.11 The calculation values of $V_{ISHE}(80^\circ)$ with different τ_s .³⁰

Chapter 3 Experimental techniques



3.1 Magnetron Sputtering

3.1.1 Principle of sputtering

In this work, the cobalt (Co) and platinum (Pt) thin film is deposited using the magnetron sputtering system and the introduction of the magnetron sputtering system will be discussed in this section. The sputter techniques are widely used to deposit thin film and the advantage is exhibited as⁸⁶⁻⁸⁸

1. In principle, any vacuum-compatible material can be deposited by this sputtering process with a direct current (DC) or radio frequency (RF) power supply, ex. metal, semiconductor, insulator, high melting material, and dielectric material.
2. The energy of the sputtered atoms is about 1-10 eV, corresponding to a temperature of about 10^4 - 10^5 K. This result shows that the lowering of synthesis temperature can be achieved by the high energetic sputter atoms during the sputtering process.
3. The sputter technology can be used to generate a large area sample with high quality and homogeneity.
4. The ratio of alloys thin films can be easily controlled by using co-sputtering or/and addition different reactive gas, ex. N_2 or O_2 .

Several typical sputtering systems are used for thin film deposition including DC diode, RF diode, magnetron sputtering systems and ion beam sputtering systems. The sputtering phenomenon is shown that the atoms are ejected from the solid target surface

due to the bombardment with the energetic ions. The detailed theory was studied by Wehner in 1960s.^{89,90} The features of sputtering collision are shown in Fig. 3.1. The sputtering is initiated from the collision between incident ions and surface atoms followed by inducing the collisions between surface atoms. The atoms may finally escape from the surface due to successive collisions.

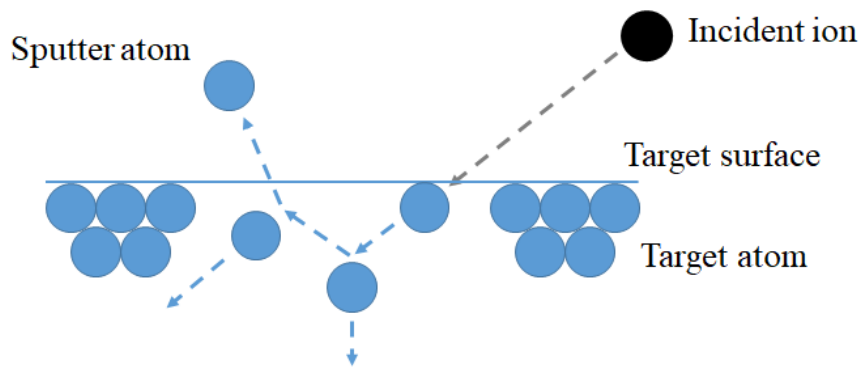


Fig. 3.1 The illustration of the sputtering collision.

In the sputtering system, the energetic ions can be produced by cold cathode glow discharge and the typical example is illustrated in the Fig. 3.2. In the discharge device, when the glow discharge is initiated in a low pressure gas with a high impedance power supply. The modes of discharge are dependent on the discharge current and the discharge modes versus current are shown in Fig. 3.3. The process of glow discharge is as follow

1. The gas molecules are ionized and generate energetic ions by collision with the energetic electron before traveling to the anode.
2. The cathode surface is bombarded with the energetic ions and produces the secondary electrons from the cathode surface.
3. The secondary electrons increase the ionization of gas molecules via collision and induce a self-sustained glow discharge.

However, the glow discharge current is below 10^{-9} A, the number of secondary electrons are insufficient to cause enough ionization to maintain a self-sustained glow discharge.

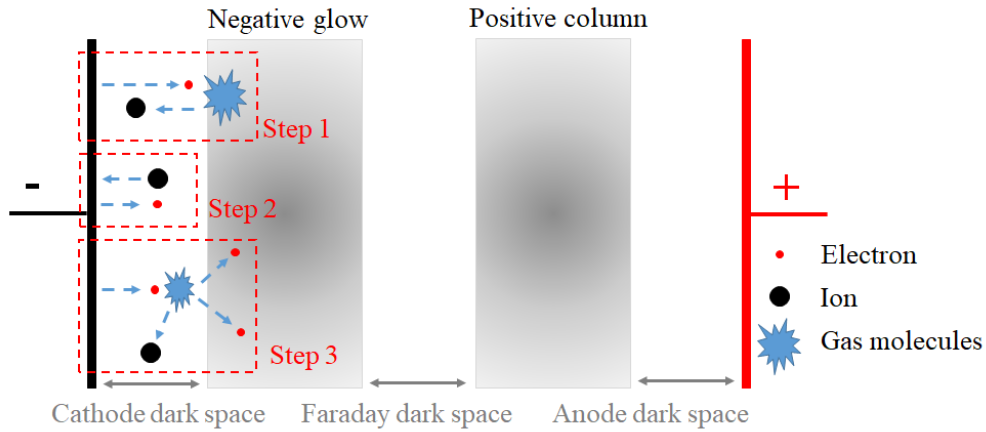
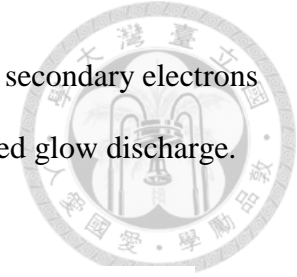


Fig. 3.2 The configuration of typical example and the process of glow discharge.

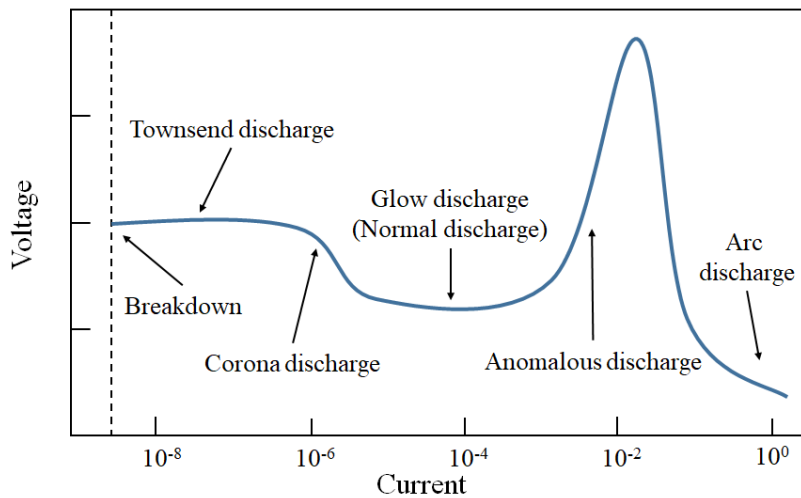


Fig. 3.3 A classification of gas discharge modes for different discharge current.

The process of gas discharge can be worked in the magnetic field. Fig. 3.4 (a) shows that the orbital motion of electron is around the magnetic field and the radius of the orbital motion is expressed as $r = mv/eB$, where the B is the magnetic field, the e is the

electron charge, the m and v are the mass and velocity of the electron, respectively. On the other hand, the transverse (parallel) magnetic field is superposed on the electric field (E), the configuration are shown in Fig. 3.4 (b) and (c), and the electrons shown cycloid (helical) motion in the space. This result shows that the magnetic field increases the collision probability between electron and gas molecules in the discharge device.

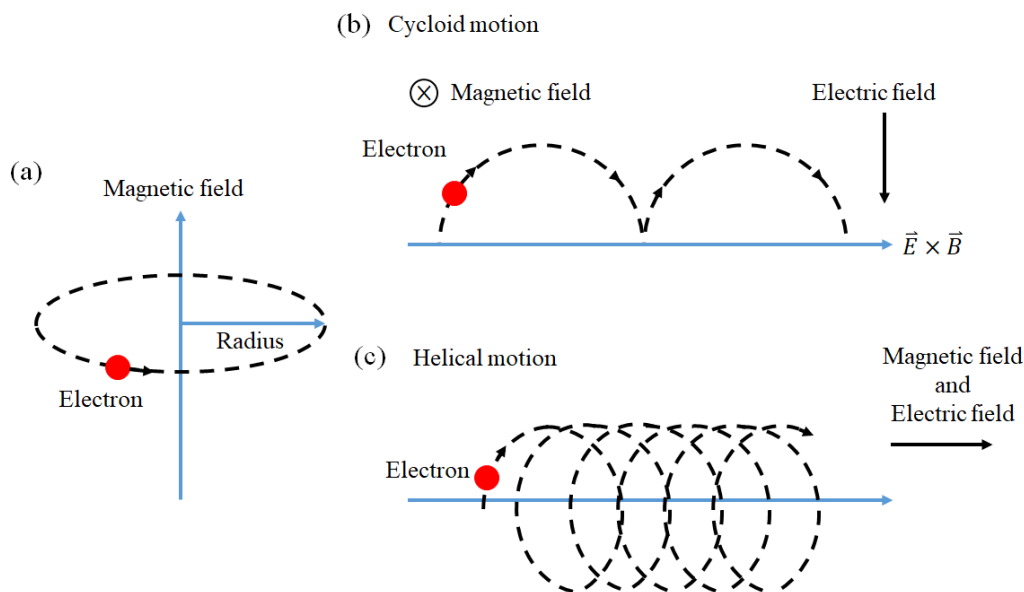


Fig. 3.4 (a) The orbital motion of electron around the magnetic field. The (b) Cycloid and (c) helical motion of electron under the magnetic and electric field.

The magnetron sputtering source is a typical application for discharge in the magnetic field. The magnetron sputtering system is an important technique for thin film deposition and two different configurations of magnetron sputtering systems are shown in the Fig. 3.5; cylindrical type and planar type magnetron sputtering systems. The magnetron sputtering system is first studied by Penning in 1935 and this technique is used for thin film deposition by Kay at 1960s.⁸⁶ In the magnetron sputtering system, the magnetic field increases the density of ions by more than one order of magnitude and

increases collision probability between ions and the target surface. The working pressure is 10^{-4} to 10^{-3} Torr for magnetron sputtering systems, which is two orders in magnitude lower than diode sputtering system (about 10^{-2} to 10^{-1} Torr). These results show that the thin film can be deposited with little film contamination and at a high deposition rate in this system. However, the magnetron sputtering systems have been found to be limited for using the magnetic target because the magnetic lines of force are confined within the target material. This problem has been solved by using the very thin magnetic target (the magnetic lines of force can be through the magnetic target).

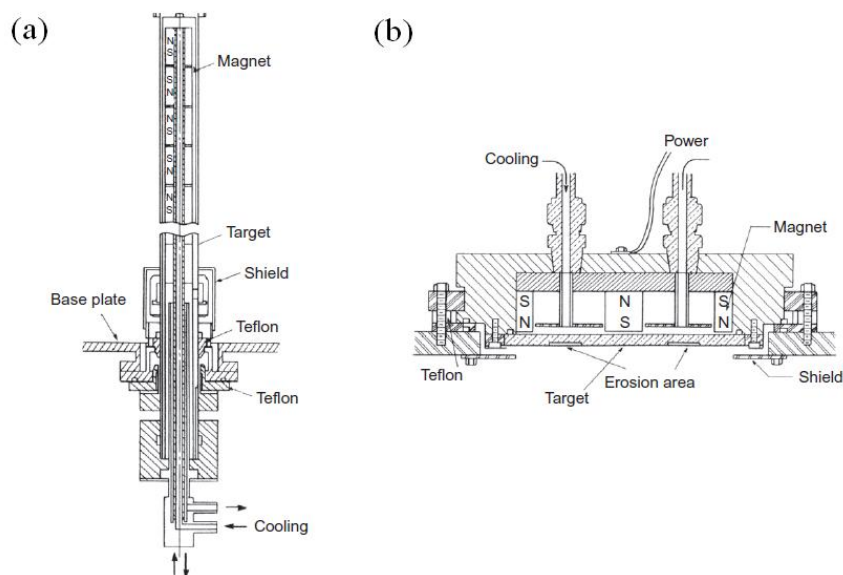


Fig. 3.5 The configuration of (a) cylindrical type and (b) planar type magnetron sputtering systems.⁸⁶

3.1.2 Sputtering system

The multi-gun magnetron sputtering system, CVT TFS-4700; shown in Fig. 3.6 (a), was used to deposit thin film in this work. This sputtering system includes two different vacuum systems: main chamber and loading chamber. The base pressure is less

than 4×10^{-7} and 1×10^{-4} Torr for main and loading chamber, respectively. Three sputtering sources are installed in the main chamber. The detailed configuration of the vacuum and sputtering chamber are shown in Fig. 3.7 (a) and (b), respectively.

The deposition of metal thin films has some issues in the original CVT TFS-4700 because this system is designed for the co-sputtering manufacturing process. The mutual interference of each target causing inhomogeneity and hard to control film quality. Therefore, we redesigned an isolated sputtering gun so that the plasma is not affected by other sputter sources. The sputtering sources are fixed on the bellow tube mechanism and the photo of sputtering sources are shown in the Fig. 3.6 (b). The working distance of sputtering, from source to sample holder, can be modulated from 7 to 20 centimeters in the high vacuum environment.

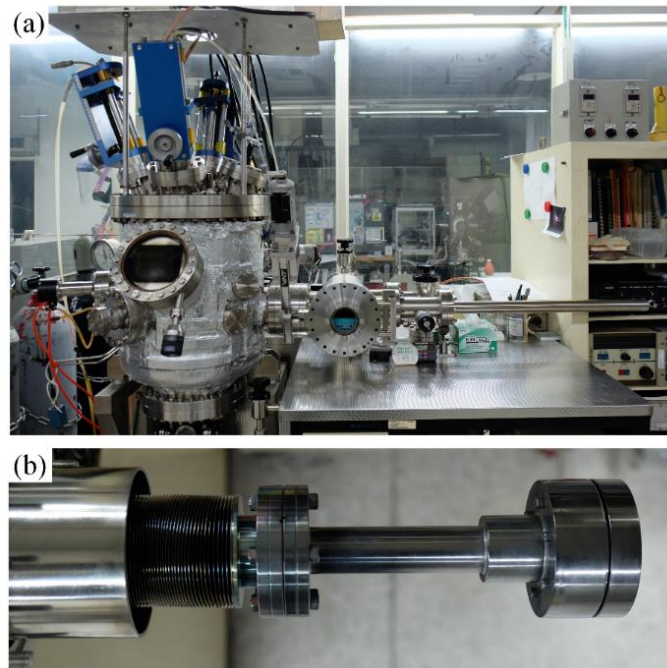


Fig. 3.6 The (a) multi-gun DC magnetron sputtering system and (b) the sputtering source.

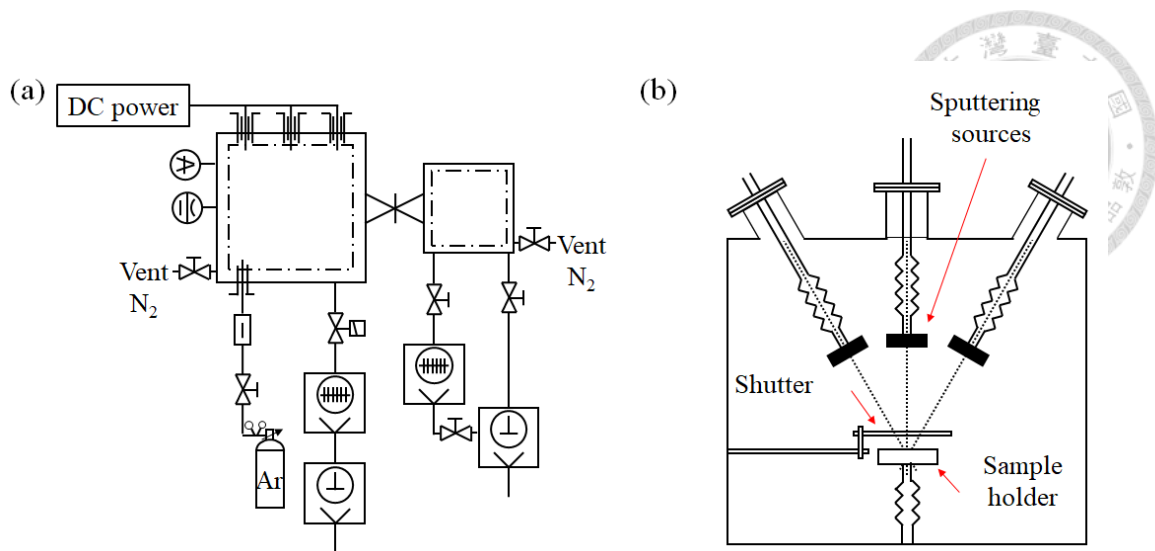


Fig. 3.7 The detail configuration of (a) vacuum and (b) sputtering chamber for CVT TFS-4700 system.

The deposition conditions were optimized based on the new design of the New CVT TFS-4700 system. A 60 W DC power and 10.5 cm working distance were used for Co thin film deposition. On the other hand, a 45 W DC power and 10 cm working distance were used for Pt thin film deposition. The sputtering gas is Argon gas and the pressure of 2.5×10^{-3} torr was maintained during thin film deposition.

3.2 Thin film deposition

3.2.1 Principle of thin film deposition

Creating nanomaterials is an important technology for the development of spintronic and electronic devices. Because many interesting phenomena (ex. spin transport, tunneling effect and field effect in the semiconductor) were only observed in the nanomaterials but cannot be find in the bulk materials. The nanomaterials ($1 \text{ nm} = 10 \text{ \AA}$

= 10^{-9} m) are defined and classified into three different types:⁸⁶

1. Zero-dimensional nanomaterials have three-dimensions of nanometer size, ex. Quantum dots.
2. One-dimensional nanomaterials have two-dimensions of nanometer size, ex. Nanowires.
3. Two-dimensional nanomaterials have one-dimensions of nanometer size, ex. Thin film.

The thin film technology has been used for more than in making electronic devices, optical coating and, etc. in the last fifty years. The thin film transistors (TFT) and thin film integrated circuits (IC) were generally studied in the 1960s. The Si-MOS (Metal Oxide Semiconductor) device was developed in the 1970s. After 1980s, the spin-dependent GMR effect and TMR were extensively studied in the FM thin film sandwich structure.⁸⁶ The thin film technology is a well-established technology for the material processing. However, it is still being developed on a daily basis, because it is an important technology in the development of new thin film devices, such as spin torque magnetoresistive random-access memory (ST-MRAM) and spin-basis spin-basis MOSFFT.^{32,40}

The thin film is defined as a two-dimensional nanomaterial made by stacking the atom or molecules on a substrate and the thickness is less than several micrometers. The step of thin film growth is shown in the following: adsorbent, surface diffusion, nucleation and film growth. During the thin film growth, the atoms are adsorbed on the substrate and move by surface diffusion. Then, the birth of thin films starts with random nucleation sites followed by nucleation and thin film growth stages. The Process of nucleation is shown in Fig. 3.8. The nucleation is a fundamental and important process for many areas of physics, chemistry and materials science. The nucleation involves the transition from



an initial or metastable phase A to a new phase B, ex. from vapor to liquid or vapor to solid.⁹¹ The nucleation growth and microstructure of thin film are dependent on various deposition conditions, such as growth temperature, growth rate, and substrate surface chemistry.

Process of nucleation

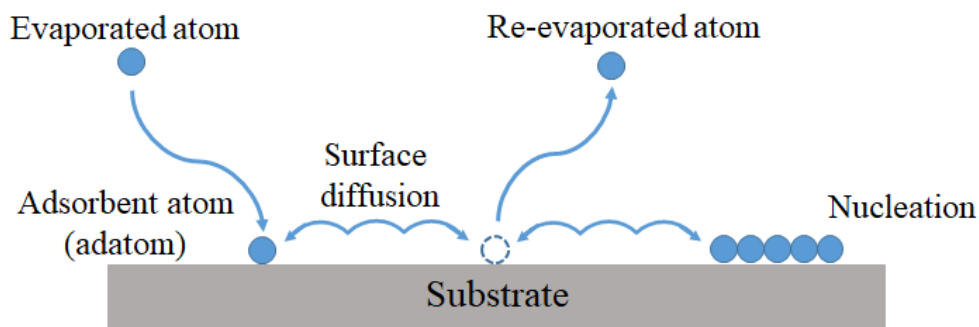


Fig. 3.8 The illustration of nucleation process.

There are three different primary mechanisms for thin film growth: Volmer-Weber (3D island growth), Frank-van der Merwe (2D layer by layer growth) and Stranski-Krastanow (S-K growth).^{92,93} The Schematic of three different growth mechanisms are shown in Fig. 3.9

In the Volmer-Weber mechanism, the adatoms are much more strongly bound to each other than to the substrate. During the thin film growth, as soon as the nucleation sites of the first layer are formed the second layer begins to deposition on top. Therefore, the many 3D islands are developed on the substrate and coalesce to a continuous thin film.

For the Frank-van der Merwe mechanism, the adatoms are much more strongly bound to substrate than to the other adatom. During the thin film growth, the nucleation sites are formed as Volmer-Weber mechanism but the new adatoms is only incorporated

into the first layer. After form the full monolayer, the atoms are deposition on the top of monolayer and result in a full thin film on the substrate.

The Stranski-Krastanow mechanism is a combination of the two different growth mechanisms: Frank-van der Merwe and Volmer-Weber growth mechanism. In the first stage, the one or two full monolayer is deposition on the substrate by the Frank-van der Merwe mechanism. Then, the growth mechanism changes to Volmer-Weber in the second stage and the 3D islands are developed on the top of the monolayer. At the finals, a continuous thin film can be achieved on the substrate.

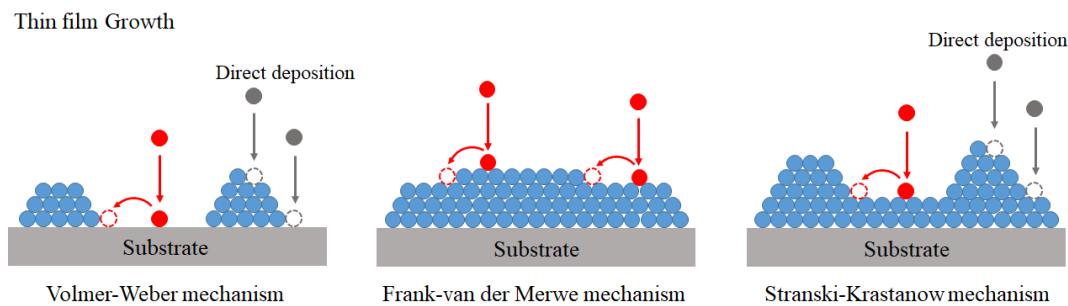


Fig. 3.9 Three different growth mechanisms: Volmer-Weber (3D island growth), Frank-van der Merwe (2D layer by layer growth) and Stranski-Krastanow (S-K growth).

The deposition methods of thin film can be discriminated by the two different deposition processes: Physical Vapor Deposition (PVD) and Chemical Vapor Deposition (CVD). The generally deposition methods are shown in Fig. 3.10 and the Table 3.1 are listed that the special features of the four different deposition processes. Compare with CVD techniques, the PVD techniques is an efficient and fast method using to thin film growth. The analysis of thin film properties is necessary and important for the study of thin film materials and devices. The properties of thin film include the crystalline structure, chemical composition, optical, electric and mechanical properties. Table 3.2 is

shown that several methods are used for the analysis of properties in this work.

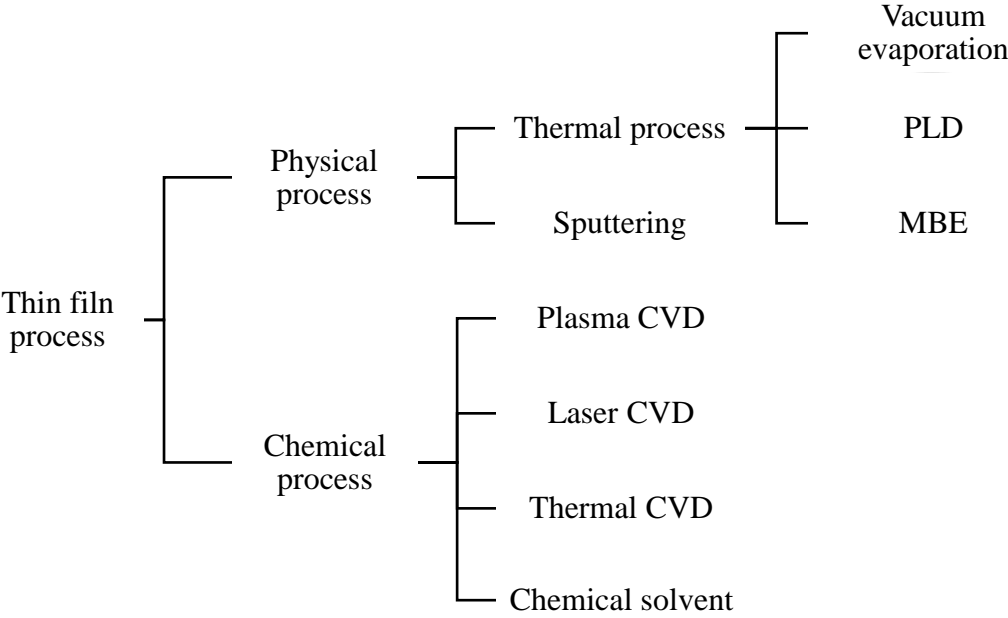


Fig. 3.10 The typical deposition methods of thin film.⁸⁶

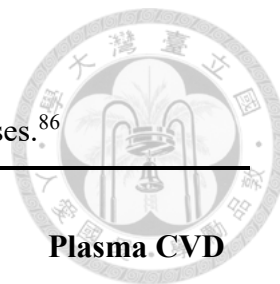


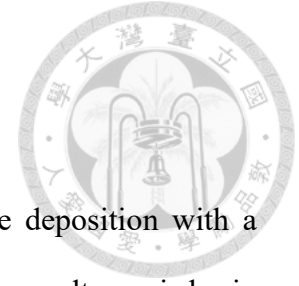
Table 3.1 The special features of the four different deposition processes.⁸⁶

| Type of Deposition | Electron Beam | Diode sputtering | Magnetron sputtering | Plasma CVD |
|----------------------------|--------------------------------|---|--|---|
| Deposition material | Material of high melting point | Wide varieties of materials, compounds refractory metals, alloys. | | Decomposition and/or chemical reaction of organometallic compounds or halides |
| Temperature of substrate | Low | High (>300°C) | Low (<100°C) | High (>300°C) |
| Deposition rate | 80~800 Å/sec | 3~30 Å/sec | 80~800 Å/sec | 80~800 Å/sec |
| Gas pressure | Low < 10 ⁻⁵ Torr | High 10 ⁻² ~10 ⁻¹ Torr | Low 10 ⁻² ~10 ⁻¹ Torr | High 1~10 Torr |
| Energy of evaporated atoms | 0.1~0.2 eV | 10~200 eV | 10~20 eV | - |
| Energy of adatoms | 0.1~0.2 eV | 0.1~20 eV | 0.2~10 eV | - |



Table 3.2 Several methods of analysis are used in this work

| Properties | Analysis method | Physical parameter |
|------------|--|-----------------------------|
| Thickness | Alpha-step | Thickness |
| | Transmission electron microscopy (TEM) | |
| Structure | High resolution | Crystallite structure |
| | transmission electron microscopy (HRTEM) | |
| Electrical | Four-terminal resistive measurements | Resistivity |
| | Hall effect measurement | Doping concentration |
| | | Hall coefficient |
| | | Diffusion constant |
| Magnetic | Ferromagnetic Resonance (FMR) | Resonance field |
| | | Damping constant |
| | | gyromagnetic ratio |
| | | g-factor |
| Spin | Vibrating-Sample Magnetometer (VSM) | Saturation magnetization |
| | | Anisotropy field |
| Spin | Inverse spin Hall effect (ISHE) | Effective anisotropy energy |
| | | Spin Hall angle |
| | | Spin lifetime |



3.2.2 Sample preparation

Before deposition, the Si-substrates were cleaned prior to the deposition with a sequence of acetone, ethanol, 2-propanol and de-ionized (DI) water in an ultrasonic basin for 15 minutes each. There are three different series sample were prepared in this work. As follows,

Reference sample: Pt (10 nm)/Co (t_{Co} nm)/Si

A series of reference sample Pt/Co bilayer, Pt (10 nm)/Co (t_{Co} nm), was deposited on an undoped Si-substrate at room temperature using the DC magnetron sputtering system. The Co-thickness (t_{Co}) varied from 5 to 40 nm. The sample names are denoted as Pt/Co (t_{Co})/undoped. The t_{Co} was controlled by the deposition time with the deposition rate of Co and Pt being 1.6 and 2.7 Å/sec, respectively. The deposition rate is derived from Alpha step results (DEKTAK 6M) and the error is 3% in our system.

Sample A: Co (t_{Co} nm)/Si

A series of single Co layer, Co (t_{Co} nm)/Si, were deposited on the different resistivity Si (100) substrate at room temperature using the DC magnetron sputtering system. The t_{Co} varied from 5 to 40 nm. The sample names are denoted corresponding to the thickness of Co, carrier type of Si and the nominal resistivity. For example, Co (10)/n-Si-10 represents the sample with the thickness of Co being 10 nm, carrier type of Si being electron, and the nominal resistivity of Si being 10 ohm-cm. The characteristics of Si-substrate and sample name of Co/Si are shown in Table 3.3.

Table 3.3 The parameter and name of Si-substrate, and define the name for all samples.

| Sample name | Co (t_{Co})/ <i>undoped-Si</i> | Co (t_{Co})/ <i>n-Si-10</i> | Co (t_{Co})/ <i>p-Si-10</i> | Co (t_{Co})/ <i>p-Si-0.1</i> | Co (t_{Co})/ <i>p-Si-0.005</i> |
|---------------------------------|---------------------------------------|------------------------------------|------------------------------------|-------------------------------------|---------------------------------------|
| Substrate name | <i>undoped-Si</i> | <i>n-Si-10</i> | <i>p-Si-10</i> | <i>p-Si-0.1</i> | <i>p-Si-0.005</i> |
| t_{Si} (μm) | 290 \pm 10 | 500 \pm 25 | 500 \pm 25 | 500 \pm 25 | 500 \pm 25 |
| Dopant | - | Phosphorus | Boron | Boron | Boron |
| Carrier type | - | electron | hole | hole | hole |
| Nominal resistivity (Ohm-cm) | 3000~ 5000 | 1~10 | 1~10 | 0.1~0.2 | 0.005~ 0.008 |

Sample B: Co (t_{Co} nm)/GaAs

A series of single Co layer, Co (t_{Co} nm)/GaAs, were deposited on the *p*- and *n*-GaAs (100) substrate at room temperature using the DC magnetron sputtering system. The t_{Co} varied from 5 to 40 nm. The sample names are denoted corresponding to the thickness of Co and carrier type of GaAs. For example, Co (10)/*n*-GaAs represents the sample with the thickness of Co being 10 nm, carrier type of GaAs being electron. The characteristics of GaAs-substrate and sample name of Co/GaAs are shown in Table 3.4.



Table 3.4 The parameter and name of GaAs-substrate, and define the name for all samples.

| Sample name | Co (t_{Co})/ <i>n</i> -GaAs | Co (t_{Co})/ <i>p</i> -GaAs |
|---------------------------------|------------------------------------|------------------------------------|
| Substrate name | <i>n</i> -GaAs | <i>p</i> -GaAs |
| t_{GaAs} (μm) | 350 \pm 20 | 350 \pm 20 |
| Dopant | Silicon | Zinc |
| Carrier type | electron | hole |



3.3 Measurements

3.3.1 Hall effect

The Hall coefficient (R_H) and resistivity (ρ) can be measured by van der Pauw method in disk of irregular shape and thin film material. In the van der Pauw measurement, the contacts are placed on the corner of the samples and the schematic of measurement is shown in the Fig 3.11. The current is supplied through the contacts 1 and 3 (I_{13}) and the Hall voltage is measured across the contacts 2 and 4 (V_{24}). The error in the measurement may result from the misalignment of the contacts, where the joining line of the contacts 2 and 4 should be perpendicular to the applied current (contact 1 to 3 or inversely). One usually measures the voltage both with and without the \mathbf{B} ($V_{24}(\pm\mathbf{B})$ and $V_{24}(0)$) to minimize error in the measurement of Hall voltage.⁹⁴ The R_H are shown as

$$R_H = \frac{[V_{24}(\mathbf{B}) - V_{24}(0)]d}{I_{13}\mathbf{B}} = \frac{[V_{24}(\mathbf{B}) - V_{24}(-\mathbf{B})]d}{2I_{13}\mathbf{B}} = \frac{1}{nq} \quad \text{Eq. 3.1}$$

where d is the thickness of the thin film.

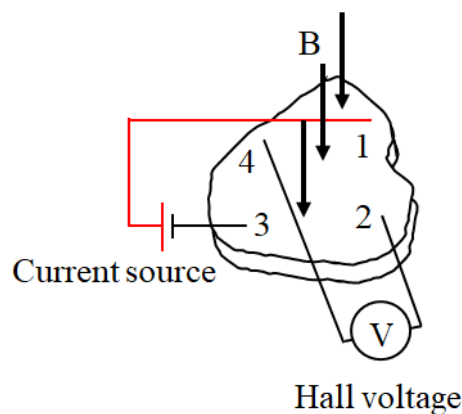
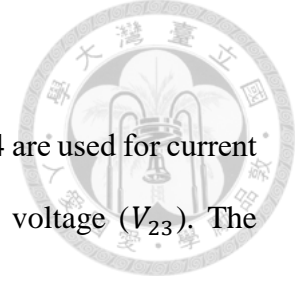


Fig. 3.11 The schematic of measurement for van der Pauw method



For the measurement of ρ , two adjacent contacts such as 1 and 4 are used for current injection (I_{14}) and remaining contacts are used for measuring the voltage (V_{23}). The resistance can be defined as

$$R_{23,14} = \frac{V_{23}}{I_{14}} \quad \text{Eq. 3.2}$$

On the other hand, the sample is rotated 90 degrees in which the current is injected by the contacts 1 and 2, the voltage is measured by remaining contacts. The resistance can be defined as $R_{43,12}$. The ρ can be calculated by combining $R_{23,14}$ and $R_{43,12}$ and show as

$$\rho = \frac{\pi d f (R_{23,14} + R_{43,12})}{2 \ln 2} \quad \text{Eq. 3.2}$$

where f is a factor that depends on the ratio $R_{23,14}/R_{43,12}$. Usually a large value for f indicate that the contacts are bad or the sample is inhomogeneous.

Hall effect measurement

The doping concentration (N), ρ and R_H of Si and GaAs substrates were measured at room temperature with $H = 5500$ Oe by a Hall effect system (HMS-3000). The mobility ($\mu = \frac{R_H}{\rho}$) and diffusion constant of SC (D_N , $D_N e = \mu kT$) can be derived from ρ and R_H data. The HMS-3000 includes a source meter, sample holder, permanent magnet and measurement program. The ρ and N can be detected in the range from 10^{-4} to 10^7 Ohm-cm and from 10^7 to 10^{21} cm⁻³, respectively, in our Hall effect system.

The Au electrodes of 150 nm were deposited at four corners of substrates by DC sputtering system (Quorum Q150T S) before measuring Hall effect. The surface area of Si-substrates and Au are 5×5 mm² and 1.5×1.5 mm², respectively. The details of the measurement for Hall effect are listed in Table 3.5 The schematic of Hall effect system

and measured sample are shown in the Fig. 3.12.



Fig. 3.12 The schematic of (a) Hall effect system, (b) sample holder and (c) measured sample.

3.3.2 High resolution transmission electron microscopy (HRTEM)

Due to the physically limit, it is impossible to detect nanostructure using optical microscope. If we want to retain the classical optical imaging structure, we have to replace the visible light by something with shorter wavelength. The transmission electron microscopy (TEM) is a high resolution and versatile tool for nanostructure analysis. Because the TEM images are formed by electrons for which the wavelength is much smaller than visible light. Due to the wavelength of the electron beam is smaller than the size of atoms, the real arrangement of atoms can be observed using TEM measurement. The conformation of TEM can be decomposed into two different systems: Illumination and Imaging system. The illumination system includes an electron gun and a condenser electromagnetic system. The imaging system includes sample hold system, an objective and two projective electromagnetic lens and CCD camera.

The electrons are emitted by thermionic, Schottky, or field-emission electron gun and concentrate to electron beam by condenser electromagnetic lens. The electron beam through the crystalline sample, the diffracted ray is focused on the back-focal plane via objective electromagnetic lens and creates a diffraction spot in this plane. Finally, the diffraction pattern is imaged on the observation screen by modulation the focal length of projective electromagnetic lens.^{95,96} Besides the functioning principle of TEM, its conformation is basically similar to the optical microscope. The schematic of transmission electron microscope and light optical microscope are shown in Fig. 3.13 (a) and (b), respectively.

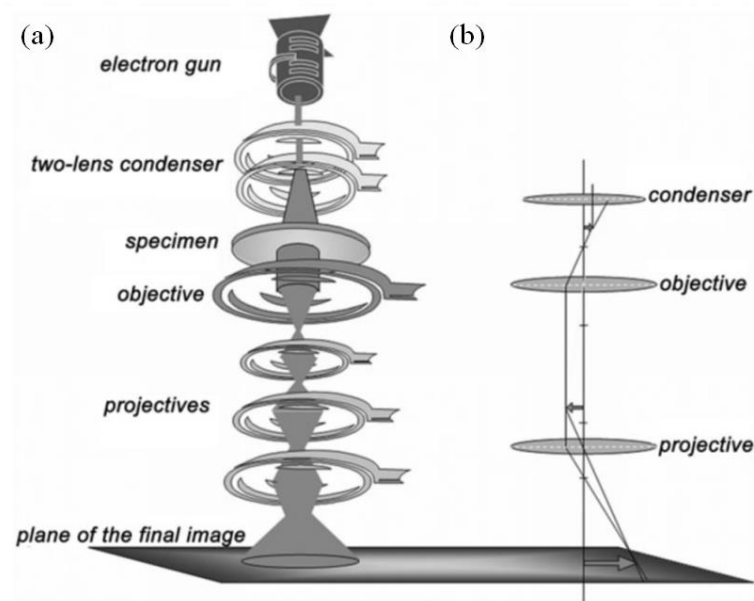


Fig. 3.13 The schematic of (a) transmission electron microscope and (b) light optical microscope.⁹⁵

HRTEM measurement

The crystallite structure, high resolution transmission electron microscopy (HRTEM) images and electron diffraction patterns of Co thin film, Co (40)/Si-Sub., were observed

by the FEGTEM system (FEI E.O Tecnai F20 G2 Field-Emission TEM). The focused ion-beam (FIB, Hitachi NX2000) technique was used to prepare the samples with micrometer scale before doing HRTEM. The picture of FEGTEM and FIB system is shown in the Fig. 3.14 (a) and (b), respectively. The acceleration voltages can be modulated from 20 to 200 kV and the magnification can be change from 25 to 1.03M. The point resolution, line resolution, information resolution are 0.23, 0.1 and 0.15 nm, respectively, in this TEM system.

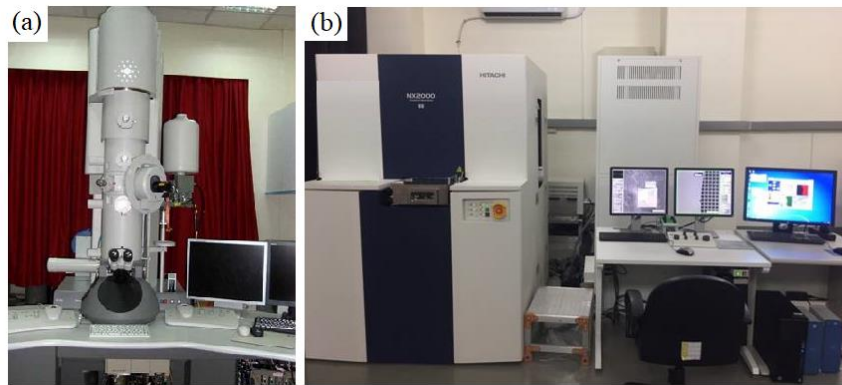


Fig. 3.14 The picture of (a) FEGTEM and (b) FIB system (This picture download from High valued Instrument Center of NSYSU)

3.3.3 Vibrating-Sample Magnetometer (VSM)

The Vibrating-Sample Magnetometer (VSM) is a powerful and sensitive tool using to detection of the Hysteresis loops ($M - H$ loops). It is based on the flux change near a detection coil in the uniform H when a magnetized sample is extracted or inserted near the coil. The total flux (Φ_T) through the coil in the magnetic field is

$$\Phi_T = BA = (H_{ex} - N_d M + 4\pi M)A \quad \text{Eq. 3.3}$$

where H_{ex} is an external field, N_d is a demagnetizing factor, M is a magnetization, A

is magnetized sample or coil area. If the magnetized sample is fast removed from the coil, the flux (ϕ_R) through the coil becomes

$$\phi_R = BA = H_a A \quad \text{Eq. 3.4}$$

The change of the flux is shown as,

$$\phi_T - \phi_R = (4\pi - N_d)MA \quad \text{Eq. 3.5}$$

the equation shows that the flux change is proportional to the magnetization and can be recorded by the flux-meter.⁹⁷ In the VSM system, a sample is placed on the end of a nonmagnetic rod and the other end of which is fixed on a mechanical of vibrator; the diagram is shown in Fig. 3.15 (a). The sample is vibrated near the detection coil and the direction is perpendicularly to the H . According to Faraday's law, the oscillating magnetic field of the vibrating sample induces a voltage in the detection coil. This voltage is proportional to the magnetic moment of the sample. The voltage signal can be amplified by a lock-in amplifier and the limiting sensitivity is about 10^{-5} emu. The VSM can be easily operated for the measurements at the high or low temperatures because only the sample must be heated or cooled.

These important magnetic parameters, saturation magnetization (M_s), anisotropy field (H_k) and effective anisotropy energy (K_{eff}) effective demagnetization ($4\pi M_{eff}$), can be determined and derived from the $M - H$ loop and Two typical $M - H$ loops are sketched in the Fig. 3.15 (b) and (c). Fig. 3.15 (b) shows that the $M - H$ loop is measured with H parallel to the easy axis. The $M_s \equiv M(max)$ is the saturation magnetization, $M_r \equiv M(H = 0)$ is the remanence magnetization, $H_s \equiv H(M_s)$ is saturation field, $H_c \equiv H(M = 0)$ is the coercive field or coercivity. On the other hand, the Fig. 3.15 (c) shows that the $M - H$ loop is measured with H parallel to the hard axis and The value of M_r and H_c both approach zero.



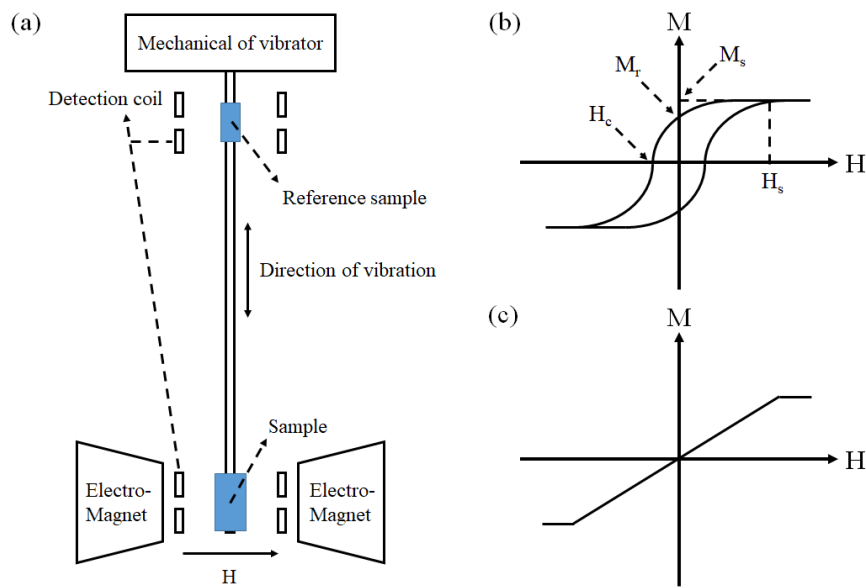


Fig. 3.15 (a) The diagram of VSM measurement system. The typical $M - H$ loops measured parallel to (b) easy axis and (c) hard axis.

VSM measurement

The $M - H$ loop of Co thin film, for sample A and B, were measured at room temperature by measuring VSM (MicroSense VSM EZ9). The $M - H$ loop was measured by sweeping the H from -20 kOe to 20 kOe with two different directions of the H : in-plane (H is perpendicular to the normal vector of film plane) and out-of-plane direction (H is parallel to the normal vector of film plane). The signal noise about 0.4 μemu and field resolution is about 5 mOe in our VSM system. The schematic of VSM system and measurement set up are shown in the Fig. 3.16. The parameter of measurement for VSM is shown in Table 3.5.

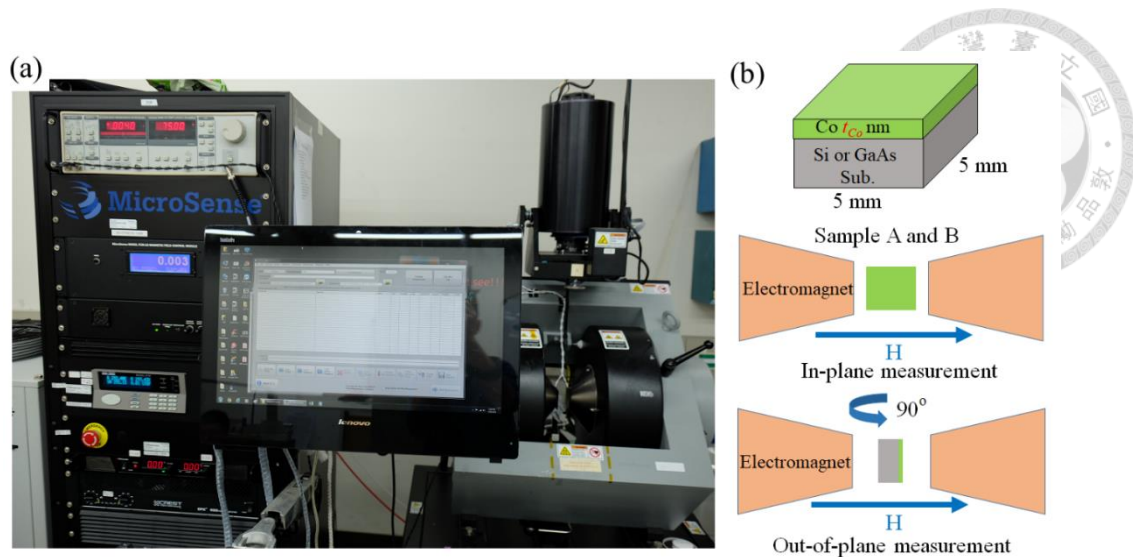


Fig. 3.16 The schematic of (a) VSM system and (b) the measurement set up of VSM.

3.3.4 Ferromagnetic resonance (FMR) and Inverse spin Hall effect

(ISHE)

The FMR is a sensitivity, versatile and nonintrusive tool used to analyze the character of FM material. The FMR spectrum was measured at room temperature using a FMR system (Bruker EMX) in this work. The Bruker EMX system includes a DC power supply, microwave (MW) source, electromagnet, TE₁₀₂ MW cavity and measurement program. The MW source comes from klystron and transmitted into the cavity by the waveguide. The voltage signal of ISHE was measured using nano-voltmeter (Keithley 2182A) under FMR condition and the magnitude of the external magnetic field was detected by a Gauss meter. The photo and schematic of Bruker EMX system are shown in Fig. 3.17 (a) and (b), respectively. For our FMR and ISHE measurement, the sample was placed in the center of TE₁₀₂ MW cavity, where the frequency of MW was 9.8 GHz (X-band), the magnetic field (h_{ac}) of the MW is maximum and the electric field (e_{ac}) of the MW is minimum; show in Fig. 3.17 (c). The FMR spectra and voltage signal were

detected by sweeping the H from 200 Oe to 14000 Oe and the field resolution can be defined as the field range per 4096 point in our measurement. The power of MW (P_{MW}) can be modulated from 100 mW to 20 mW. The angular-dependence FMR spectra and voltage signal were measured by rotating the sample Holder. The photo of Keithley 2182A and sample holder are shown on Fig. 3.18 (a) and (b), respectively.

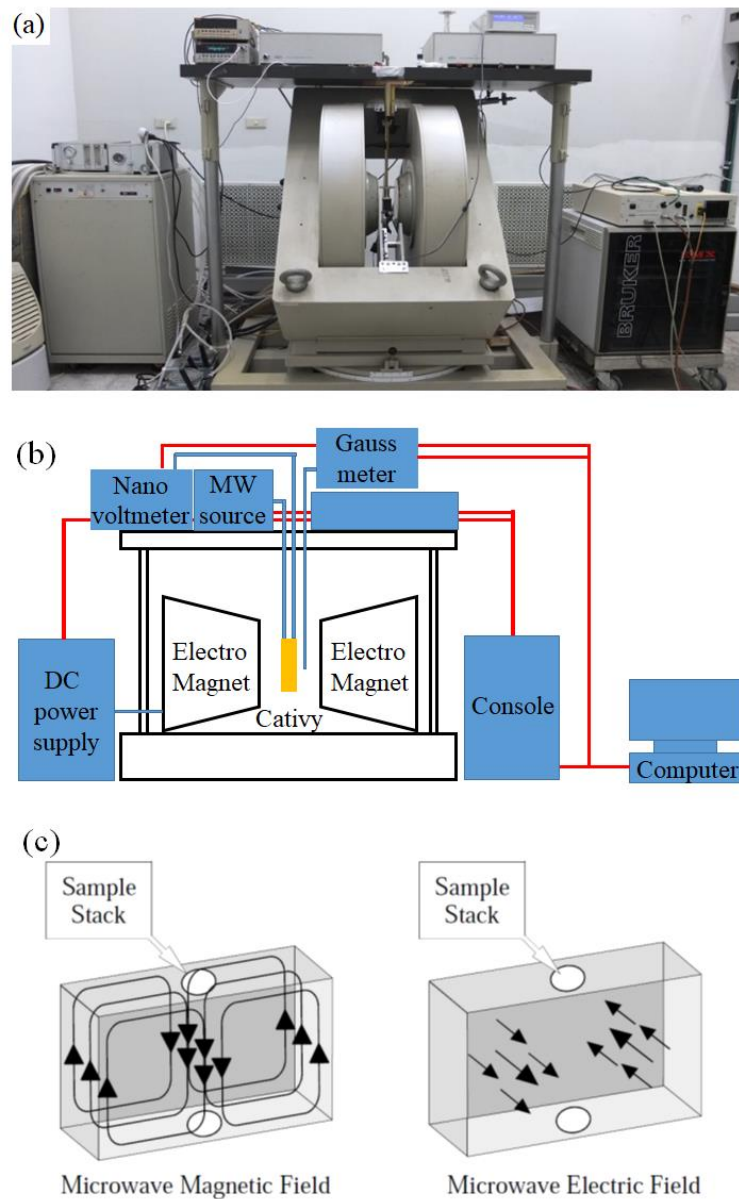


Fig. 3.17 The (a) photo and (b) schematic of Bruker EMX system. (c) The Magnetic and electric field patterns in a standard TE₁₀₂ cavity



Fig. 3.18 The photo of (a) nano-voltmeter (b) sample holder.

FMR and ISHE measurement

In this work, the FMR and ISHE measurements of reference sample, sample A and B had three different set up: Co-thickness dependence (t_{Co} -dependence), Power of MW dependence (P_{MW} -dependence) and angular dependence (θ_H -dependence). The schematic of measurement set up of FMR and ISHE are shown in the Fig. 3.19.

1. For t_{Co} -dependence FMR measurements, the t_{Co} was varied from 5 to 40 nm. The P_{MW} is set at 100 mW and the θ_H is 0° and 180° (the direction of H is perpendicular to the normal vector of film plane at $\theta_H = 0^\circ$). The spectrum was detected by sweeping the H from 200 to 1100 Oe.
2. For P_{MW} -dependence measurement, the P_{MW} was varied from 20 to 100 mW and the θ_H was fixed on 0° . The spectrum was detected by sweeping the H from 200 to 1100 Oe.
3. For θ_H -dependence measurement, the θ_H was varied from 0° to 180° and the

P_{MW} was fixed on 50 mW (H is parallel to the normal vector of film plane at 90°). The θ_H can be control by rotating the sample Holder. The FMR spectrum was detected by sweeping the H from 200 to 14000 Oe.

The θ_H -dependence data of resonance field (H_r), linewidth (ΔH) and voltage signals (V) are denoted as $H_r(\theta_H)$, $\Delta H(\theta_H)$ and $V(\theta_H)$, respectively. For simplicity, if the θ_H is not specified, it means the θ_H is 0° . The parameter of measurement for FMR and ISHE are ordered in Table 3.5.

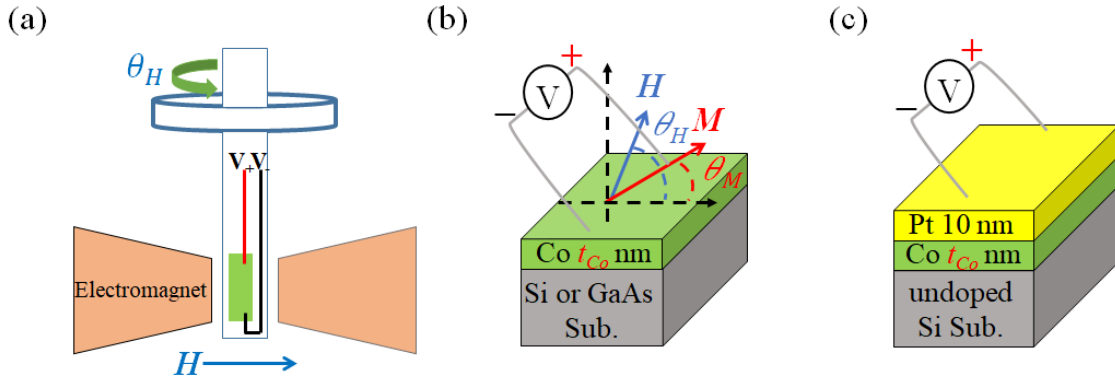


Fig. 3.19 The measurement set up of (a) FMR and (b) ISHE for reference sample, sample A and sample B, respectively.

Table 3.5 The parameter of measurement for Hall effect, VSM, FMR and ISHE

| Method | Hall effect | VSM | FMR and ISHE | | |
|--------------------|---------------------|------------------------------|-----------------------------------|------------------------------|-----------------------------|
| | | | t_{Co-} dependence | P_{MW-} dependence | θ_H- dependence |
| Sample type | Si and GaAs-sub. | Sample A, and B | Reference sample, Sample A and B. | | |
| Sample size | 5×5 mm ² | 5×5 mm ² | 3×1.5 mm ² | | |
| Magnetic field | 5500 Oe | Sweep from -20 kOe to 20 kOe | Sweep from 200 Oe to 1100 Oe | Sweep from 200 Oe to 1100 Oe | Sweep from 200 Oe to 14 kOe |
| Orientation of H | 90° and 270° | 0° and 90° | 0° and 180° | 0° | varied from 0° to 180° |
| Power of MW | - | - | 100 mW | Varied from 20 mW to 100 mW | 50 mW |

Chapter 4 Result and discussions



4.1 Spintronic transport in Si with different doping

concentration and dopants

4.1.1 Hall effect measurement for Si

The accurate electrical properties, such as N , ρ , R_H , μ , and D_N of SC were experimentally determined by Hall effect system. For Si system, the N is 1×10^{13} , 8.1×10^{14} , 2.8×10^{15} , 1.8×10^{17} and $1.7 \times 10^{19} \text{ cm}^{-3}$ for *undoped*-Si, *n*-Si-10, *p*-Si-10, *p*-Si-0.1 and *p*-Si-0.005, respectively. The ρ is 3000, 8.6, 4.6, 0.15 and 0.007 $\Omega\text{-cm}$ for *undoped*-Si, *n*-Si-10, *p*-Si-10, *p*-Si-0.1 and *p*-Si-0.005, respectively. The R_H decreases from 3000 to 0.37 cm^3/C with increasing N from 2.8×10^{15} to $1.7 \times 10^{19} \text{ cm}^{-3}$ for *p*-type Si-sub.. On the other hand, the values of ρ and R_H are 4.6 $\Omega\text{-cm}$ and -7600 cm^3/C , respectively, for *n*-type Si-sub. with N of $8.1 \times 10^{14} \text{ cm}^{-3}$.

The mobility and diffusion constant are determined using Eq. 4.1 and Eq. 4.2, respectively.⁹⁸

$$\mu = \frac{R_H}{\rho} \quad \text{Eq. 4.1}$$

$$D_N = \frac{\mu kT}{e} \quad \text{Eq. 4.2} \quad \text{Einsitein's relation}$$

For *p*-type Si, the reduction in μ and D_N is observed with increasing doping concentration. The μ decreases from 351.1 to 54.23 cm^2/Vs and D_N decreases from 9.0 to 1.4 cm^2/s when N increase from 2.8×10^{15} to $1.7 \times 10^{19} \text{ cm}^{-3}$. For *n*-type Si, the values are 1662 cm^2/Vs and 6.0 cm^2/s , respectively. The accurate electrical properties of Si are listed in the Table 4.1.

The value ($54 \text{ cm}^2/\text{Vs}$) of μ for heavily doped p -type Si, p -Si-0.005, is comparable to the literature ($57 \text{ cm}^2/\text{Vs}$).⁹⁹ Furthermore, the μ of n -type Si is larger than that of p -type Si for similar N and it is consistent with the literature report. Because, the variation of μ is directly related to the relaxation time and varies inversely with the conductivity effective mass.⁹⁸

Table 4.1 The parameter of carrier concentration (N), resistivity (ρ), thickness (t_{Si}), Hall coefficient (R_H), mobility (μ) and diffusion constant (D_N) for silicon substrate.

| Substrate name | <i>undoped-Si</i> | <i>n-Si-10</i> | <i>p- Si-10</i> | <i>p- Si-0.1</i> | <i>p- Si -0.005</i> |
|--------------------------------------|------------------------------------|--------------------------------------|--------------------------------------|--------------------------------------|--------------------------------------|
| N (cm^{-3}) | (1 ± 0.1) $\times 10^{13}$ | (8.1 ± 0.4) $\times 10^{14}$ | (2.8 ± 0.2) $\times 10^{15}$ | (1.8 ± 0.1) $\times 10^{17}$ | (1.7 ± 0.1) $\times 10^{19}$ |
| ρ (ohm-cm) | 3800 ± 750 | 4.6 ± 0.1 | 8.6 ± 0.3 | 0.15 ± 0.01 | 0.007 ± 0.0001 |
| t_{Si} (μm) | 290 ± 10 | 500 ± 25 | 500 ± 25 | 500 ± 25 | 500 ± 25 |
| R_H (cm^3/C) | - | (-7.6 ± 0.4) $\times 10^3$ | (3.0 ± 0.4) $\times 10^3$ | (3.52 ± 0.02) $\times 10^1$ | (3.7 ± 0.1) $\times 10^{-1}$ |
| μ (cm^2/Vs) | - | 1662 ± 50 | 351 ± 2 | 238 ± 2 | 54 ± 3 |
| D_N (cm^2/s) | - | 42 ± 1 | 9.0 ± 0.2 | 6.0 ± 0.1 | 1.4 ± 0.1 |

4.1.2 Microstructures and magnetic properties of Co/Si

The crystallite structure of Co thin films is determined by the TEM experiment. The cross-section TEM images are shown in Fig. 4.1 (a) ~ (e) for all Co (40)/Si samples. The images show the t_{Co} is approximately 41 nm which is close to the nominal thickness (40 nm), showing a good deposition control and stability of the sputtering system. The HRTEM images and electron diffractogram of the TEM are displayed in Fig. 4.2 (a) ~ (e) and inset of Fig. 4.2 (a) ~ (e), respectively, for all Co (40)/Si. Rings and spots observed in electron diffraction pattern are originated from Co thin films and (100) planes of Si-substrates, respectively. From the TEM and diffraction results, the Co thin film have similar crystallite structure for all Co (40)/Si and a nature amorphous SiO_2 layer is found between Co and Si-substrate.

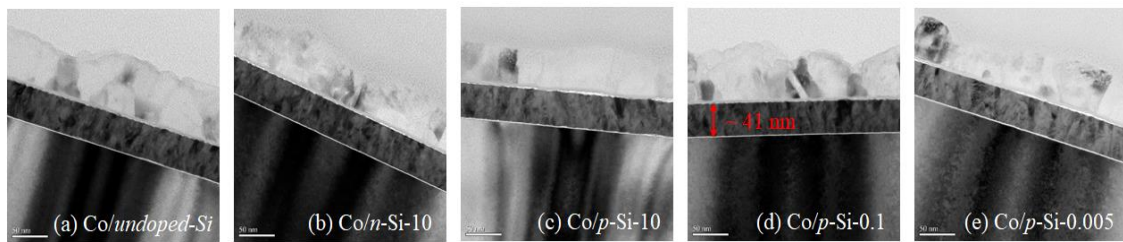


Fig. 4.1 The cross-section TEM images for Co (40)/Si samples. (a) the Co/undoped-Si (b) Co/p-Si-10 (c) Co/n-Si-10 (d) Co/p-Si-0.1 (e) Co/p-Si-0.005.

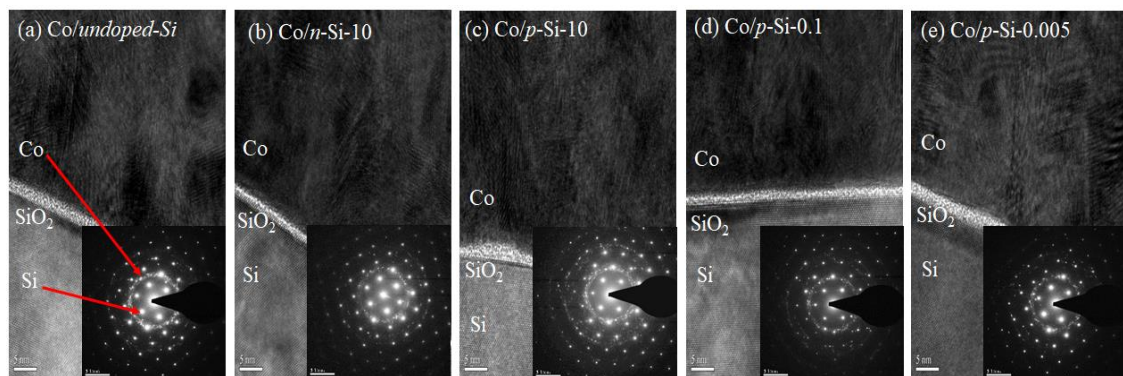


Fig. 4.2 The images of HRTEM and electron diffraction patterns for Co (40)/Si samples.

(a) the Co/*undoped*-Si (b) Co/*p*-Si-10 (c) Co/*n*-Si-10 (d) Co/*p*-Si-0.1 (e) Co/*p*-Si-0.005.

The magnetic properties of Co thin films for sample A are obtained by analyzing VSM data. The $M - H$ loops of Co (t_{Co})/*undoped*-Si, Co (t_{Co})/*p*-Si-10, Co (t_{Co})/*n*-Si-10, Co (t_{Co})/*p*-Si-0.1 Co (t_{Co})/*p*-Si-0.005 are shown in Fig. 4.3 ~ 4.7, respectively.

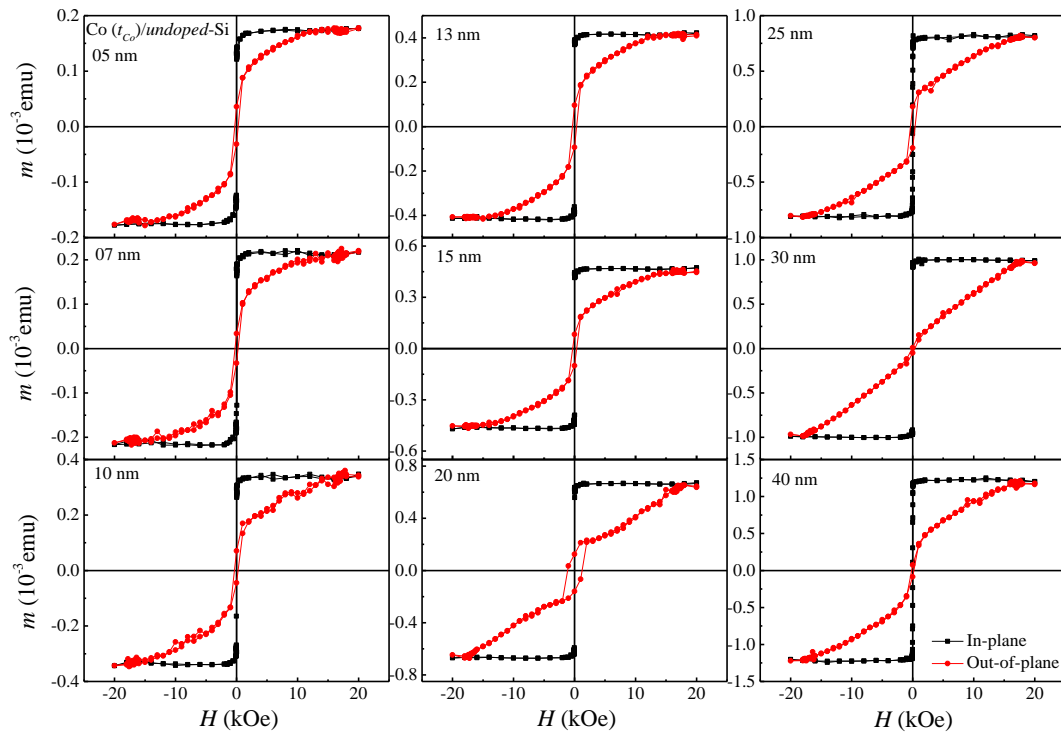


Fig. 4.3 The $M - H$ loops of Co (t_{Co})/*undoped*-Si and the t_{Co} change from 5 nm to 40 nm.

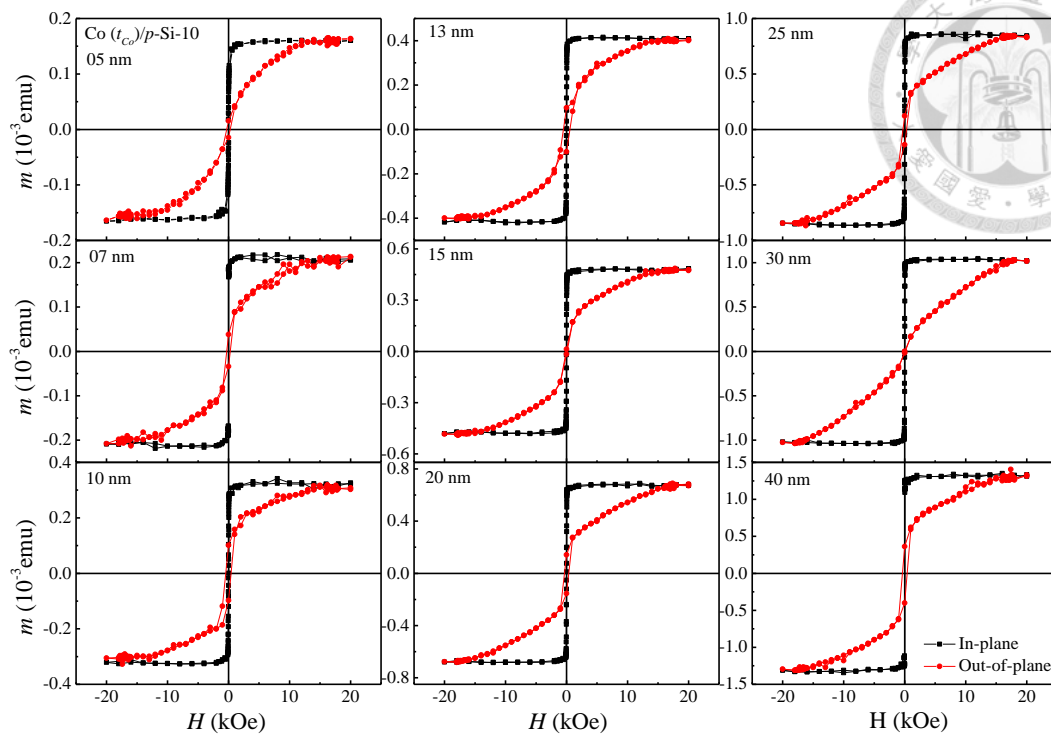


Fig. 4.4 The $M - H$ loops of $\text{Co}(t_{\text{Co}})/p\text{-Si-10}$ and the t_{Co} change from 5 nm to 40 nm.

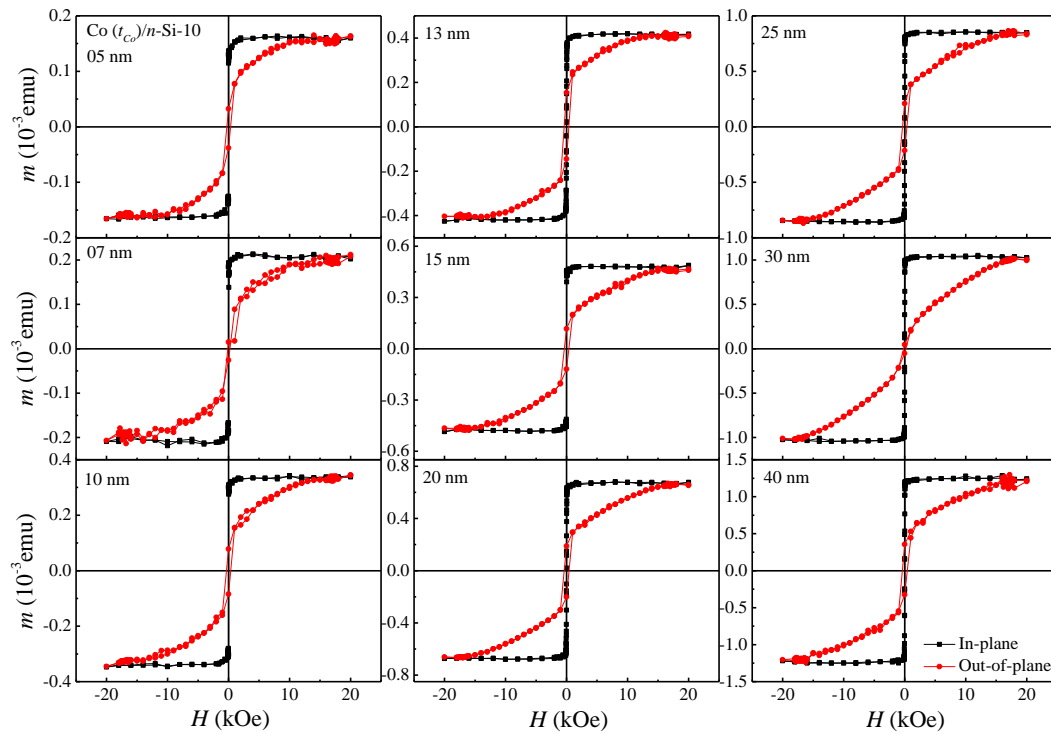


Fig. 4.5 The $M - H$ loops of $\text{Co}(t_{\text{Co}})/n\text{-Si-10}$ and the t_{Co} change from 5 nm to 40 nm.

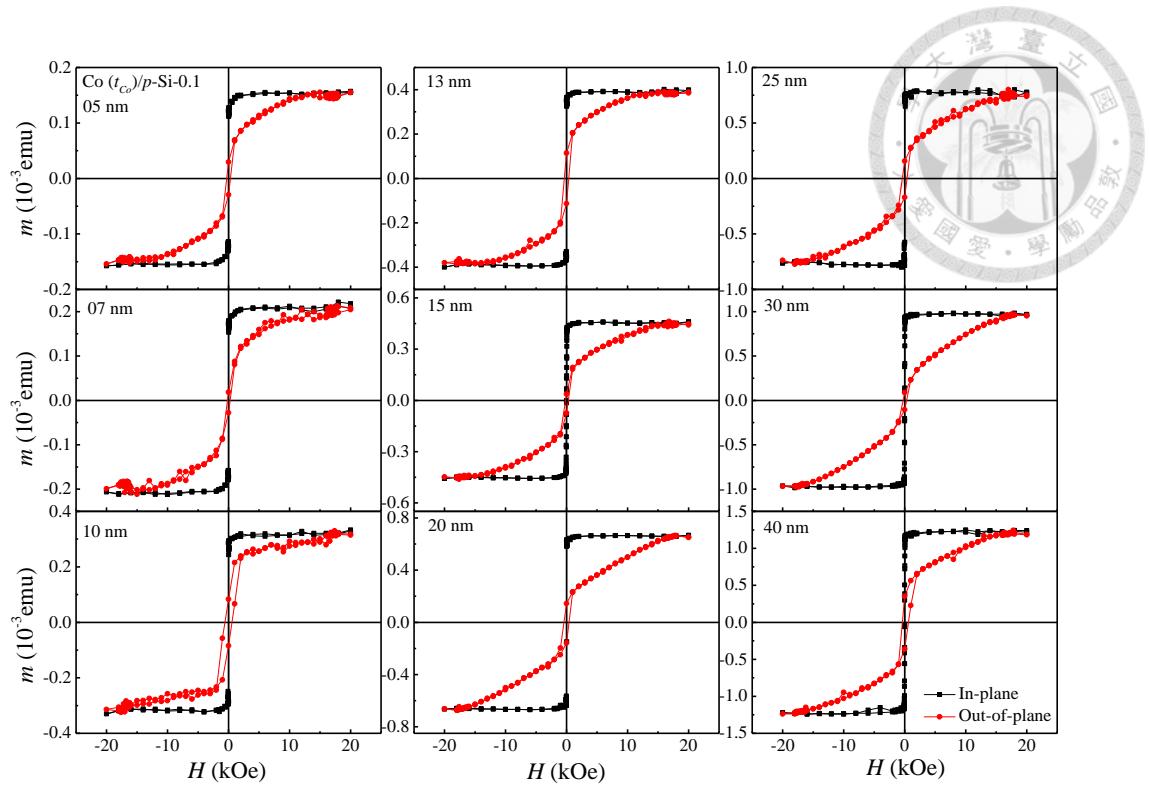


Fig. 4.6 The $M - H$ loops of $\text{Co}(t_{\text{Co}})/p\text{-Si-0.1}$ and the t_{Co} change from 5 nm to 40 nm.

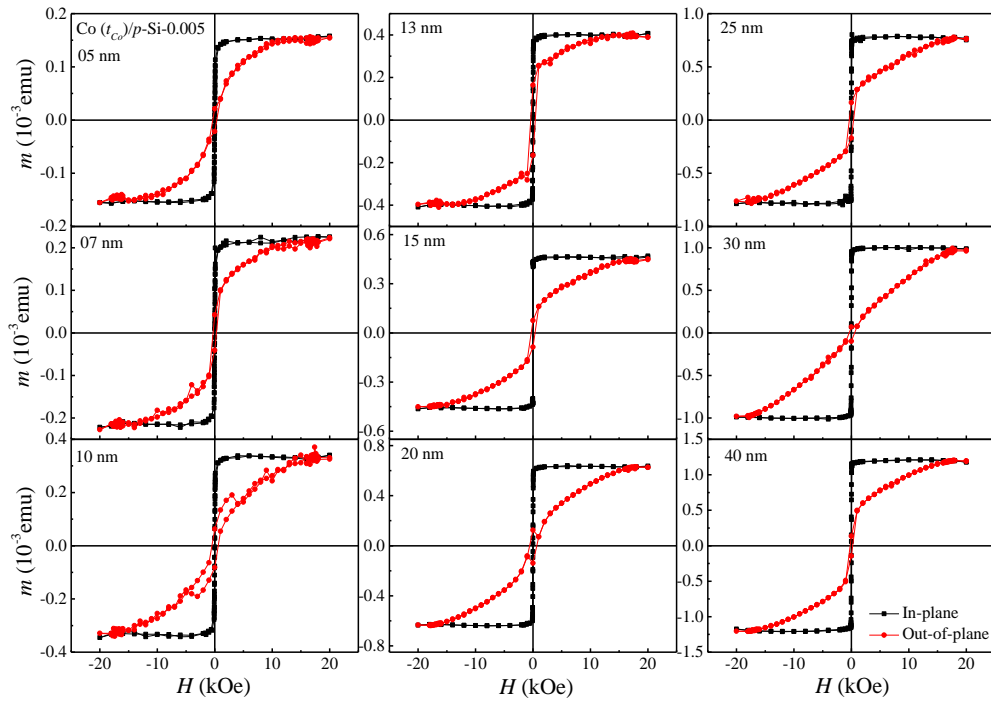


Fig. 4.7 The $M - H$ loops of $\text{Co}(t_{\text{Co}})/p\text{-Si-0.005}$ and the t_{Co} change from 5 nm to 40 nm.

The black squares display $M - H$ loop with in-plane field and the red circles display $M - H$ loop with out-of-plane field. The $M - H$ loops show that the easy axis is in the films plane and the hard axis is along the out-of-plane direction. The thickness-dependence data of saturation magnetic moment (m_s) are plotted in Fig. 4.8 and the m_s is linear dependence on t_{Co} . The M_s and magnetic dead layer (MDL) are extracted from slope and intercept of linear fit of $m_s - t_{Co}$ curve (red solid line in the Fig. 4.8), respectively. The M_s is $1264 \pm 20 \text{ emu/cm}^3$ which is smaller than bulk (1400 emu/cm^3) and the MDL is not apparent for Co thin films.

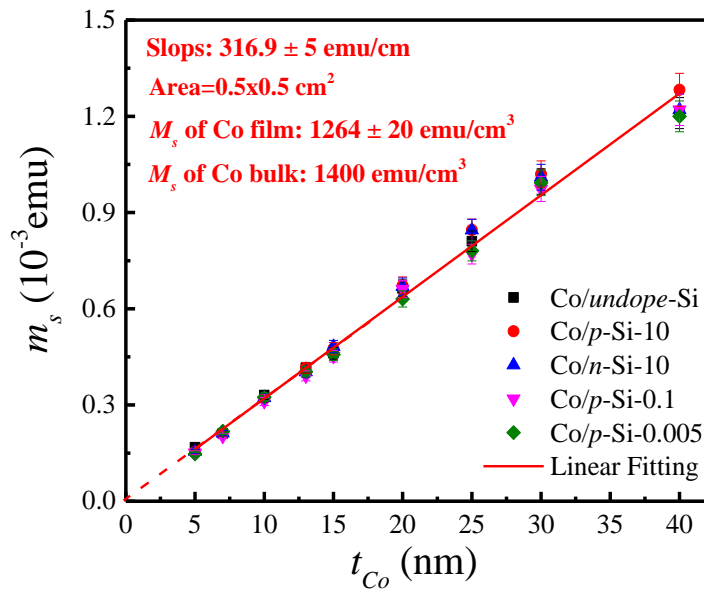


Fig. 4.8 The $m_s - t_{Co}$ curve for sample A and the red solid line is a linear fitting result.

The K_{eff} and $4\pi M_{eff}$ are described by Eq. 4.2, Eq.4.3 and Eq.4.4

$$K_{eff} = \frac{1}{2}(M_s \times H_k) = K_v + \frac{2K_s}{t_{FM}} \quad \text{Eq. 4.2}$$

$$K_{eff} \times t_{FM} = K_v \times t_{FM} + 2K_s \quad \text{Eq. 4.3}$$

$$4\pi M_{eff} = 4\pi M_s + \frac{2K_s}{M_s t_{FM}} \quad \text{Eq. 4.4}$$

where the terms K_v and K_s are volume anisotropy energy and surface anisotropy energy, respectively. The t_{FM} is the thickness of FM layer. The thickness-dependence data of H_k are plotted in Fig. 4.9 and the H_k as a function of t_{Co} . The $K_{eff} \times t_{Co}$ versus t_{Co} are plotted in the Fig. 4.10 (a)~(e) for Co/*undoped*-Si, Co/*p*-Si-10, Co/*n*-Si-10, Co/*p*-Si-0.1, Co/*p*-Si-0.005, respectively. The value of $K_{eff} \times t_{Co}$ is linear dependence on t_{Co} for sample A. The linear fitting results (red solid line) are shown in the Fig. 4.10 and it agrees with the Eq. 4.3. The K_v and K_s are extracted from intercept and slope of linear fit of $K_{eff} \times t_{FM} - t_{Co}$ curve, respectively. The values of K_v and K_s are listed in Table 4.2 and the results are close to literature report¹⁰⁰ (-7.5 Merg/cm³ and 1.7 erg/cm²).

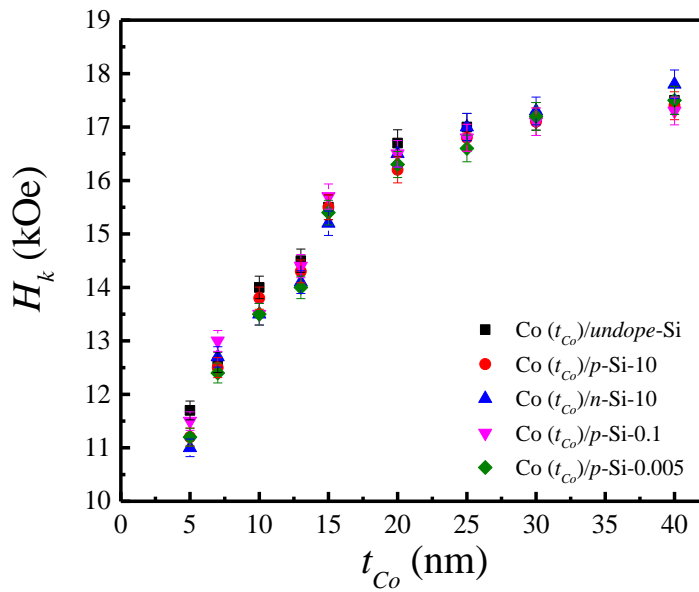


Fig. 4.9 The $H_k - t_{Co}$ curve for sample A.

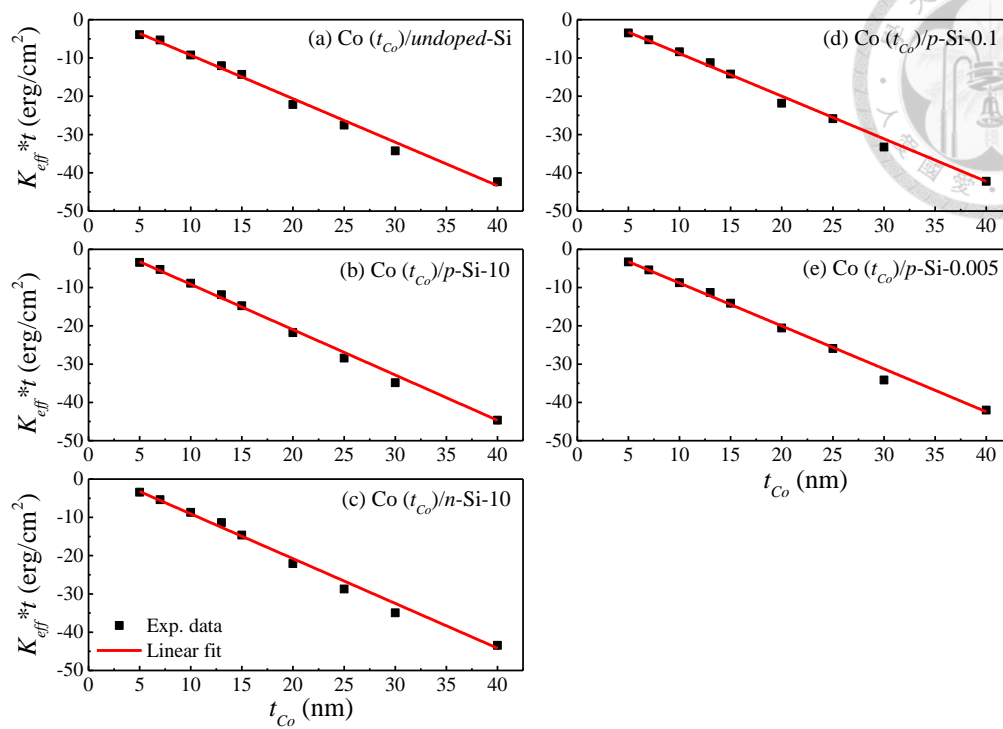


Fig. 4.10 The $K_{eff} \times t - t_{co}$ curve for sample A and the red solid lines are linear fitting result.

Table 4.2 The value of K_v and K_s of Sample A are extracted from intercept and slope of linear fitting result, respectively.

| Sample | Co/ <i>undoped-Si</i> | Co/ <i>n-Si-10</i> | Co/ <i>p-Si-10</i> | Co/ <i>p-Si-0.1</i> | Co/ <i>p-Si-0.005</i> |
|----------------------------------|--------------------------|-----------------------|-----------------------|------------------------|--------------------------|
| K_v (Merg/cm ³) | -11.3±4.2 | -11.6±4.0 | -11.8±3.3 | -11.1±3.5 | -11.2±2.7 |
| K_s (erg/cm ²) | 1.04±0.19 | 1.30±0.17 | 1.34±0.14 | 1.15±0.15 | 1.19±0.11 |

The values of $4\pi M_{eff}$ are obtained using Eq. 4.4 and its values are shown in Fig. 4.11. A larger value of $4\pi M_{eff}$ for Co (5) film is due to surface anisotropy. The VSM

results show that magnetic properties of Co films are independent of carrier concentration and type of Si-substrate.

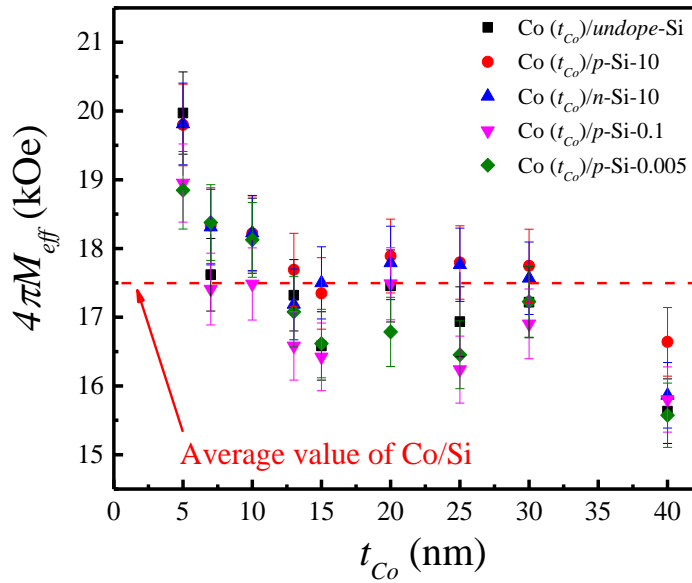


Fig. 4.11 The value of $4\pi M_{eff}$ for sample A.

4.1.3 Ferromagnetic resonance and inverse spin Hall effect results of reference sample [Pt (10 nm)/Co (t_{Co} nm)/unpoded]

The techniques of FMR-SP and ISHE-probe spin current are mainly applied on the FM/NM bilayer system. In the previous studies, researchers used heavy metals, for examples, Pt as a spin current detector because Pt has strong SOI.^{27,78-81,84,101} Therefore, the Pt/Co bilayer structure [Pt (10 nm)/Co (t_{Co})/unpoded] is a reference sample in this work.

The black line in Fig. 4.12 (a) shows the typical FMR spectrum (dI/dH vs. H) for Pt/Co (10)/undoped sample. The FMR spectrum is measured with condition that power

of microwave (P_{MW}) is 100 mW and angle of θ_H is 0° . The corresponding dc voltage signals (V vs. H) are displayed on Fig. 4.12 (b). The $V(\theta_H)$ is measured under FMR condition with two different θ_H : 0° (black line) and 180° (red line). The $V(\theta_H)$ shows an opposite sign when the θ_H direction changes from 0° to 180° , which indicates the θ_H dependence of voltage. This result is consistent with the relation of j_s and j_c in Eq.26.

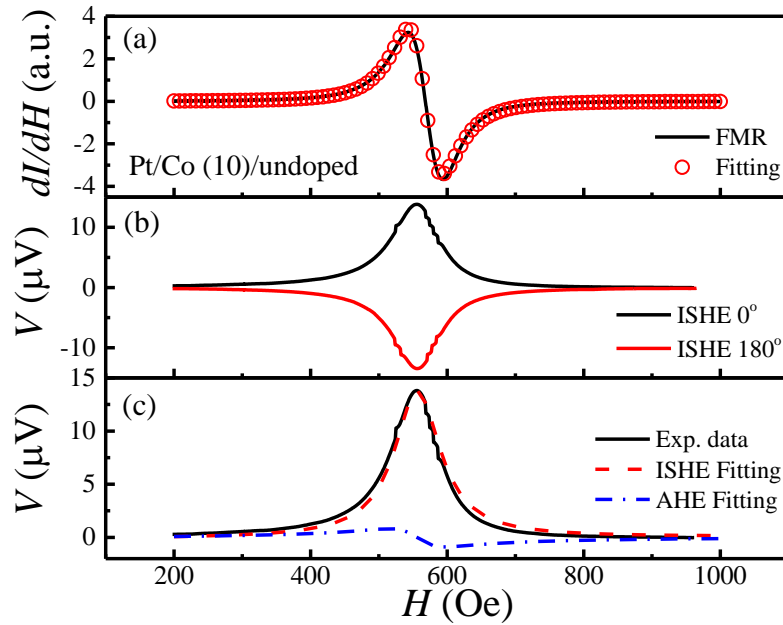


Fig. 4.12 (a) The FMR spectrum for Pt/Co (10)/undoped sample (dI/dH vs. H) and the open circle is fitting result by differential form of Lorentzian (b) voltage signals (V vs. H) for Pt/Co (10)/undoped sample (c) The black curve is experiment data; red dash and blue dash-dot curves are ISHE and AHE fits to Eq.4.6.

The H_r and ΔH are extracted by fitting the FMR spectrum using differential form of Lorentzian Eq. 4.5. The H_r and ΔH are 567 Oe and 85 Oe, respectively for Pt/Co (10)/undoped sample. The fitting result (open circle) is shown in Fig. 4.12 (a).

$$\frac{dI}{dH} \propto \frac{\Delta H(H-H_r)}{((H-H_r)^2 + \Delta H^2)^2} \quad \text{Eq. 4.5}$$

The voltage signal can be decomposed into two parts by Eq. 4.6: symmetric and asymmetric terms.^{27,78} The symmetric term is due to ISHE and the asymmetric term is contributed by the AHE.

$$V = V_{s(ISHE)} \frac{\Delta H^2}{(H-H_r)^2 + \Delta H^2} + V_{as(AHE)} \frac{-2\Delta H(H-H_r)}{(H-H_r)^2 + \Delta H^2} \quad \text{Eq. 4.6}$$

where V_{ISHE} and V_{AHE} are ISHE voltage and AHE voltage, respectively. Fig. 4.12 (c) shows the fitting result of V using Eq 4.6 where the black, blue dash and red dash-dot curves are experimental data, fitting curves of ISHE and AHE, respectively. The V_{ISHE} and V_{AHE} are around 13.8 and 0.8 μV respectively at 100 mW microwave excitation.

Fig. 4.13 (a) and (b) show P_{MW} dependent FMR spectral and voltage signals, respectively, for Pt/Co (10)/undoped sample. The intensity of FMR spectrum and signal of voltage increase with increasing P_{MW} from 20 to 100 mW. Fig. 4.14 shows that the V_{ISHE} linearly increases with increasing P_{MW} from 20 to 100 mW and the red solid line is the linear fitting result.

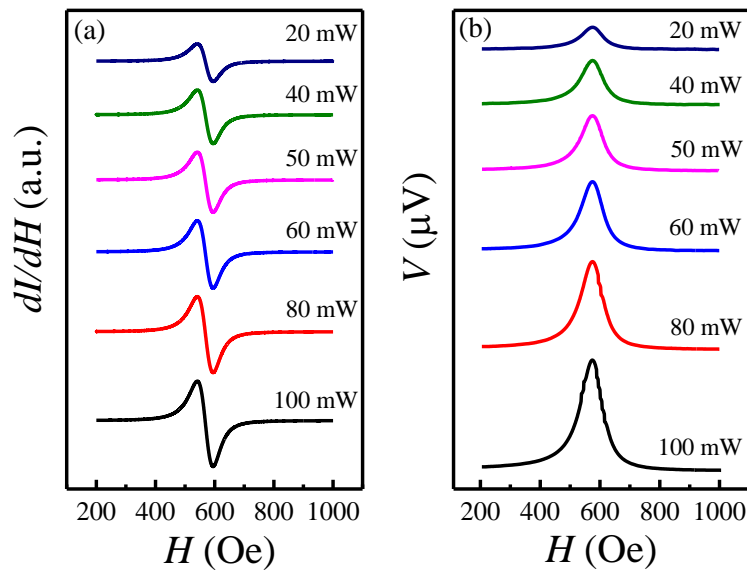


Fig. 4.13 The P_{MW} dependent (a) FMR spectra and (b) voltage signals for Pt/Co

(10)/undoped sample.

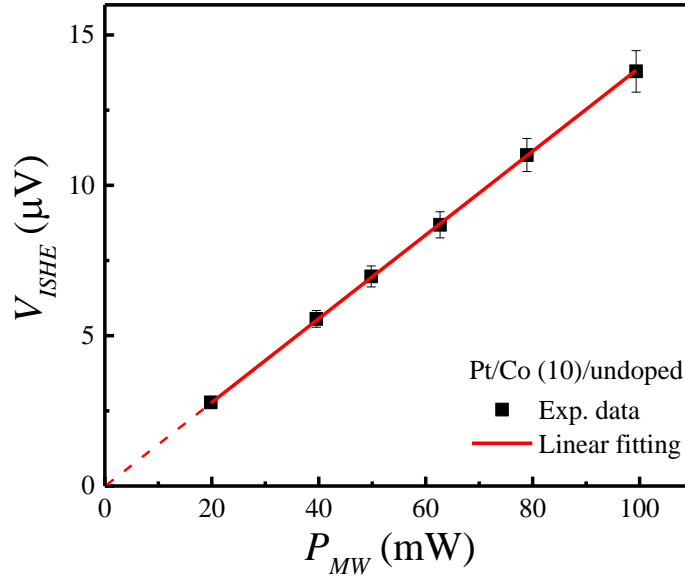


Fig. 4.14 The plot of V_{ISHE} v.s. P_{MW} for Pt/Co (10)/undoped sample which P_{MW} is varied from 20 to 100 mW and the red solid line is the linear fitting result.

The θ_{ISHE} is the conversion rate of spin current to charge current via ISHE and described by⁷⁸

$$I_c = \theta_{ISHE} w \left(\frac{2e}{\hbar} \right) \lambda_s \tanh \left(\frac{t_N}{2\lambda_s} \right) j_s^0 \quad \text{Eq. 2.46}$$

$$j_s^0 = \frac{g_{eff}^{\uparrow\downarrow} \gamma^2 \hbar r_f^2 [4\pi M_s \gamma + \sqrt{(4\pi M_s)^2 \gamma^2 + 4\omega^2}]}{8\pi \alpha^2 [(4\pi M_s)^2 \gamma^2 + 4\omega^2]} \quad \text{Eq. 4.7}$$

since the effective damping constant (α) comes from three contributions: intrinsic damping (α_0), spin pumping damping (α_{SP}) and eddy-current damping (α_{EC}), the α can be described by¹⁰²⁻¹⁰⁴

$$\alpha = \alpha_0 + \alpha_{SP} + \alpha_{EC} = \alpha_0 + \frac{\gamma \hbar}{4\pi M_s} g_{eff}^{\uparrow\downarrow} t_{FM}^{-1} + C_{EC} t_{FM}^2 \quad \text{Eq. 4.8}$$

$$C_{SP} = \frac{\gamma \hbar}{4\pi M_s} g_{eff}^{\uparrow\downarrow}$$

where C_{EC} and C_{SP} are the coefficient of spin pumping and eddy-current, respectively. According to the Eq. 2.46, Eq. 4.7 and Eq. 4.8, the value of I_c is dependent on t_{FM} and the θ_{ISHE} can be extracted by fitting the thickness-dependence data of I_c . Fig. 4.15 shows the data of $I_c - t_{Co}$ for reference sample and fitting result (red solid curve) using the Eq. 2.46, Eq. 4.7 and Eq. 4.8 by inserting the following essential parameters: $g_{eff}^{\uparrow\downarrow}$ is $(6.0 \pm 0.3) \times 10^{19} \text{ m}^{-2}$, α_0 is 0.067 (The detail calculation of α_0 , α and $g_{eff}^{\uparrow\downarrow}$ are shown in section 4.1.6), γ is $1.77 \times 10^{19} \text{ C} \cdot \text{kg}^{-1}$, h_{rf} is $1.4 \times \sqrt{P_{MW}} \text{ G}$, P_{MW} is 100 mW, \hbar is $1.054 \times 10^{-34} \frac{\text{kg} \cdot \text{m}^2}{\text{s}^2} \text{ S}$, M_s is 1264 emu/cm^3 and λ_s is 7 nm.¹⁰⁵ In this work, the θ_{ISHE} of Pt is 5.3×10^{-2} and this values is comparable to literature report (5.6×10^{-2}) for Pt/Co system studied by the spin pumping method.⁸¹

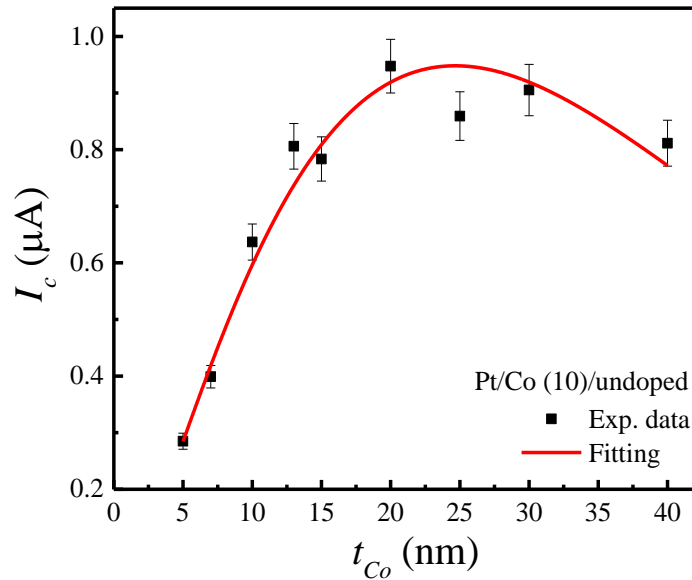


Fig. 4.15 The data of $I_c - t_{Co}$ curves for reference samples and the red solid curve is the fits to Eq. 2.46, Eq. 4.7 and Eq. 4.8.

4.1.4 Ferromagnetic resonance results of Co (t_{Co} nm)/Si

Fig. 4.16 shows the FMR spectra (black line) for Pt/Co (10)/undoped and all Co (10)/Si samples. The H_r and ΔH are extracted by fitting the FMR spectrum using Eq. 4.5 and the fitting results (open circle) are shown in Fig. 4.16. The H_r and ΔH are 550 Oe and 80 Oe, respectively, for all Co (10)/Si samples.

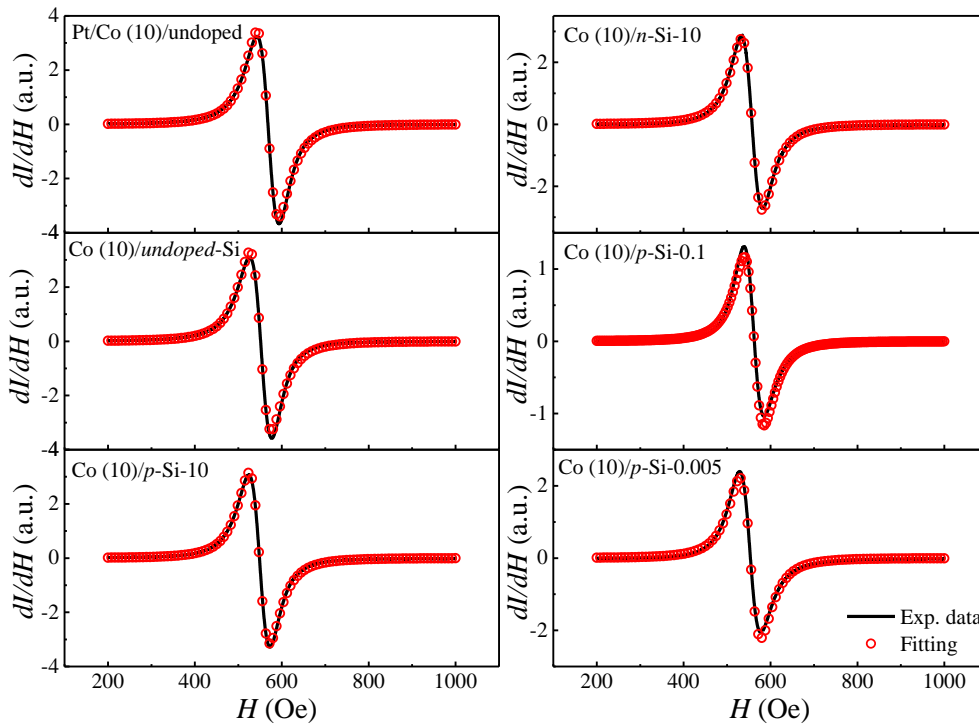


Fig. 4.16 The FMR spectra (dI/dH vs. H) for Pt/Co (10)/undopen and all Co (10)/Si samples. The open circle is fitting result using differential form of Lorentzian.

The H_r and ΔH versus t_{Co} are shown in the Fig. 4.17 (a) and (b), respectively, for reference and sample A. For sample A, the H_r and ΔH depend on t_{Co} but neither on doping concentration nor carrier type of Si. The H_r has a minimum value of 550 Oe for all Co (10)/Si samples and ΔH has a minimum value of 70 Oe for all Co (13)/Si

samples. The H_r and ΔH of sample A (red dash line in Fig. 4.17) are slightly smaller than reference sample (black dash line in Fig. 4.17).

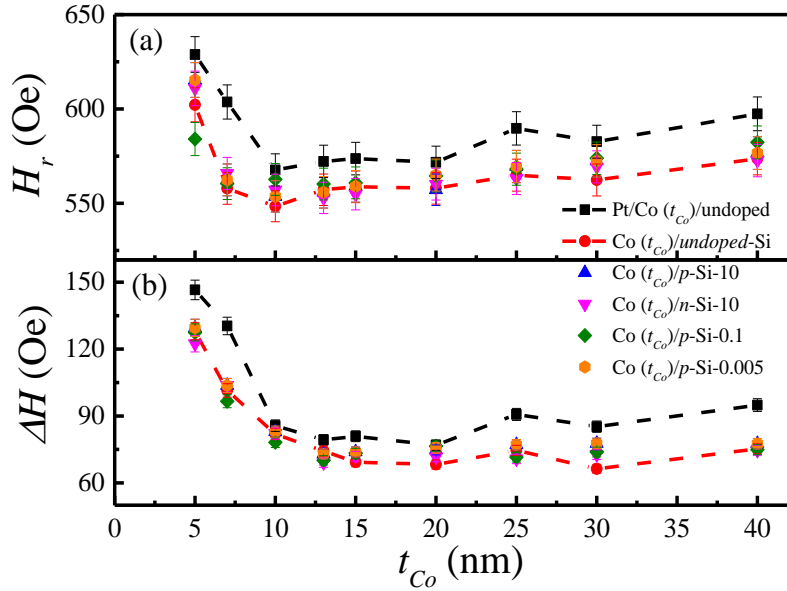


Fig. 4.17 The (a) H_r and (b) ΔH versus t_{Co} changing from 5 nm to 40 nm for reference and sample A, respectively.

The data of $H_r(\theta_H)$ and $\Delta H(\theta_H)$ are shown in Fig. 4.18 (a) and (b), respectively, for Pt/Co (10)/undoped and all Co (10)/Si samples (Due to the instrument limit, we could not measure the FMR spectra at the out of plane, θ_H is 90° , for all samples). The equilibrium angle of magnetization (θ_M), g -factor and gyromagnetic ratio (γ) are important parameters for magnetic materials. These can be calculated by combining Eq. 4.9 and Eq. 4.10 with $4\pi M_{eff}$ (This value is obtained from VSM measurement), data of $H_r(\theta_H)$ and $\Delta H(\theta_H)$.

$$\left(\frac{\omega}{\gamma}\right)^2 = H_1 \times H_2 \quad \text{Eq. 4.9}$$

$$2H_r \sin(\theta_H - \theta_M) = 4\pi M_{eff} \sin(2\theta_M) \quad \text{Eq. 4.10}$$

$$H_1 = [H_r \cos(\theta_H - \theta_M) - 4\pi M_{eff} \cos^2 \theta_M]$$

$$H_2 = [H_r \cos(\theta_H - \theta_M) - 4\pi M_{eff} \cos 2\theta_M]$$

the $\omega = 2\pi f$, f is the microwave frequency. The red solid curve in Fig. 4.18 (a) is the calculated results of $H_r(\theta_H)$ using Eq. 4.9 and Eq. 4.10 which matches with experimental data. The θ_H dependence of the θ_M are plotted in Fig. 4.19 and the behavior of θ_M are similar for all samples. The results show that magnetization is lying on film plane at $\theta_H < 60^\circ$ and raise to out-of-plane direction at $\theta_H > 60^\circ$.

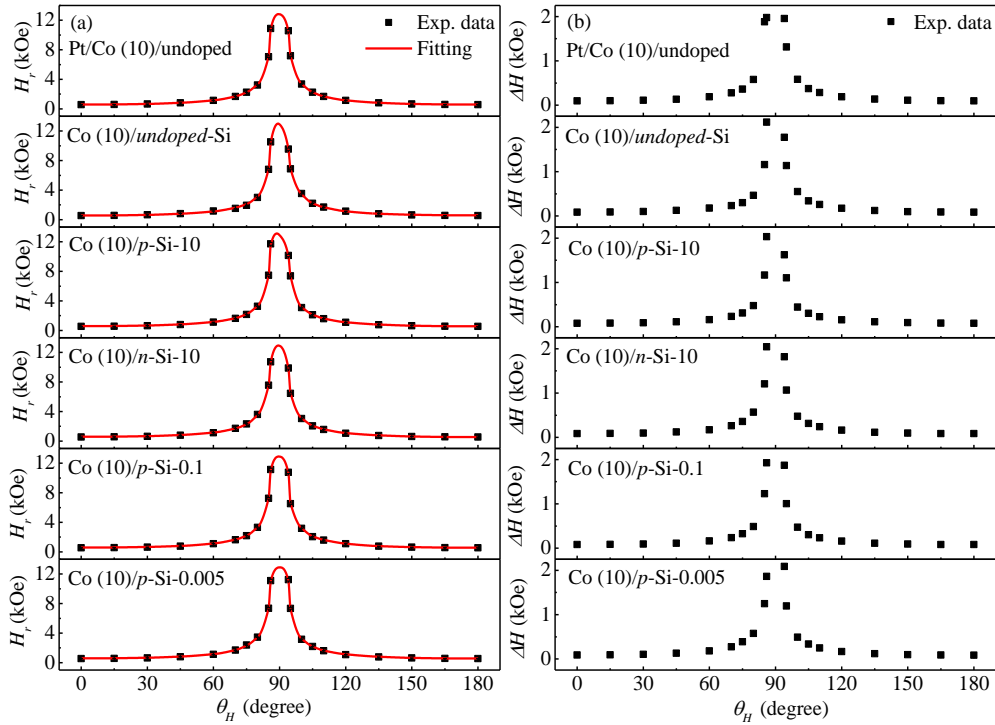


Fig. 4.18 The angular-dependence data of (a) H_r , calculational results of H_r (red line) and (b) ΔH for Pt/Co (10)/undopen and all Co (10)/Si samples, respectively.

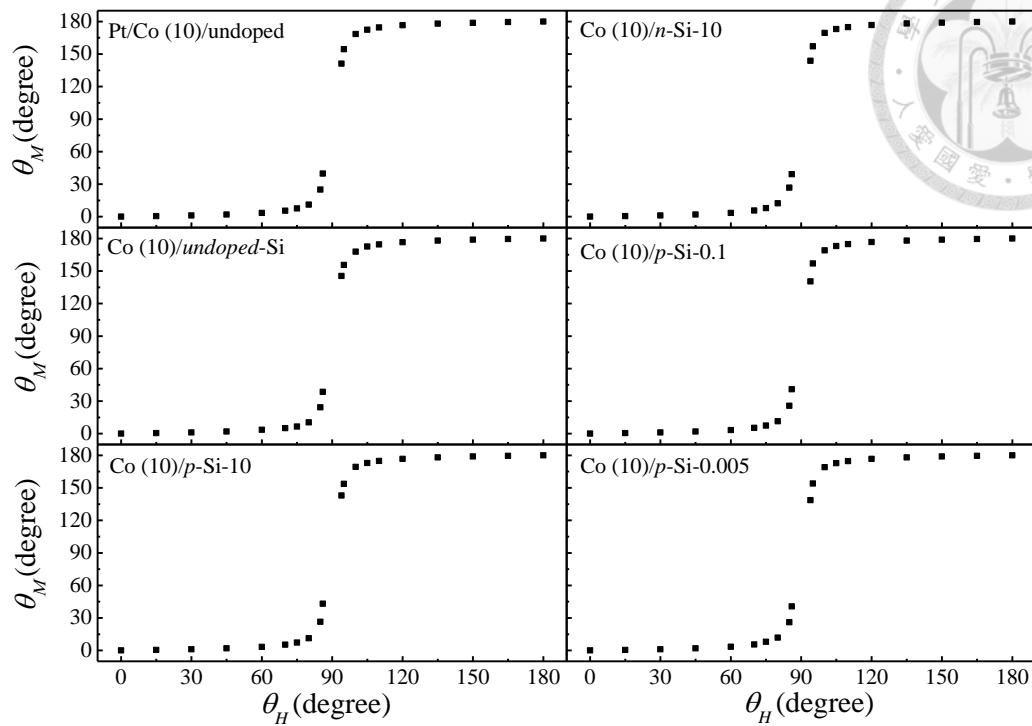


Fig. 4.19 The θ_M versus θ_H for Pt/Co (10)/undopen and all Co (10)/Si samples, respectively.

The gyromagnetic ratio and g-factor versus t_{Co} are plotted in the Fig. 4.20 (a) and (b), respectively. The mean values of gyromagnetic ratio and g-factor are $1.83 \times 10^{11} \text{ rads}^{-1} \text{ T}^{-1}$ and 2.15, respectively. The value of g-factor is in good agreement with theoretical value for Co thin film (2.16).¹⁰⁶

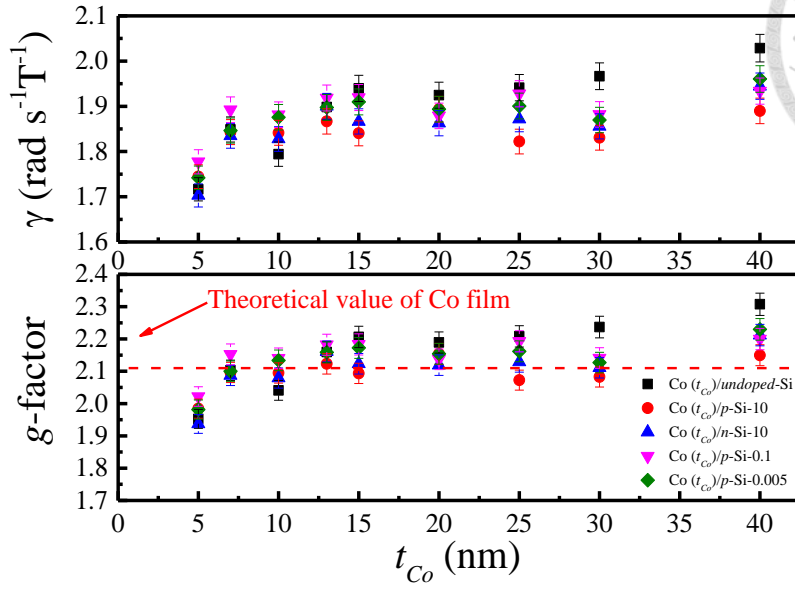


Fig. 4.20 The value of (a) gyromagnetic ratio and (b) g -factor for sample A.

4.1.5 Effective damping constant and effective spin mixing

conductance for Co (t_{Co} nm)/Si

The efficiency of spin current injection at the interface FM/SC (NM) is denoted as the effective spin mixing conductance ($g_{eff}^{\uparrow\downarrow}$). In most of the spin pumping experiments, the $g_{eff}^{\uparrow\downarrow}$ value was obtained by the difference of effective damping constants (α) for single FM layer and FM/NM bilayer.^{82,83} However, it was not so accurate since the α depends on thickness of FM layer. In this work, we made a series of Co thin film with different thicknesses to obtain the best fit of $g_{eff}^{\uparrow\downarrow}$ for Co/Si samples.

The α can be experimentally determined by fitting the data of $H_r(\theta_H)$ and $\Delta H(\theta_H)$ based on the following Eq. 4.11

$$\Delta H_{pp}^{hom} = \frac{1}{\sqrt{3}} \frac{\alpha}{M_s} (H_1 + H_2) \times \left| \frac{d(\frac{\omega}{\gamma})}{dH_r} \right|^{-1} \quad \text{Eq. 4.11}$$

$$H_1 = [H_r \cos(\theta_H - \theta_M) - 4\pi M_{eff} \cos^2 \theta_M]$$

$$H_2 = [H_r \cos(\theta_H - \theta_M) - 4\pi M_{eff} \cos 2\theta_M]$$

where γ is gyromagnetic ratio, $\omega = 2\pi f$, f is the microwave frequency, M_s is the saturation magnetization, M_{eff} is the effective magnetization, ΔH_{pp}^{hom} is the peak to peak linewidth ($\Delta H = \sqrt{3}\Delta H_{pp}^{hom}$). Based on the calculated result, the α (black dot) as a function of t_{Co} and plotted in Fig. 4.21 for reference sample and sample A.

In Fig. 4.21, the red solid curve is fitting curve according to Eq. 4.8; while the blue dash and green dash-dot curves describe $\alpha_0 + \alpha_{SP}$ and $\alpha_0 + \alpha_{EC}$, respectively. It is noted that the spin pumping term is dominant for thinner Co layers (< 25 nm); while the eddy-current damping term is dominant for thicker Co layer (> 25 nm).

$$\alpha = \alpha_0 + \alpha_{SP} + \alpha_{EC} = \alpha_0 + \frac{\gamma\hbar}{4\pi M_s} g_{eff}^{\uparrow\downarrow} t_{FM}^{-1} + C_{EC} t_{FM}^2 \quad \text{Eq. 4.8}$$

The value of α_0 is obtained from fitting result of Co (t_{Co})/undoped-Si because the spin current cannot injects into undoped-Si. The value of C_{SP} and C_{EC} are listed in Table 4.3.

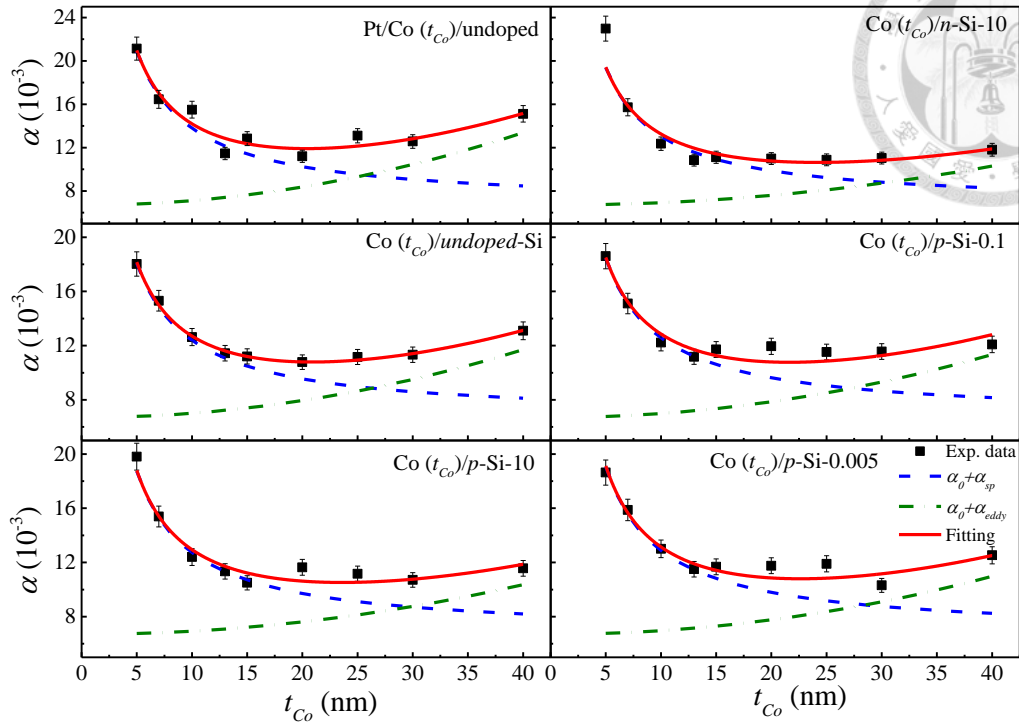


Fig. 4.21 The α versus t_{Co} curve for reference sample and sample A. The red solid lines, blue and green dash-dot curves are described $\alpha_0 + \alpha_{SP} + \alpha_{EC}$, $\alpha_0 + \alpha_{SP}$ and $\alpha_0 + \alpha_{EC}$ fitting curves according to Eq. 4.8, respectively.

The $g_{eff}^{\uparrow\downarrow}$ is derived from Eq. 4.8 by inserting the following essential parameters: γ is $1.77 \times 10^{19} \text{ C} \cdot \text{kg}^{-1}$, \hbar is $1.054 \times 10^{-34} \frac{\text{kg} \cdot \text{m}^2}{\text{s}^2}$ S, M_s is 1264 emu/cm^3 . The obtained values of $g_{eff}^{\uparrow\downarrow}$ for sample A are shown in the fourth row of Table 4.3 and Fig. 4.22, indicating that the efficiency of spin injection in all samples is roughly the same within the uncertainty of data. The reason for that $g_{eff}^{\uparrow\downarrow}$ (average value is $5.0 \times 10^{19} \text{ m}^{-2}$) is independent of doping concentration and carrier type may be due to the same interface of Co and Si (Co/SiO₂/Si). The $g_{eff}^{\uparrow\downarrow}$ of reference sample is $6.0 \times 10^{19} \text{ m}^{-2}$ and the value is slightly larger than Co/Si. This result shows that the spin pumping efficiency of Pt/Co interface is larger than Co/Si interface and mismatch with linewidth result.

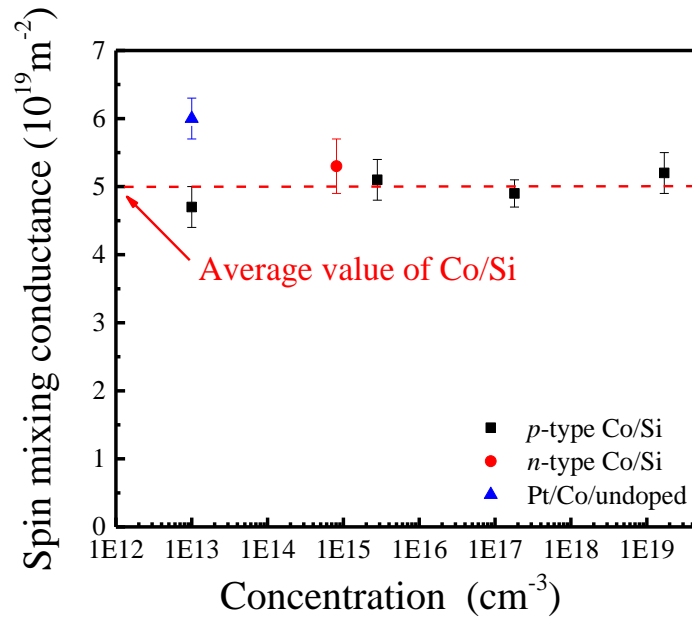


Fig. 4.22 The $g_{eff}^{\uparrow\downarrow}$ v.s. N for reference sample and sample A.

Table 4.3 The fitting results of damping constant and the value of effective spin mixing conductance for reference sample and sample A.

| Sample name | Co/ <i>undoped-Si</i> | Co/ <i>n-Si-10</i> | Co/ <i>p-Si-10</i> | Co/ <i>p-Si-0.1</i> | Co/ <i>p-Si-0.005</i> | Pt/Co/ <i>undoped-Si</i> |
|---|--------------------------|-----------------------|-----------------------|------------------------|--------------------------|-----------------------------|
| α_0 (10^{-3}) | | | | | | |
| C_{SP} (10^{-11}) | | | | | | |
| C_{CE} (10^{12}) | | | | | | |
| $g_{eff}^{\uparrow\downarrow}$ ($10^{19}m^{-2}$) | | | | | | |



4.1.6 Inverse spin Hall effect of Co (t_{Co} nm)/Si

In this section, we will discuss the spin pumping effect in the Co/Si samples. The Fig. 4.23 (a) ~ (f) and (g) ~ (l) show the FMR spectra and voltage signals, respectively, for Pt/Co (10)/undoped and all Co (10)/Si samples. The $V(\theta_H)$ shows an opposite sign when the θ_H direction changes from 0° to 180° .

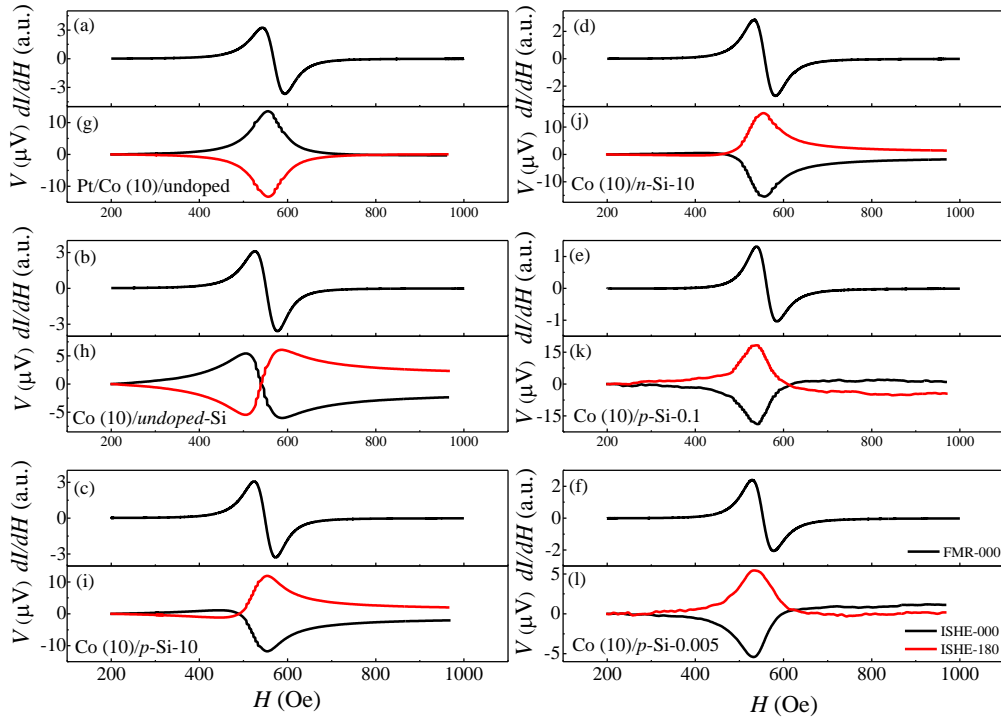


Fig. 4.23 The (a)~(f) FMR spectra with θ_H is 0° and (g)~(l) voltage signals θ_H are 0° and 180° for Pt/Co (10)/undoped and all Co (10)/Si samples, respectively.

Fig. 4.24 shows the fitting results of V using Eq. 4.6 for Pt/Co (10)/undoped and all Co (10)/Si samples. The black, red dash and blue dash-dot curves are the experimental data, symmetric and asymmetric fitting curves, respectively. From the fitting results, a

positive V_s value of 13.8 and 2.15 μV is obtained at 100 mW for the Pt/Co (10)/undoped and Co (10)/undoped-Si samples, respectively. On the other hand, a negative V_s value of -13.49, -8.68, -19.45, -5.75 μV is obtained at 100 mW for Co (10)/n-Si-10, Co (10)/p-Si-10, Co (10)/p-Si-0.1 and Co (10)/p-Si-0.005 samples, respectively. The values of V_s , as shown in Fig. 4.25, follow linearly dependence with P_{MW} increasing from 20 to 100 mW for Pt/Co (10)/undoped and all Co (10)/Si samples. These results show θ_H and P_{MW} dependence of V_s which is consistent with the spin pumping theory. Therefore, the V_s is treated as the inverse spin Hall voltage, V_{ISHE} , and V_{as} is treated as the anomalous Hall voltage, V_{AHE} , respectively.

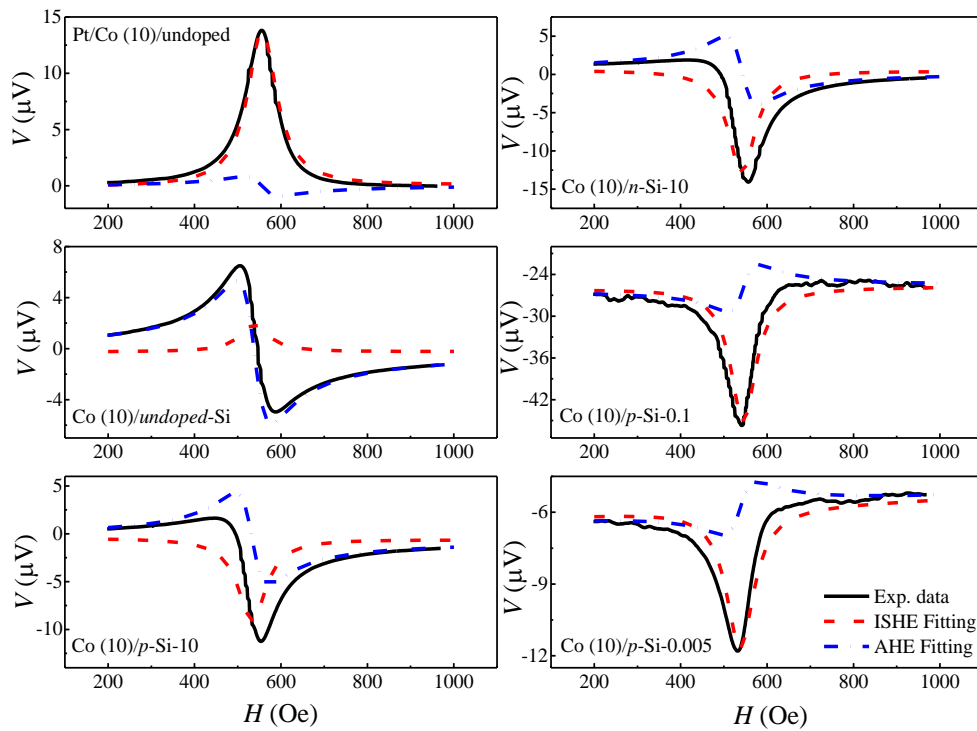


Fig. 4.24 The voltage signals with θ_H is 0° for Pt/Co (10)/undoped and all Co (10)/Si samples. The black, red dash and blue dash-dot curves are experiment data, ISHE and AHE fitting curves, respectively

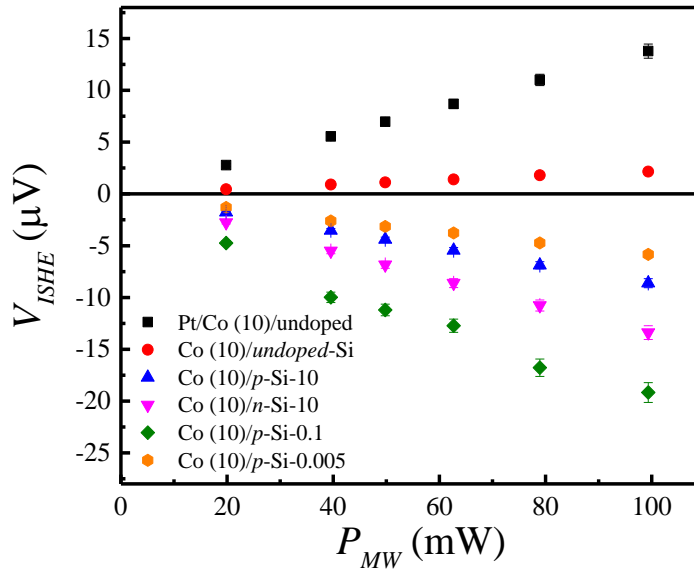


Fig. 4.25 The plot of V_{ISHE} with microwave power which is varied from 20 to 100 mW for all Pt/Co (10)/undoped and all Co (10)/Si samples.

The Eq. 2.26 shows that the sign of V_{ISHE} depends on the direction of spin current. The opposite sign in V_{ISHE} indicates that the spin current flows in two different directions: one is into Si-sub. and the other is out of Si-sub.. Since the V_{ISHE} in the reference sample is positive and the direction of spin current is into the Pt (out of the Si-substrate). On the other hand, the spin current is out of Si-sub. in the Co/undoped-Si sample and conversion to charge current in the Co layer, called as self-induced ISHE.^{107,108} The negative V_{ISHE} shows that the direction of spin current is into the Si-sub. and conversion to charge current in the Si-sub..

The thickness-dependence V_{ISHE} and I_{ISHE} ($\equiv \frac{V_{ISHE}}{R}$) are shown in Fig. 4.26 and 4.27, respectively. The resistance values can be obtained by two different methods: the two-point probe (use in this study) and the equivalent circuit model. The comparison of resultant resistance is shown in Appendix A.



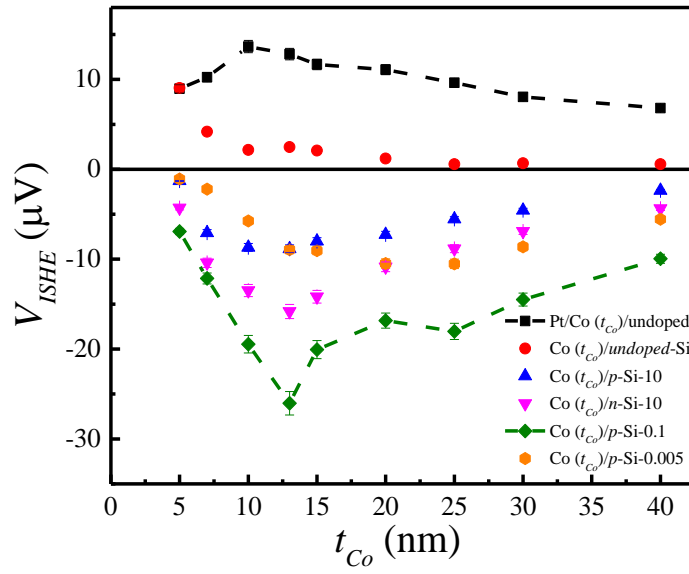


Fig. 4.26 The thickness-dependence data of V_{ISHE} for reference sample and sample A.

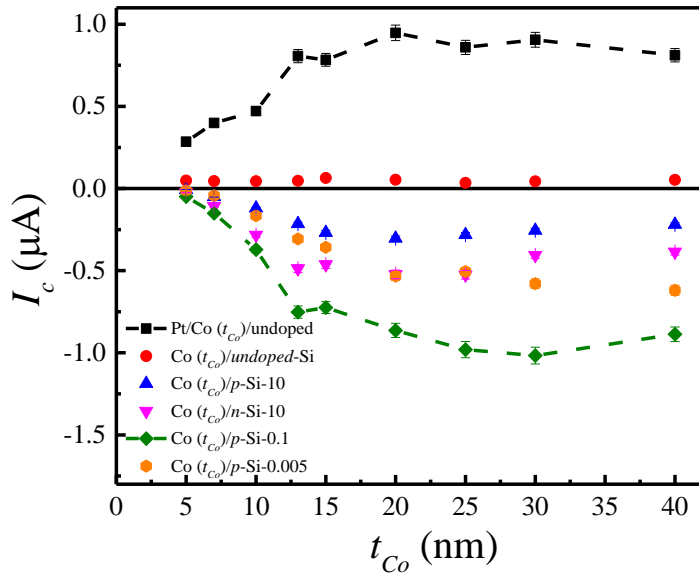


Fig. 4.27 The thickness-dependence data of I_c for reference sample and sample A.

For reference sample, the V_{ISHE} and I_{ISHE} has maximum value at 10 nm and 20 nm, respectively. For Co (t_{Co})/p-Si-10, Co (t_{Co})/n-Si-10, Co (t_{Co})/p-Si-0.1 and Co (t_{Co})/p-Si-0.005, the behavior is similar to the reference sample but observed opposite

signals for V_{ISHE} and I_{ISHE} . For Co (t_{Co})/undoped-Si sample, the V_{ISHE} is decreases with increasing t_{Co} but the I_{ISHE} is independent on t_{Co} .

The data of $V_{ISHE}(\theta)$ is plotted in Fig. 4.28 for Pt/Co (10)/undoped and all Co (10)/Si samples. For Pt/Co (10)/undoped and Co (10)/p-Si-0.005, the $V_{ISHE}(\theta)$ has a close value at low angle and it decreases near $\theta_H = 90^\circ$. For Co (10)/n-Si-10, Co (10)/p-Si-10 and Co (10)/p-Si-0.1, the $V_{ISHE}(\theta)$ decreases with increasing θ_H . The curvature of $V_{ISHE}(\theta) - \theta_H$ curves depends on the doping concentration and carrier type of Si. For Co (10)/undoped-Si, the $V_{ISHE}(\theta)$ has maximum value at θ_H near 80° and 100° . The angular dependent FMR spectra and voltage signals are shown in Appendix B.

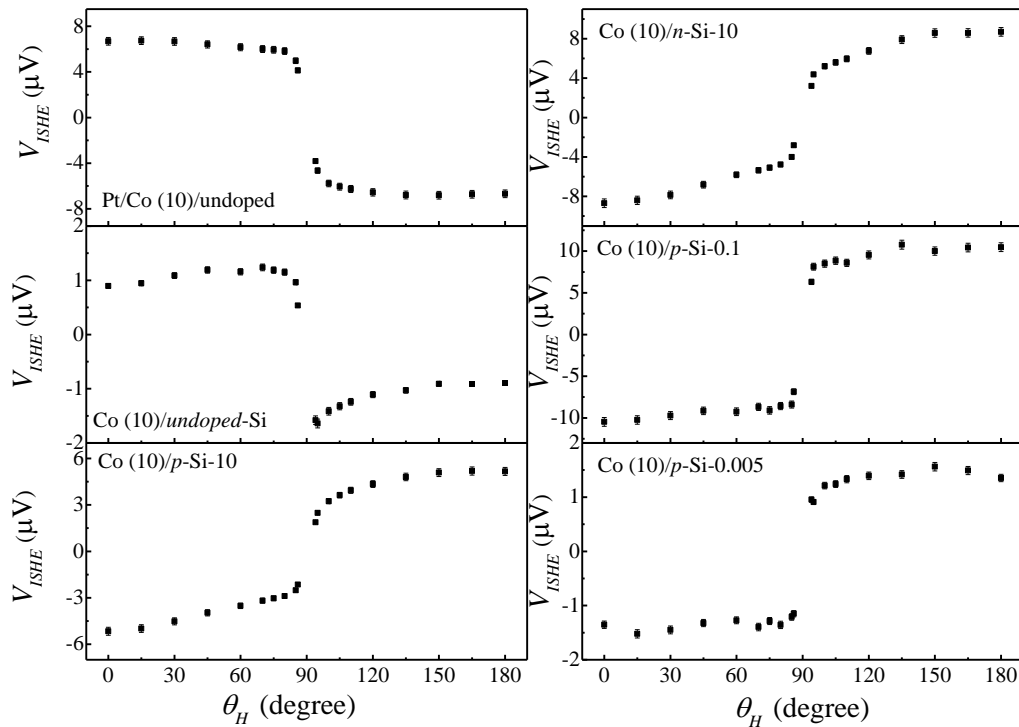


Fig. 4.28 The $V_{ISHE} - \theta_H$ curves for Pt/Co (10)/undoped and all Co (10)/Si samples.



4.1.7 Spin lifetime and spin diffusion length of Si

The spin precession is one of the method used to detect spin lifetime in FM/SC spin pumping system. The free spins in SC makes a precession around the axis parallel to H and gradually relaxes back to a static state after some time, which as called the spin lifetime. In this work, the study of τ_s and θ_{ISHE} of Si is focused on Co/ p -Si-10, Co/ n -Si-10, Co/ p -Si-0.1 and Co/ p -Si-0.005 samples because the spin pumping results showed that the spin current flow into Si layer in these samples.

The τ_s in Si can be extracted by fitting the normalized $V_{ISHE}(\theta)$ using equation Eq. 2.50 and Eq. 2.51.

$$V_{ISHE}(\theta_H) = A \times j_s^0 \times \left[\cos \theta_H \cos(\theta_H - \theta_M) \int_0^{t_{sc}} e^{-x/\sqrt{D_N \tau_s}} dx + \sin \theta_H \sin(\theta_H - \theta_M) \int_0^{t_{sc}} e^{-x/\sqrt{\frac{D_N \tau_s}{1+i\omega_L \tau_s}}} dx \right]$$

Eq. 2.51

the normalized value of $V_{ISHE}(\theta)$ [$V_{ISHE}(\theta_H)/V_{ISHE}(0)$] is plotted in Fig. 4.29 for Co (10)/ n -Si-10, Co (10)/ p -Si-10, Co (10)/ p -Si-0.1 and Co (10)/ p -Si-0.005. In Fig. 4.29, the red solid cures are the fitting result of normalized $V_{ISHE}(\theta)$ by inserting the following essential parameters: the f is 9.8 GHz, γ is $1.77 \text{ rads}^{-1}\text{T}^{-1}$, h_{rf} is $1.4 \times \sqrt{P_{MW}}$ G, P_{MW} is 50 mW, t_{sc} is 500 μm for Si, M_s is 1264 Oe, the θ_M are obtained in section 4.1.5 and the other parameter (α , $g_{eff}^{\uparrow\downarrow}$ and D_N) are listed in Table 4.4. The τ_s and $\lambda_s = \sqrt{D_N \tau_s}$ are obtained from fitting results. For p -type Si, the τ_s/λ_s decreases from 160 ps/380 nm to 12 ps/40 nm, respectively, upon increasing N from 2.8×10^{15} to $1.7 \times 10^{19} \text{ cm}^{-3}$. For n -type Si of N of $8.1 \times 10^{14} \text{ cm}^{-3}$, the τ_s and λ_s are 180 ps and 870 nm, respectively. The computer code for obtaining the normalized value of $V_{ISHE}(\theta_H)$ is shown in Appendix C.

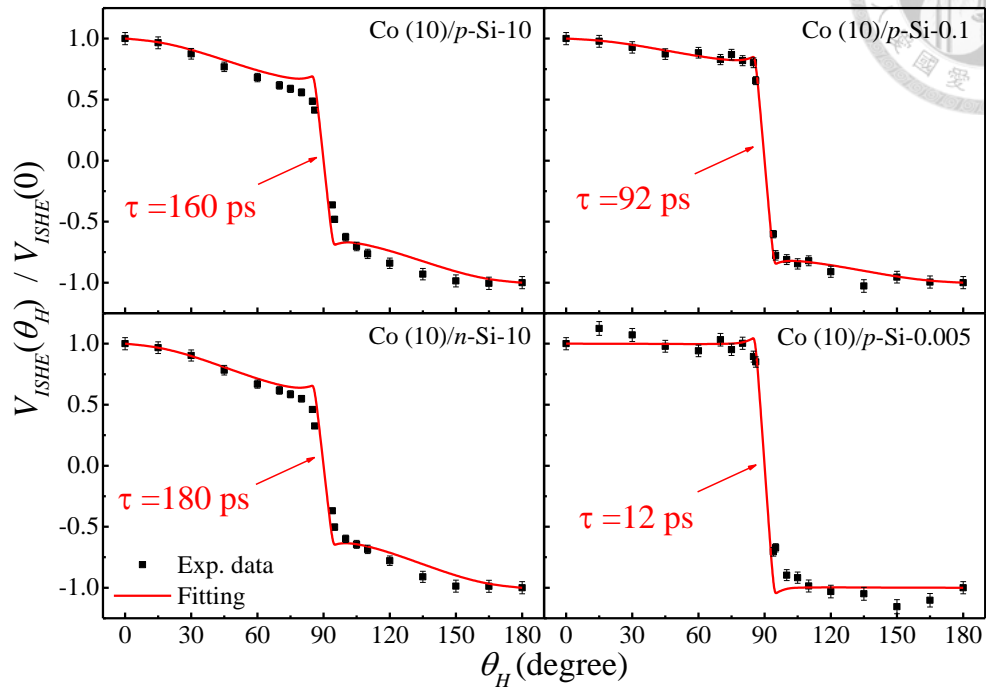


Fig. 4.29 The normalized value of $V_{ISHE}(\theta_H)$ [$V_{ISHE}(\theta_H)/V_{ISHE}(0)$] versus θ_H and the fitting result (red solid curves) for Co (10)/p-Si(10), Co (10)/n-Si(10), Co (10)/p-Si(0.1) and Co (10)/p-Si(0.005) samples.

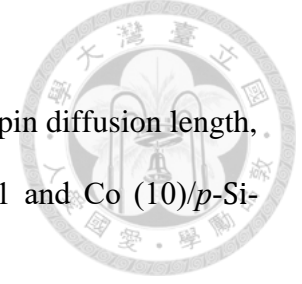


Table 4.4 The calculation result and parameter of spin lifetime and spin diffusion length, respectively for Co (10)/*p*-Si-10, Co (10)/*n*-Si-10, Co (10)/*p*-Si-0.1 and Co (10)/*p*-Si-0.005 samples.

| Sample | Co/ <i>n</i> -Si-10 | Co/ <i>p</i> -Si-10 | Co/ <i>p</i> -Si-0.1 | Co/ <i>p</i> -Si-0.005 |
|--|------------------------|------------------------|-------------------------|---------------------------|
| $g_{eff}^{\uparrow\downarrow}$ (10^{19} m^{-2}) | 5.3±0.4 | 5.1±0.3 | 4.9±0.3 | 5.2±0.3 |
| D_N (cm^2/s) | 42±3 | 9.0±0.5 | 6.0±0.4 | 1.4±0.1 |
| τ_s (ps) | 180±9 | 160±8 | 92±5 | 12±1 |
| λ_s (nm) | 870±44 | 380±20 | 235±12 | 40±2 |

According to theoretical report,⁵³ the SOI of SC depends not only on intrinsic SOC but also the doping concentration and the dopants. This effect is due to donor-induced spin scattering, called as Donor-driven spin relaxation. The spin lifetime can be show as

$$\frac{1}{\tau_s(\varepsilon_k)} = \frac{4\pi N_d m_e \alpha_B^6}{27\hbar^4} \sqrt{2m_e \varepsilon_k} (6|\eta|^2 + 1) \Delta_{SO}^2 \quad \text{Eq. 2.10}$$

the value of Δ_{SO} is dependent on both the SC itself and dopant (host and impurity). Accordingly, the spin lifetime is dependent on doping atom and it is inverse proportional to doping concentration ($\frac{1}{N_d}$). For this study, the relation between τ_s/λ_s and N of Si are displayed in Fig. 4.30 and Table 4.4. The τ_s decrease with increasing N for same doping atom and it is consistent with theoretical report. According to literatures report,^{44,85} the

experimentally obtained spin dynamic parameters are related to the properties of FM material, the roughness of interface and the technique of measurement. The τ_s and λ_s values we obtained (12 ps and 40 nm) are very close to that estimated (9 ps and 56 nm) by Saitoh's group with the same method and similar doping concentration of *p*-Si.³⁰

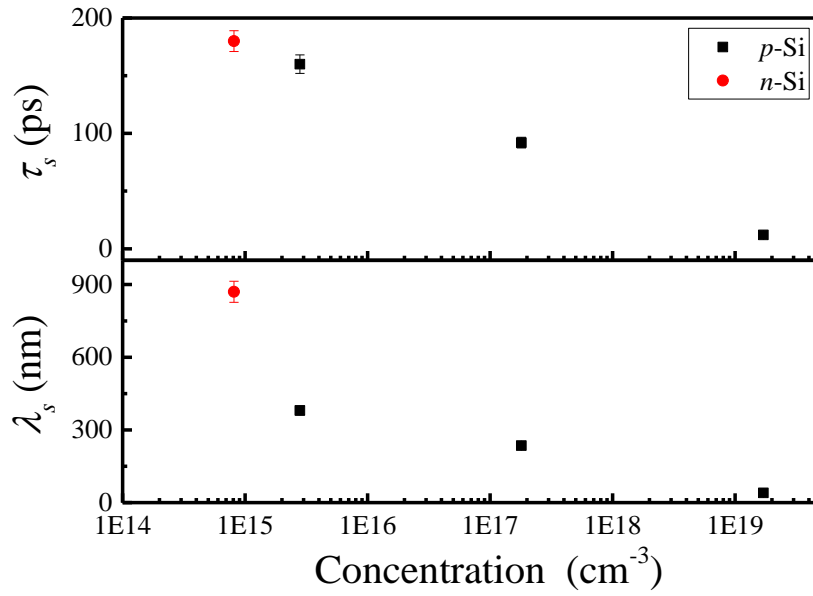


Fig. 4.30 (a) spin lifetime and (b) spin diffusion length versus resistivity of Si for Co (10)/*p*-Si(10), Co (10)/*n*-Si(10), Co (10)/*p*-Si(0.1) and Co (10)/*p*-Si(0.005) samples.

4.1.8 Inverse spin Hall angle of Si

The last but not the least parameter to derive is θ_{ISHE} . The spin pumping results show that the spin current flow to opposite direction for the different Co/Si samples. For the Co (t_{Co})/*undoped*-Si, the spin current flows into Co and induces a positive V_{ISHE} value via ISHE in the Co layer, as call sell-induced ISHE. The following Eq. 2.46 describes the charge current generated by ISHE:

$$I_c = \theta_{ISHE} w \left(\frac{2e}{h} \right) \lambda_s \tanh \left(\frac{t_N}{2\lambda_s} \right) j_s^0 \quad \text{Eq. 2.46}$$

the obtained value of I_c for all Co (10)/Si samples is listed in Table 4.5. It is worthy to note that the I_c of Co/*undoped*-Si is much smaller than other Co/Si samples, which shows that self-induced ISHE can be neglected in other Co/Si samples. The obtained, θ_{ISHE} of Co is 4.1×10^{-3} with $\lambda_s = 38$ nm and $j_s^0 = 0.47 \times 10^{-9} \frac{J}{m^2}$, which is close to the reported value (6.3×10^{-3}) measured by Hall effect.^{107,109}

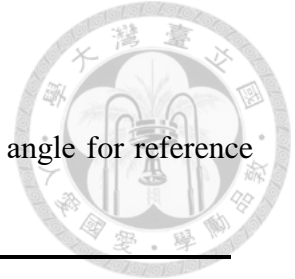


Table 4.5 The calculation result and parameter of inverse spin Hall angle for reference sample and sample A.

| Sample | Co/ <i>undoped-Si</i> | Co/ <i>n-Si-10</i> | Co/ <i>p-Si-10</i> | Co/ <i>p-Si-0.1</i> | Co/ <i>p-Si -0.005</i> |
|--|--------------------------|-----------------------|-----------------------|------------------------|---------------------------|
| α (10^{-3}) | 12.6±0.4 | 12.4±0.4 | 12.4±0.4 | 12.2±0.4 | 13.0±0.4 |
| $g_{eff}^{\uparrow\downarrow}$ (10^{19} m^{-2}) | 4.7±0.2 | 5.3±0.4 | 5.1±0.3 | 4.9±0.3 | 5.2±0.3 |
| D_N (cm^2/s) | - | 42±3 | 9.0±0.5 | 6.0±0.4 | 1.4±0.1 |
| τ_s (ps) | - | 180±9 | 160±8 | 92±5 | 12±1 |
| λ_s (nm) | 38 | 870±44 | 380±20 | 235±12 | 40±2 |
| V_{ISHE} (μV) | 2.15±0.1 | -13.4±0.7 | -8.68±0.4 | -19.4±0.9 | -5.74±0.3 |
| I_c (μA) | 0.04±0.02 | -0.2±0.01 | -0.12±0.01 | -0.37±0.02 | -0.16±0.01 |
| θ_{ISHE} (10^{-3}) | 4.1±0.2 | 0.23±0.01 | 0.32±0.02 | 1.50±0.07 | 4.2±0.2 |

For other Co (t_{Co})/Si samples, the spin current flows into Si and induce a negative V_{ISHE} value via ISHE in the Si layer. The θ_{ISHE} can be accurately extracted by fitting thickness-dependence data of I_c , shows in section 4.1.4. The thickness-dependence data of I_c and fitting result (red solid curves) are plotted in Fig. 4.31 for Co/*n*-Si-10, Co/*p*-Si-10, Co/*p*-Si-0.1 and Co/*p*-Si-0.005. The value of fitting parameter and fitting result are shown in Table 4.5. The θ_{ISHE} increase from 0.32×10^{-3} to 4.2×10^{-3} with increasing N from 2.8×10^{15} to $1.7 \times 10^{19} \text{ cm}^{-3}$ for *p*-type Si. The θ_{ISHE} is 0.23×10^{-3} for *n*-type Si with N of $8.1 \times 10^{14} \text{ cm}^{-3}$. Fig. 4.32 shows an inverse relation for λ_s and θ_{ISHE} . The fit yields $\lambda_s \theta_{ISHE} = 17.2 \text{ nm}$ (the red solid curve) for Si, which is close to that Co/Pt system⁸¹ ($\sim 19 \text{ nm}$) and slightly larger than Py/Pt system (12.8 nm , shown in inset of Fig. 4.32).^{78,110-114}

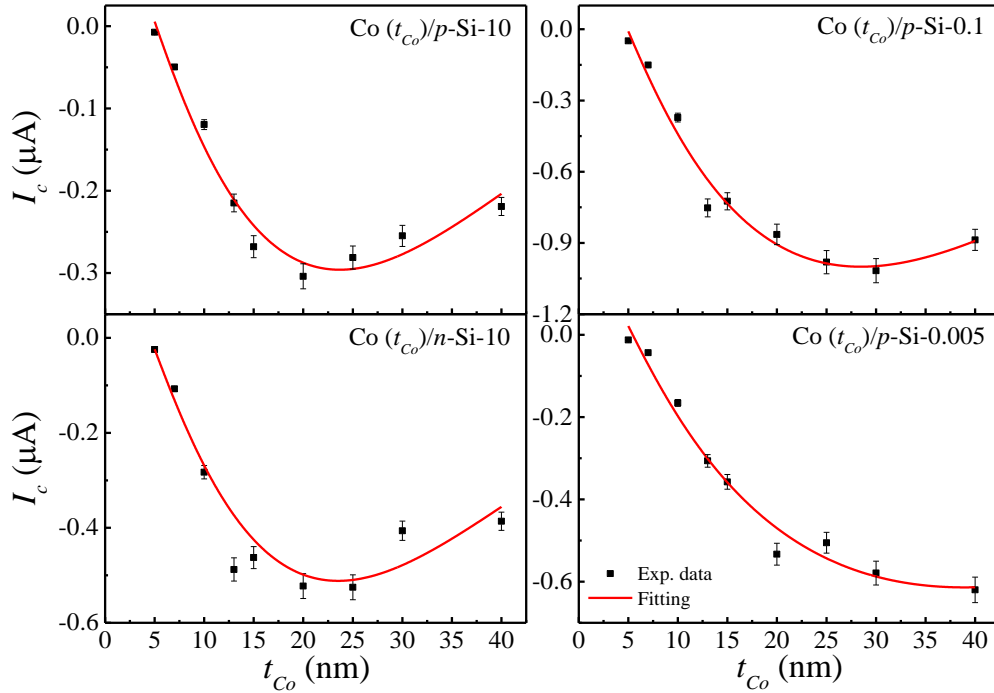


Fig. 4.31 The plot of $I_c - t_{Co}$ curves and fitting result (red solid curve) for Co (10)/*p*-Si(10), Co (10)/*n*-Si(10), Co (10)/*p*-Si(0.1) and Co (10)/*p*-Si(0.005).

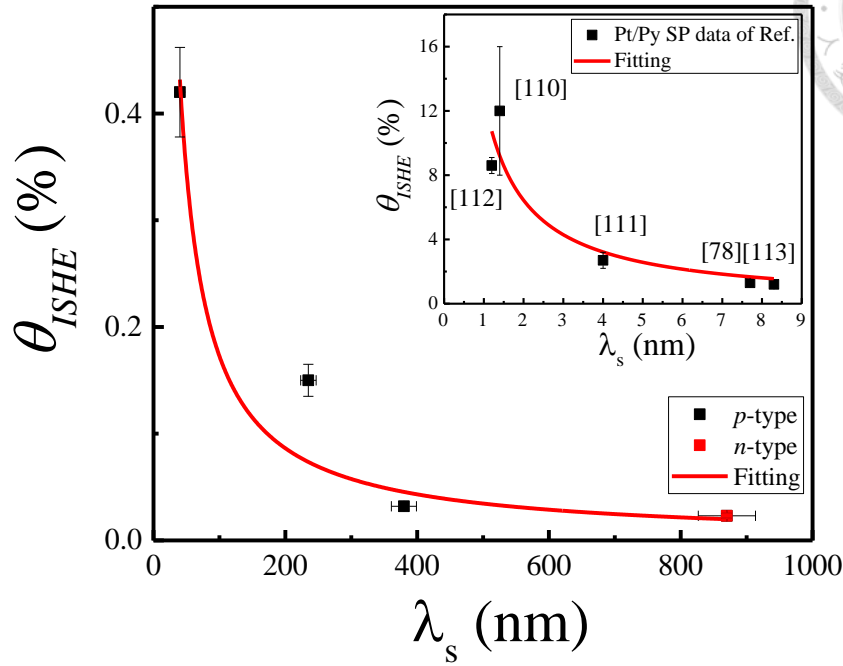
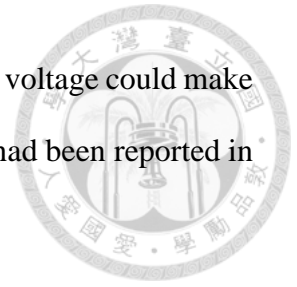


Fig. 4.32 The plot of θ_{ISHE} with λ_s and the red line shows $\lambda_s \times \theta_{ISHE} \cong 17.2$ nm. The inset shows that $\lambda_s \times \theta_{ISHE} \cong 12.8$ for Py/Pt system studied by the FMR-SP technique and the data obtained from literature.^{78,110-114}

We summarize the τ_s , λ_s and θ_{ISHE} for *p*-Ge, *p*-Si, *p*-GaAs, *n*-GaAs using the same method as shown in Table 4.6. The value of θ_{ISHE} of GaAs have been reported by two different groups. Saitoh's group,²⁹ obtained the θ_{ISHE} value of 30×10^{-3} for *p*-GaAs with $N = 1.4 \times 10^{19}$. Kwo's group⁴⁶ reported the θ_{ISHE} value to be 0.028×10^{-3} for the *p*-GaAs with $N = 1 \times 10^{18}$. The large variation could be due to the different doping concentrations, dopants, thickness and heating effect. Our resultant value of 4.2×10^{-3} is smaller than the value of GaAs with the same doping concentration and same analysis method, which is attributed to the larger SOI in GaAs. On the other hand, the θ_{ISHE} value of Si obtained from this work, 4.2×10^{-3} , is larger than the value of 0.1×10^{-3} obtained by Saitoh's group for the same doping concentration and dopant, which may be due to the

large heating effect occurring in their sample. The heating induced dc voltage could make the extraction of the ISHE voltage difficult. A similar heating effect had been reported in the GaAs system.⁴⁶



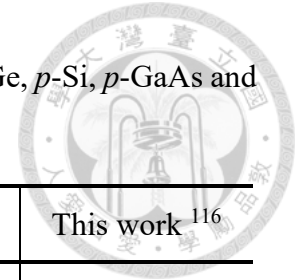


Table 4.6 The value of doping concentration, diffusion constant, spin-diffusion length, spin lifetime and spin Hall angle for *p*-Ge, *p*-Si, *p*-GaAs and *n*-GaAs.

| Group | M. Jamet ¹¹⁵ | Shiraishi ⁴⁵ | J. Kwo ⁴⁶ | E. Saitoh ^{29,113} | | | This work ¹¹⁶ |
|---|-------------------------|-------------------------|---------------------------|-----------------------------|-----------------------|---------------------|--------------------------|
| Material | CoFeB/ <i>p</i> -Ge | Py/ <i>p</i> -Ge | Py/ <i>p</i> -GaAs | Py/ <i>p</i> -GaAs | Py/ <i>n</i> -GaAs | Py/ <i>p</i> -Si | Co/ <i>p</i> -Si |
| N (cm ⁻³) | 9×10^{18} | 1×10^{18} | $1 \sim 2 \times 10^{18}$ | 1.4×10^{19} | 1.2×10^{18} | 2×10^{19} | 1.7×10^{19} |
| D_N (cm ² /s) | 4.67 | - | - | 2.83 | 113.75 | 3.23 | 1.4 |
| τ_s (ps) | 0.7 | - | - | 0.1 | 15 | 9 | 12 |
| λ_s (nm) | 26 | 20 | 163 | 5.3 | 411 | 56 | 40 |
| θ_{ISHE} ($\times 10^{-3}$) | 0.7 | 0.96 | 0.028 | 30 | -7 | 0.1 | 4.2 |



4.2 The dopant effect on spin-orbit interaction in GaAs

4.2.1 Hall effect measurement for GaAs

The mobility and diffusion constant are determined using Eq. 4.1 and Eq. 4.2, respectively.⁹⁸

$$\mu = \frac{R_H}{\rho} \quad \text{Eq. 4.1}$$

$$D_N = \frac{\mu kT}{e} \quad \text{Eq. 4.2} \quad \text{Einsitein's relation}$$

For GaAs system, the values of ρ and R_H are 0.07 Ω -cm and 15 cm^3/C , respectively, for p -GaAs with N of $3.9 \times 10^{17} \text{ cm}^{-3}$. The value of ρ and R_H are 0.001 Ω -cm and -1.4 cm^3/C , respectively, for n -GaAs with N of $4.3 \times 10^{18} \text{ cm}^{-3}$. On the other hand, the μ and D_N is 158 cm^2/Vs and 3.9 cm^2/s , respectively, for p -GaAs. The the μ and D_N are 1411 cm^2/Vs and 35 cm^2/s , respectively, for n -GaAs. Table 4.7 shows that the accurate electrical properties of GaAs and Si with different type of dopants.

Table 4.7 The parameter of carrier concentration (N), resistivity (ρ), thickness (t_{GaAs}), Hall coefficient (R_H), mobility (μ) and diffusion constant (D_N) for GaAs substrate.

| Substrate name | n -GaAs | p -GaAs |
|--------------------------------------|--------------------------------|--------------------------------|
| N (cm^{-3}) | $(4.3 \pm 0.1) \times 10^{18}$ | $(3.9 \pm 0.1) \times 10^{17}$ |
| ρ (ohm-cm) | 0.0010 ± 0.0005 | 0.07 ± 0.02 |
| t_{GaAs} (μm) | 350 ± 25 | 350 ± 25 |
| R_H (cm^3/C) | $(-1.4 \pm 0.02) \times 10^0$ | $(1.5 \pm 0.1) \times 10^1$ |
| μ (cm^2/Vs) | 1411 ± 200 | 158 ± 5 |
| D_N (cm^2/s) | 35 ± 5 | 3.9 ± 0.1 |

4.2.2 Magnetic properties of Co/GaAs

The magnetic properties of Co thin films for sample B are obtained by analyzing VSM data. Fig. 4.33 and Fig. 4.34 show the $M - H$ loops of Co (t_{Co})/ p -GaAs and Co (t_{Co})/ n -GaAs, respectively.

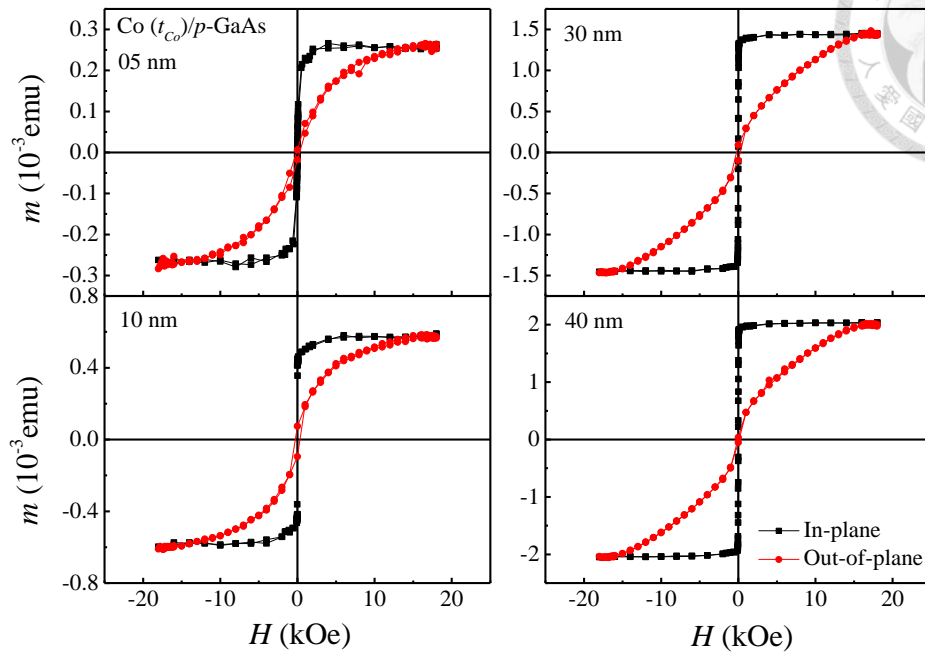


Fig. 4.33 The $M - H$ loops of $\text{Co}(t_{\text{Co}})/p\text{-GaAs}$ and the t_{Co} is 5 nm, 10 nm, 30 nm and 40 nm.

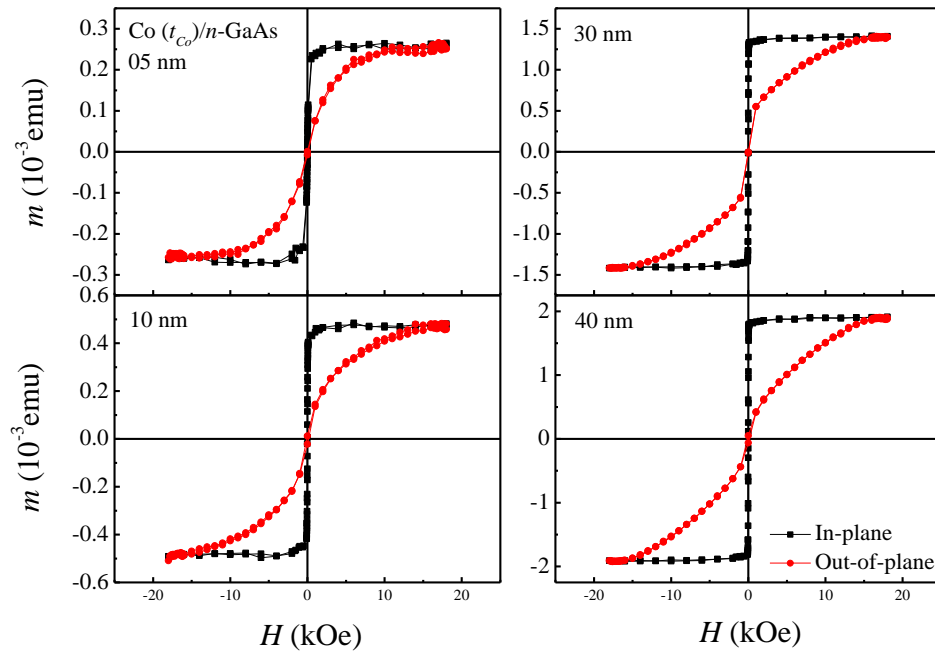


Fig. 4.34 The $M - H$ loops of $\text{Co}(t_{\text{Co}})/n\text{-GaAs}$ and the t_{Co} is 5 nm, 10 nm, 30 nm and 40 nm.

The black squares exhibit $M - H$ loop with in-plane field and the red circles exhibit $M - H$ loop with out-of-plane field. The $M - H$ loops show that the easy axis is in the films plane and the hard axis is along the out-of-plane direction. Fig. 4.35 show that the m_s is linear dependence on t_{Co} and the red solid line is the linear fitting result. The M_s is $1303 \pm 38 \text{ emu/cm}^3$ and the MDL is about 1 nm for Co thin films. Although the M_s of sample B is slightly larger than sample A, it is roughly the same within the uncertainty of data.

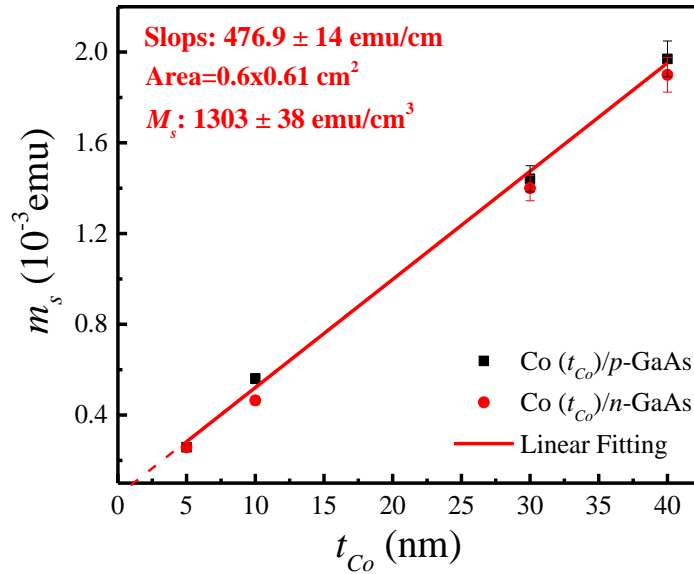


Fig. 4.35 The $m_s - t_{Co}$ curve for sample B and the red solid line is a linear fitting result.

$K_{eff} \times t_{Co}$ versus t_{Co} are plotted in the Fig. 4.36 (a) and (b) for Co/p-GaAs, Co/n-GaAs, respectively. The value of $K_{eff} \times t_{Co}$ is linear dependence on t_{Co} for sample B. The linear fitting result (red solid line) is shown in the Fig. 4.36 and it agrees with the Eq. 4.3. The K_v and K_s are extracted from intercept and slope of linear fit of $K_{eff} \times t_{FM} - t_{Co}$ curve, respectively. The values of K_v and K_s are listed in Table 4.8. The K_v of sample B is close to the value of sample A but the K_s of sample B is one half smaller

than the value of sample A. On the other hand, the value of $4\pi M_{eff}$ is obtained using Eq. 4.4 and the average value of $4\pi M_{eff}$ is 17k Oe for sample B.

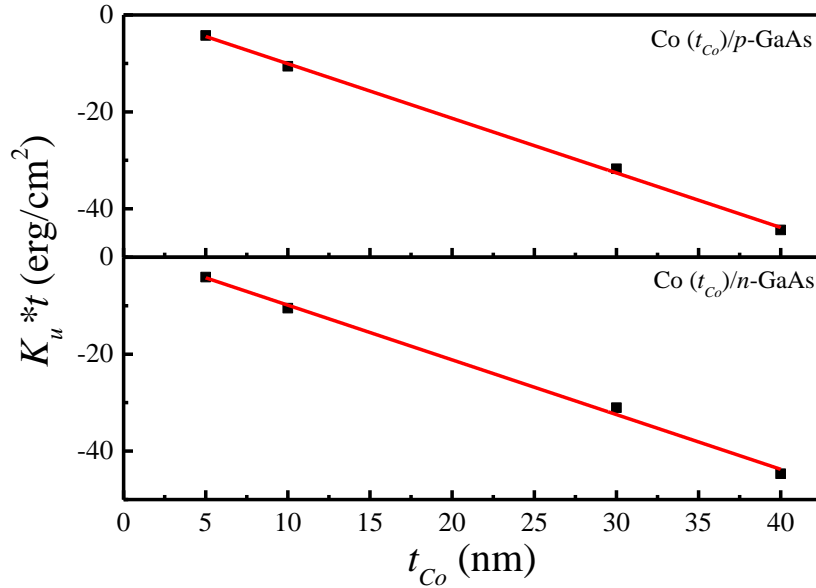


Fig. 4.36 The $K_{eff} \times t - t_{Co}$ curve for sample B and the red solid lines are linear fitting result.

Table 4.8 The value of M_s , K_v and K_s for Sample B, Co/n-Si-10 and Co/p-Si-10.

| Sample | Co/ <i>n</i> -GaAs | Co/ <i>p</i> -GaAs | Co/ <i>n</i> -Si-10 | Co/ <i>p</i> -Si-10 |
|----------------------------------|-----------------------|-----------------------|------------------------|------------------------|
| M_s (emu/cm ³) | 1303±38 | | 1264±20 | |
| K_v (Merg/cm ³) | -11.3±4.5 | -11.2±2.8 | -11.6±4.0 | -11.8±3.3 |
| K_s (erg/cm ²) | 0.7±0.3 | 0.6±0.3 | 1.30±0.17 | 1.34±0.14 |



4.2.3 Ferromagnetic resonance and effective damping constant of Co (t_{Co} nm)/GaAs.

The FMR spectra (black line) for Co (10)/*p*-GaAs and Co (10)/*n*-GaAs samples are shown in Fig. 4.37. The H_r and ΔH are extracted by fitting FMR spectrum using Eq. 4.5 and the fitting results (open circle) are shown in Fig. 4.37. The H_r and ΔH are 560 Oe and 90 Oe, respectively, for all Co (10)/GaAs samples.

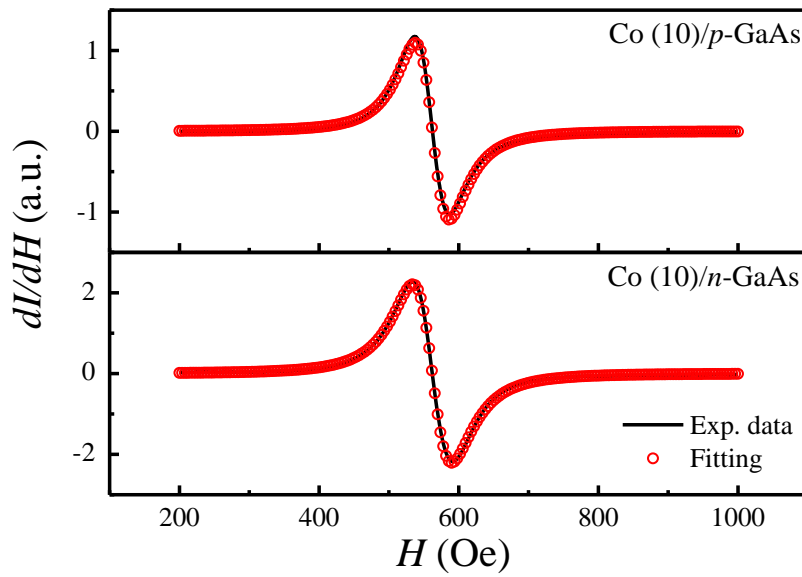


Fig. 4.37 The FMR spectra (dI/dH vs. H) for all Co (10)/GaAs samples. The open circle is fitting result using differential form of Lorentzian.

The H_r and ΔH versus t_{Co} are shown in the Fig. 4.38 (a) and (b), respectively, for sample B. The H_r has a minimum value of 558 Oe for all Co (13)/GaAs samples and ΔH has a minimum value of 75 Oe for all Co (20)/GaAs samples.

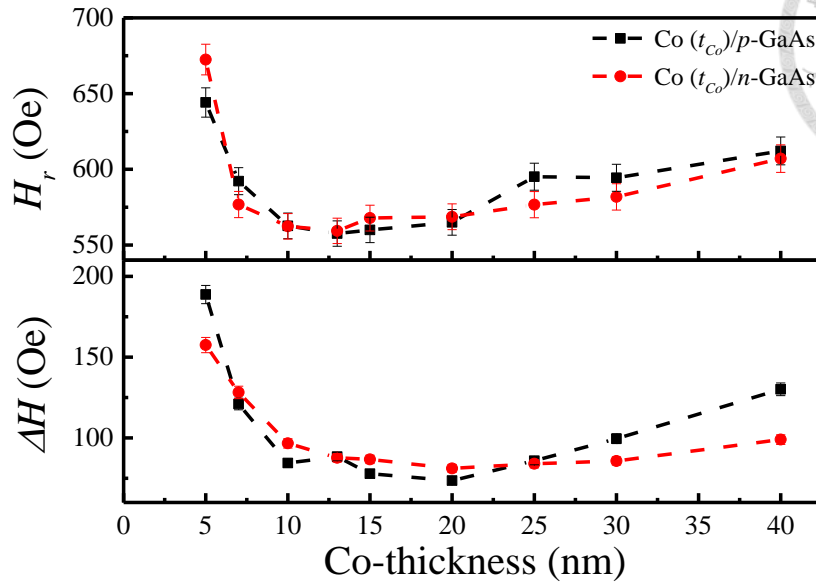


Fig. 4.38 The (a) H_r and (b) ΔH versus t_{Co} changing from 5 nm to 40 nm for sample B.

Fig. 4.39 (a) and (b) shown the data of $H_r(\theta_H)$ and $\Delta H(\theta_H)$, respectively, for Co (10)/p-GaAs and Co (10)/n-GaAs samples. The red solid curve in Fig. 4.39 (a) are the calculated results of $H_r(\theta_H)$ using Eq. 4.9 which match with experimental data. The θ_H dependence of the θ_M (calculated by combining Eq. 4.9 and Eq. 4.10 with $4\pi M_{eff}$) are plotted in Fig. 4.40 and the results show that the behavior of θ_M of sample B is similar to sample A.

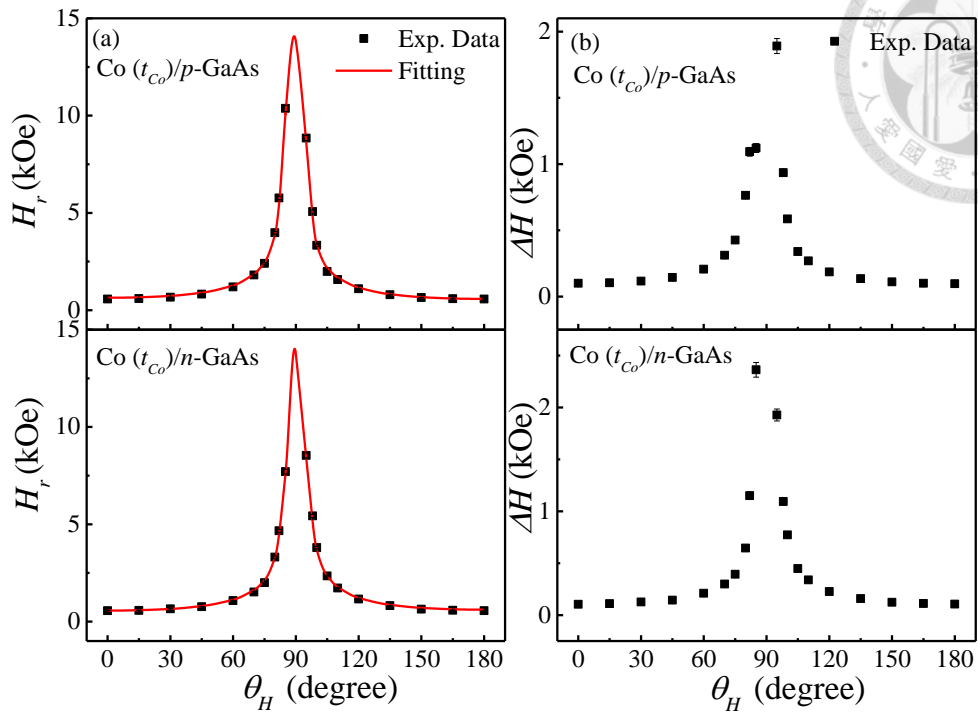


Fig. 4.39 The angular-dependence data of (a) H_r , calculational results of H_r (red line) and (b) ΔH for all Co (10)/GaAs samples.

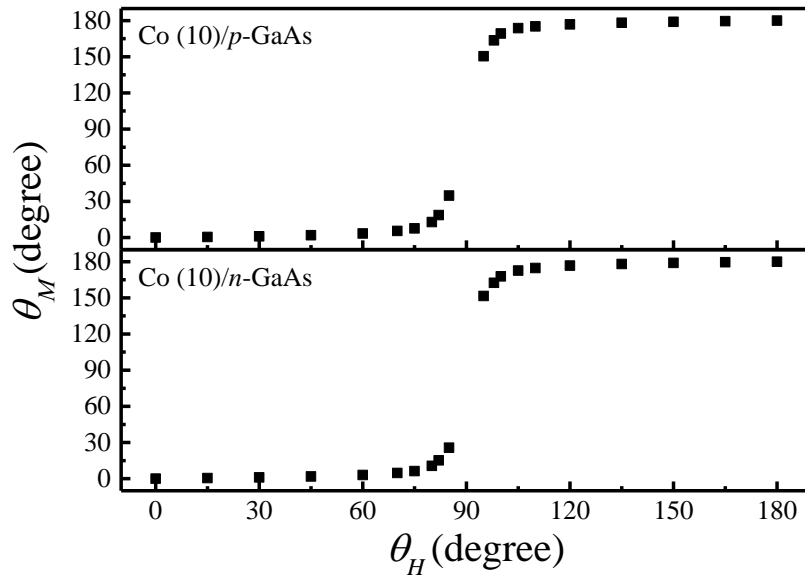


Fig. 4.40 The θ_M versus θ_H for all Co (10)/GaAs samples.

Using Eq. 4.11, the α can be experimentally determined by fitting the data of $H_r(\theta_H)$ and $\Delta H(\theta_H)$. Based on the calculation result, the α (black dot) as a function of t_{Co} and Fig. 4.41 shows the results of sample B. In Fig. 4.41, the red solid lines are fitting curves using Eq. 4.8; while the blue dash line and green dash-dot line describe $\alpha_0 + \alpha_{SP}$ and $\alpha_0 + \alpha_{EC}$, respectively. It is noted that the spin pumping term is dominant for thinner Co layers (< 25 nm); while the eddy-current damping term is dominant for thicker Co layer (> 25 nm). This phenomenon is similar to sample A.

The $g_{eff}^{\uparrow\downarrow}$ is derived from Eq. 4.8 by inserting the following essential parameters: γ is $1.77 \times 10^{19} \text{ C} \cdot \text{kg}^{-1}$, \hbar is $1.054 \times 10^{-34} \frac{\text{kg} \cdot \text{m}^2}{\text{s}^2} \text{S}$, M_s is 1303 emu/cm^3 . The obtained values of $g_{eff}^{\uparrow\downarrow}$ for sample B are shown in the fourth row of Table 4.9 The $g_{eff}^{\uparrow\downarrow}$ of sample B is $6.8 \times 10^{19} \text{ m}^{-2}$ and it is slightly larger than two samples A ($5.0 \times 10^{19} \text{ m}^{-2}$) and reference sample ($6.0 \times 10^{19} \text{ m}^{-2}$), shows in Fig. 4.42. From earlier report, the $g_{eff}^{\uparrow\downarrow}$ value is $3.7 \times 10^{18} \text{ m}^{-2}$ and $4.7 \times 10^{18} \text{ m}^{-2}$ for Py/*p*-GaAs and Py/*p*-Si, respectively; These results show that the spin injection efficiency of Co/SC is higher than the Py/SC, which is consistent with the literature report in FM/Pt system.⁴⁷

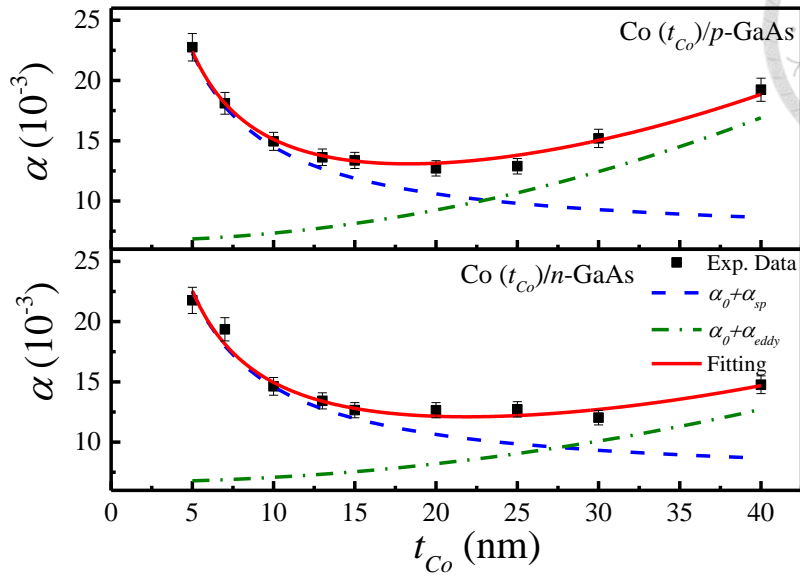


Fig. 4.41 The α versus t_{Co} curve for sample B. The red solid lines, blue and green dash-dot curves are described $\alpha_0 + \alpha_{SP} + \alpha_{EC}$, $\alpha_0 + \alpha_{SP}$ and $\alpha_0 + \alpha_{EC}$ fitting curves according to Eq. 4.8, respectively.

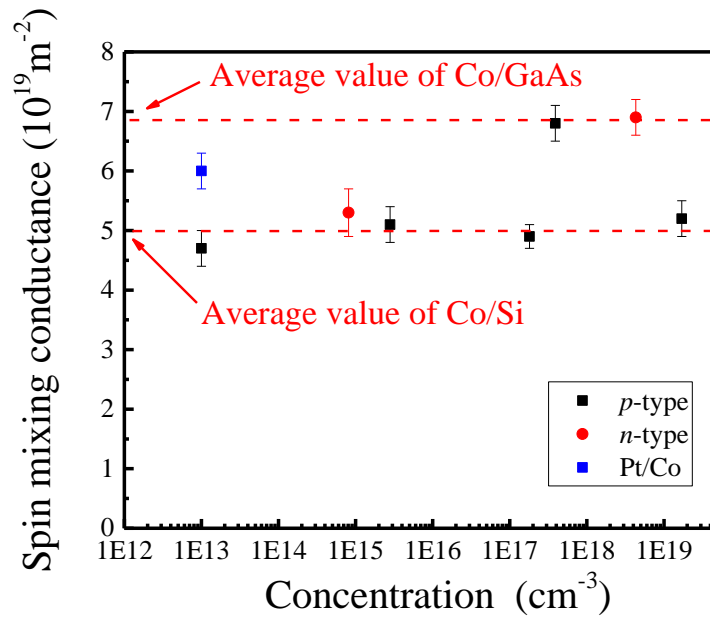


Fig. 4.42 The $g_{eff}^{\uparrow\downarrow}$ v.s. N for reference sample, sample A and sample B.



Table 4.9 The fitting results of damping constant and the value of effective spin mixing conductance for sample B, Co/*p*-Si-10 and Co/*n*-Si-10.

| Sample name | Co/ <i>n</i> -GaAs | Co/ <i>p</i> -GaAs | Co/ <i>n</i> -Si-10 | Co/ <i>p</i> -Si-10 |
|---|-----------------------|-----------------------|------------------------|------------------------|
| $\alpha_0 (10^{-3})$ | 6.7 ± 0.2 | | | |
| C_{SP} (10^{11}) | 7.9 ± 0.3 | 7.8 ± 0.2 | 6.3 ± 0.4 | 6.0 ± 0.3 |
| C_{CE} (10^{12}) | 3.7 ± 0.4 | 6.4 ± 0.2 | 2.2 ± 0.5 | 2.3 ± 0.3 |
| $g_{eff}^{\uparrow\downarrow}$ (10^{19}m^{-2}) | 6.9 ± 0.3 | 6.8 ± 0.3 | 5.3 ± 0.4 | 5.1 ± 0.3 |

4.2.4 Inverse spin Hall effect, spin lifetime, spin diffusion length and

inverse spin Hall angle of GaAs

In this section, we will discuss the τ_s , λ_s and θ_{ISHE} in the GaAs. The FMR spectra and voltage signals are displayed in the Fig. 4.43 (a) ~ (b) and Fig. 4.44 (a) ~ (b), respectively, for Co (10)/*p*-GaAs and Co (10)/*n*-GaAs samples.

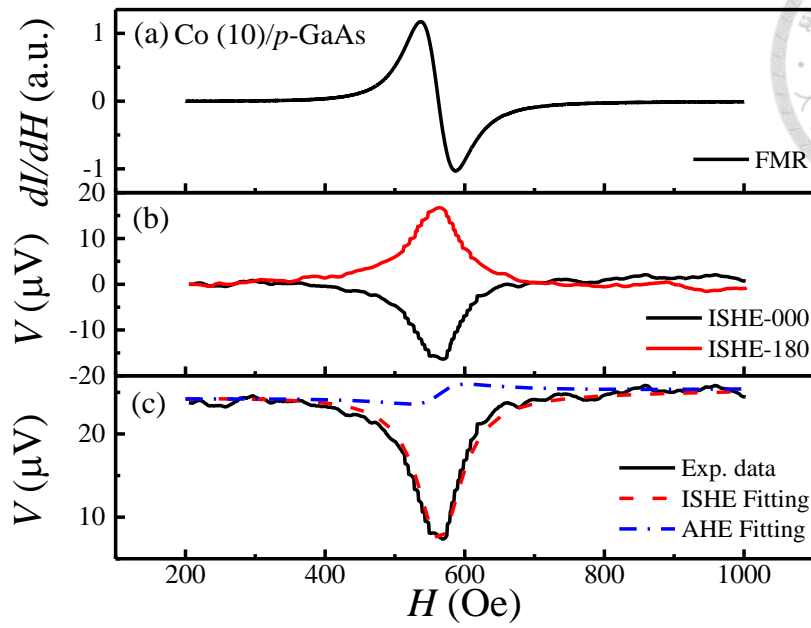


Fig. 4.43(a) The FMR spectrum for Co (10)/*p*-GaAs sample (b) voltage signals for Co (10)/*p*-GaAs sample (c) The black, red dash and blue dash-dot curves are experiment data, ISHE and AHE fitting curves using Eq. 4.6.

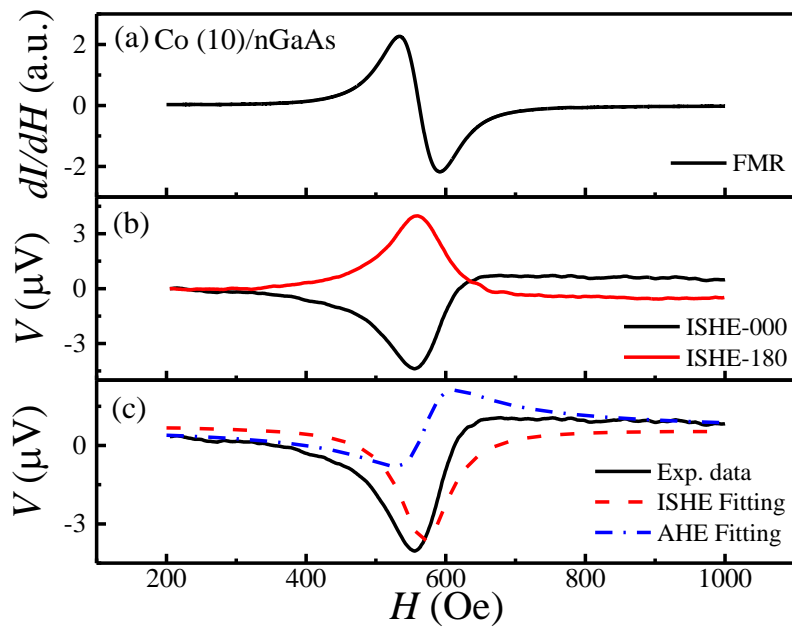


Fig. 4.44 (a) The FMR spectrum for Co (10)/*n*-GaAs sample (b) voltage signals for Co (10)/*n*-GaAs sample (c) The black, red dash and blue dash-dot curves are experiment data, ISHE and AHE fitting curves using Eq. 4.6.

The $V(\theta_H)$ shows the reverse signal when the θ_H direction changes from 0° to 180° . Fig. 4.43 (c) and Fig. 4.44 (c) show the fitting results of V using Eq. 4.6 for Co (10)/ p -GaAs and Co (10)/ n -GaAs samples, respectively. The black, red dash and blue dash-dot curves are experiment data, symmetric and asymmetric fitting curves, respectively. From fitting results, a negative V_{ISHE} value of -17.6 and -4.3 μV is obtained at 100 mW for Co (10)/ p -GaAs and Co (10)/ n -GaAs samples, respectively. Fig. 4.45 shows that the values of V_{ISHE} increases linearly with increasing P_{MW} from 20 to 100 mW for Co (10)/ p -GaAs and Co (10)/ n -GaAs samples. These results show that the direction of spin current is into the GaAs substrate. Fig. 4.46 (a) and (b) shown the thickness-dependence V_{ISHE} and I_{ISHE} ($\equiv \frac{V_{ISHE}}{R}$), respectively. The V_{ISHE} has maximum value at 20 nm for sample B. However, the I_{ISHE} has maximum value at 30 nm and 25 nm for Co/ p -GaAs and Co/ n -GaAs, respectively.

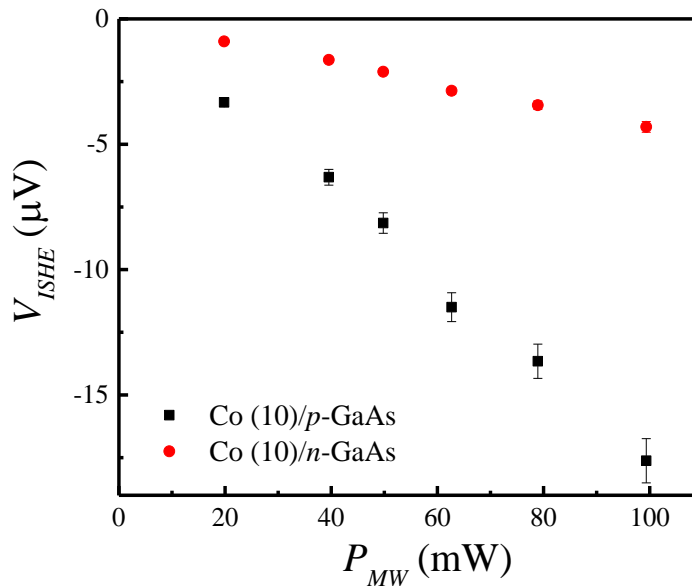


Fig. 4.45 The plot of V_{ISHE} with microwave power which is varied from 20 to 100 mW for all Co (10)/GaAs samples.

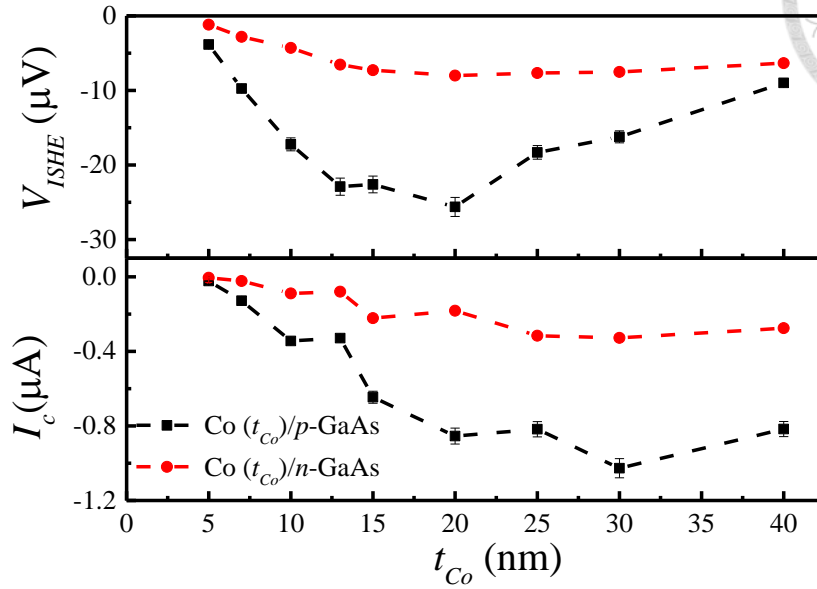


Fig. 4.46 (a) and (b) The thickness-dependence data of V_{ISHE} and I_c , respectively for sample B.

The τ_s in GaAs can be extracted by fitting the normalized $V_{ISHE}(\theta)$ using equation Eq. 2.50 and Eq. 2.51

$$V_{ISHE}(\theta_H) = A \times j_s^0 \times \left[\cos \theta_H \cos(\theta_H - \theta_M) \int_0^{t_{sc}} e^{-x/\sqrt{D_N \tau_s}} dx + \sin \theta_H \sin(\theta_H - \theta_M) \int_0^{t_{sc}} e^{-x/\sqrt{\frac{D_N \tau_s}{1 + i\omega_L \tau_s}}} dx \right]$$

Eq. 2.51

The normalized value of $V_{ISHE}(\theta)$ [$V_{ISHE}(\theta_H)/V_{ISHE}(0)$] are shown Fig. 4.47 (a) and (b) for Co (10)/ p -GaAs and Co (10)/ n -GaAs, respectively. In Fig. 4.47, the red solid curves are the fitting result of normalized $V_{ISHE}(\theta)$ by inserting the following essential parameters: the f is 9.8 GHz, γ is $1.77 \text{ rads}^{-1}\text{T}^{-1}$, h_{rf} is $1.4 \times \sqrt{P_{MW}}$ G, P_{MW} is 50 mW, t_{sc} is $350 \mu\text{m}$, M_s is 1303 Oe, the θ_M are obtained in section 4.2.2 and the other parameter (α , $g_{eff}^{\uparrow\downarrow}$ and D_N) are listed in Table 4.10. The fitting results show that the τ_s

and λ_s is 100 ps and 197 nm, respectively, for p -GaAs. Moreover, the τ_s and λ_s is 90 ps and 561 nm, respectively, for n -GaAs.

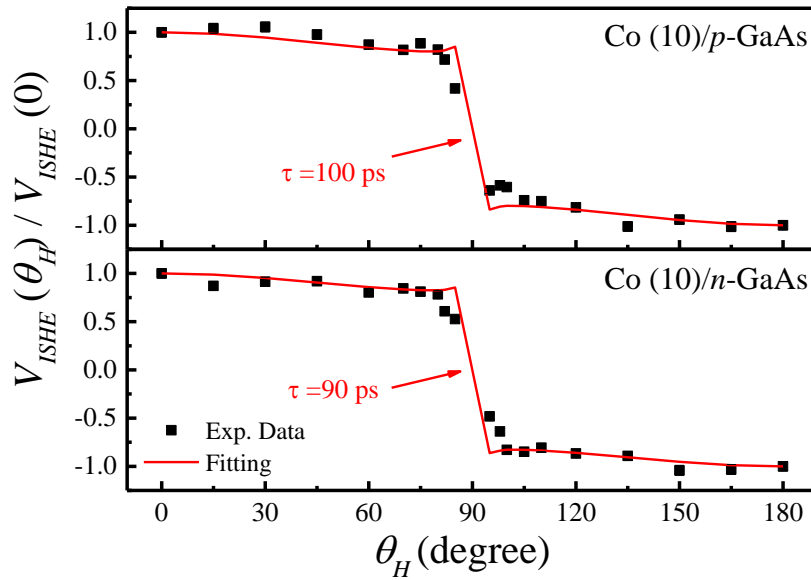


Fig. 4.47 The normalized value of $V_{ISHE}(\theta_H)$ [$V_{ISHE}(\theta_H)/V_{ISHE}(0)$] versus θ_H and the rea solid curves is fitting result for all Co (10)/GaAs samples.

The θ_{ISHE} can be accurately extracted by fitting thickness-dependence data of I_c , see in section 4.1.4. Fig 4.48 shows that the thickness-dependence data of I_c and fitting results (red solid curve) for sample B. From the fitting results, the θ_{ISHE} is 0.96×10^{-3} and 0.10×10^{-3} for p -GaAs and n -GaAs, respectively. The value of fitting parameter and the fitting result are shown in Table 4.10. From our results, the θ_{ISHE} of p -Si-10 (0.32×10^{-3}) is slightly larger than n -Si-10 (0.23×10^{-3}) and θ_{ISHE} of p -GaAs (0.96×10^{-3}) is one order larger than n -GaAs (0.10×10^{-3}); but its sign is independent on the carrier type.¹¹⁷

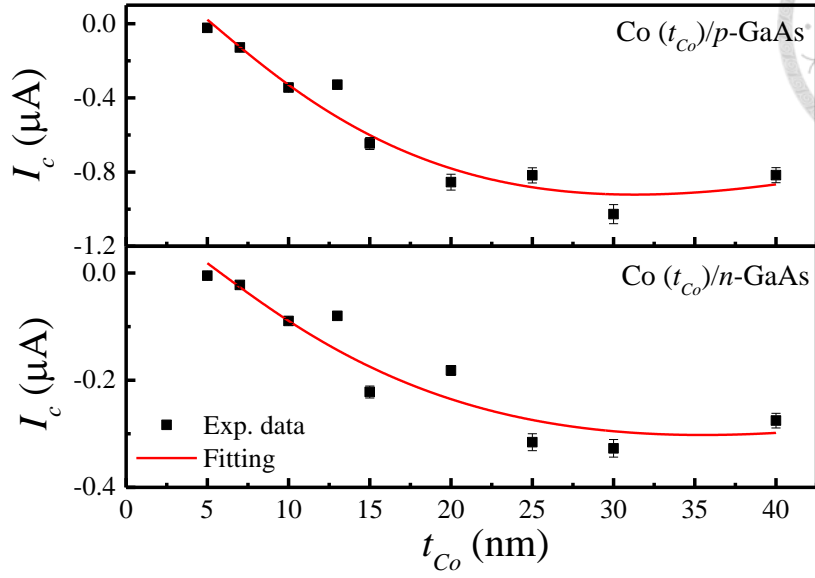
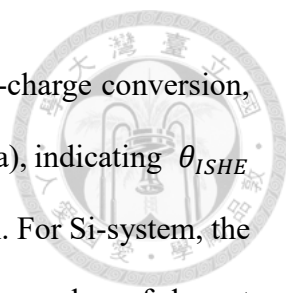


Fig. 4.48 The plot of $I_c - t_{Co}$ curves for sample B and the red solid curves are the fitting result.

To examine the universality of our results, we summarize the reported experimental values of θ_{ISHE} for various SCs as listed in Table 4.11. Since the SOI of SC depends on both the doping concentration and the atomic number of dopant (Z),^{53,116} we only compare the samples with similar doping concentration and dopant. For GaAs of $N \sim 10^{18}$, our experimental value of 0.10×10^{-3} is comparable to the value of 0.19×10^{-3} obtained by Kwo's group⁴⁶, but is one order smaller than the value of 7×10^{-3} obtained by Saitoh's group.³⁰ The SCs with different type of carriers have the same sign of θ_{ISHE} except for the result of Saitoh's group. Although the result of same sign of θ_{ISHE} is against the general expectation of an opposite sign due to the opposite charge property of electron and hole, it can be explained with the competition between the intrinsic and extrinsic SOI mechanism.¹² As to the large discrepancy between our data and Saito's, it may be related to the large uncertainty in Saito's data due to the weak voltage signal.²⁹ The magnitude of V_{ISHE} obtained in this work is three order higher than that from Saito's group.



To investigate the influence of dopant on the SOI induced spin-charge conversion, the data of θ_{ISHE} vs. Z for different SCs are shown in the Fig 4.49 (a), indicating θ_{ISHE} increases with increasing Z for Ge- and GaAs- but not for Si-system. For Si-system, the influence of Z is much less, which is attributed to the low atomic number of dopant compared with GaAs and Ge. As mentioned in the theoretical background, the magnitude of SHE is determined by the combination of intrinsic and extrinsic scatterings.¹¹⁷ The intrinsic one depends on the band structure, and the extrinsic mechanisms include the skew-scattering and the side-jump scattering. For GaAs, the skew-scattering is the domination mechanism due to its relatively high mobility,⁵⁹ thus the magnitude of θ_{ISHE} should scale with the SOI of dopant atom. In principle, the strength of SOI is a power law of Z ; but how fast SOI increasing with Z depends on the band character of outer electrons of atom.^{65,115,118} Since the dopants in the listed GaAs samples are Be, Si and Zn with the outer electronic band of s, d and p respectively, the Z dependence of SOI cannot not be simulated with a specific atoms. An empirical trend of Z^2 was proposed as an overall systematic variation of SOI without considering the change from one element to element.¹¹⁸ By combining the data of Ref. 46 (solid circles) and this work (solid squares), Fig 4.49 (b) plots the data of θ_{ISHE} vs. Z for GaAs. The solid curve is the fitting result using the relation of Z^2 proposed by Landau and Lifshitz, confirming the important role of outmost electron of dopant on the spin-charge conversion in GaAs.¹¹⁸

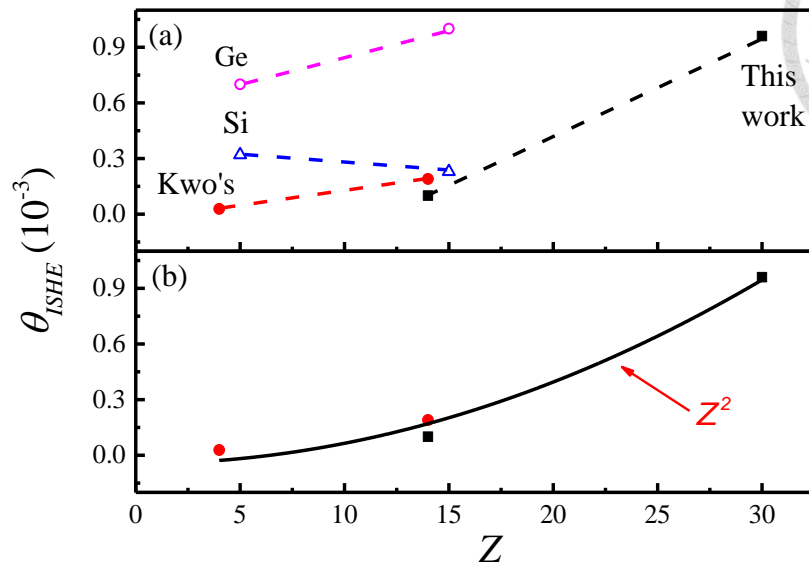


Fig. 4.49 (a) Plot of the θ_{ISHE} vs. Z for various SCs listed in Table 4.11 and (b) for GaAs system with the black line being the fit of Z^2 .

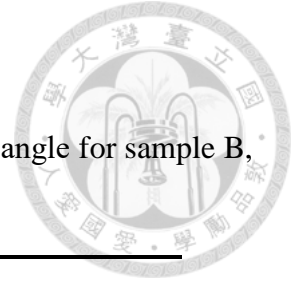


Table 4.10 The calculation result and parameter of inverse spin Hall angle for sample B, Co/*p*-Si-10, and Co/*n*-Si-10.

| Sample name | Co/ <i>n</i> -GaAs | Co/ <i>p</i> -GaAs | Co/ <i>n</i> -Si-10 | Co/ <i>p</i> -Si-10 |
|--|-----------------------|-----------------------|------------------------|------------------------|
| $g_{eff}^{\uparrow\downarrow}$ (10^{19} m^{-2}) | 6.9±0.3 | 6.8±0.3 | 5.3±0.4 | 5.1±0.3 |
| D_N (cm^2/s) | 35±5 | 3.9±0.1 | 42±3 | 9.0±0.5 |
| τ_s (ps) | 90±5 | 100±5 | 180±9 | 160±8 |
| λ_s (nm) | 561±28 | 197±10 | 870±44 | 380±20 |
| θ_{ISHE} (10^{-3}) | 0.10±0.01 | 0.96±0.05 | 0.23±0.01 | 0.32±0.02 |



Table 4.11 The experimentally results of the team that simultaneously studied the θ_{ISHE} and λ_s of *n*- and *p*-type SC.

| Group | M. Jamet ^{115,119,120} | | J. Kwo ⁴⁶ | | E. Saitoh ²⁹ | | J.G. Lin ¹¹⁶ | | This work | |
|--|--|--------------------|---|----------------|---|----------------------|---|----------------------|---|----------------------|
| Exp. method | λ_s : Hanle effect. θ_{ISHE} : Spin pumping | | λ_s : Theoretical value. θ_{ISHE} : Spin pumping | | λ_s and θ_{ISHE} : Spin pumping | | λ_s and θ_{ISHE} : Spin pumping | | λ_s and θ_{ISHE} : Spin pumping | |
| Material | <i>n</i> -Ge | <i>p</i> -Ge | <i>n</i> -GaAs | <i>p</i> -GaAs | <i>n</i> -GaAs | <i>p</i> -GaAs | <i>n</i> -Si-10 | <i>p</i> -Si-10 | <i>n</i> -GaAs | <i>p</i> -GaAs |
| Dopant (Z) | P (15) | B (5) | Si (14) | Be (4) | Si (14) | Zn (30) | P (15) | B (5) | Si (14) | Zn (30) |
| N (cm⁻³) | $\sim 10^{19}$ | 9×10^{18} | $1 \sim 2 \times 10^{18}$ | | 1.4×10^{19} | 1.2×10^{18} | 1.4×10^{19} | 8.1×10^{14} | 2.8×10^{15} | 4.3×10^{18} |
| τ_s (ps) | 400 | 0.7 | - | - | 15 | 0.1 | 180 | 160 | 90 | 100 |
| λ_s (nm) | 1300 | 26 | 94 (4.2K) | 163 | 411 | 5.3 | 870 | 380 | 561 | 197 |
| θ_{ISHE} (10⁻³) | 1~2 | 0.7 | 0.19 | 0.028 | -7 | 30 | 0.23 | 0.32 | 0.1 | 0.96 |



Chapter 5 Conclusion

A series of uniform quality Co thin films are deposited on the Si and GaAs single crystals by magnetron sputtering system. These samples are used to study the behavior of spintronic transport and dopant effect on spin-orbit interaction in the Si and GaAs single crystals, by the FMR-SP and ISHE-probe technique. The pure spin current is successfully injected into the Si and GaAs single crystals by FMR and spin signal can be measured using ISHE.

The *p*-type Si single crystals with N ranging from 8.1×10^{14} to $1.7 \times 10^{19} \text{ cm}^{-3}$ are used. Various critical parameters, such, τ_s , λ_s and θ_{ISHE} are obtained. For *p*-type Si, the λ_s decreases from 380 nm to 40 nm and the θ_{ISHE} increases from 0.32×10^{-3} to 4.2×10^{-3} , respectively, upon increasing N from 2.8×10^{15} to $1.7 \times 10^{19} \text{ cm}^{-3}$. For *n*-type Si with $N = 8.1 \times 10^{14} \text{ cm}^{-3}$, the τ_s and θ_{ISHE} are 870 nm and 0.23×10^{-3} , respectively. The experimental results show that these parameters can be tuned by the doping concentration and the dopant atoms in the Si. A constant value of $\lambda_s \theta_{ISHE}$ (17.2 nm) for Si is found to be slightly larger than Py (12.8 nm), indicating that Si is as effective as Pt in terms of converting the spin current for the application of spintronic devices.

On the other hand, the λ_s and θ_{ISHE} are 197 nm and 0.96×10^{-3} , respectively, for *p*-GaAs with $N = 3.9 \times 10^{17} \text{ cm}^{-3}$. The λ_s and θ_{ISHE} is 561 nm and 0.1×10^{-3} , respectively, for *n*-GaAs with N of $4.3 \times 10^{18} \text{ cm}^{-3}$. The θ_{ISHE} is found to have the same sign for *n*-type and *p*-type GaAs, but its magnitude is one order larger in *p*-type than *n*-type, which is attributed to the higher atomic number of dopant in *p*-type GaAs. Furthermore, the relation of θ_{ISHE} vs Z is found to follow the Landau-Lifshitz Z^2 scaling, in consistent with the model considering only the outmost electron for non-specific atoms. This study provides a deeper understanding for the influence of dopant atom on the spin-charge

conversion rate of SC, which benefits the future applications of energy-saving spintronic devices.

According to overall results, the magnitude of θ_{ISHE} is sensitive to the doping concentration and atomic number of dopant, but the sign of θ_{ISHE} is independent on the carrier type. This work demonstrates an effective route to tune the efficiency of spin-charge conversion by changing the doping concentration and dopant atoms in the SC system. The implication of these results indicates that the ISHE of SC is dominated by the extrinsic scattering mechanism instead of the intrinsic mechanism and the SOI of dopant atoms play an important role in the ISHE of SC. Owing to the energy saving resulted from the zero-dispersion of spin current, this study benefits the development and design of spintronic devices, such as new type of field emission spin-based MOSFET.



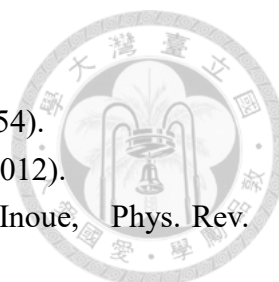
References

- ¹ N. F. Mott, Proc. Phys. Soc. **47**, 571 (1935).
- ² Bernard Dieny, Ronald B., Goldfarb, and Kyung-Jin Lee, *Introduction to magnetic random-access memory / edited by Bernard Dieny, Ronald B. Goldfarb, Kyung-Jin Lee*. (Wiley-IEEE Press, Hoboken, New Jersey, 2017).
- ³ Igor Žutić, Jaroslav Fabian, and S. Das Sarma, Reviews of Modern Physics **76** (2), 323 (2004).
- ⁴ P. A. M. Dirac, Proceedings of the Royal Society of London. Series A, Containing Papers of a Mathematical and Physical Character **117** (778), 610 (1928).
- ⁵ P. A. M. Dirac, Proceedings of the Royal Society of London. Series A, Containing Papers of a Mathematical and Physical Character **118** (779), 351 (1928).
- ⁶ Sadamichi Maekawa, *Spin Current / edited by Sadamichi Maekawa*. (Oxford University Press, Oxford, 2012).
- ⁷ Kim Jongyeon, Ayan Paul, Paul A. Crowell, Steven J. Koester, Sachin S. Sapatnekar, Wang Jian-Ping, and Chris H. Kim, Proc. IEEE **103** (1), 106 (2015).
- ⁸ Atsufumi Hirohata, Keisuke Yamada, Yoshinobu Nakatani, Ioan-Lucian Prejbeanu, Bernard Diény, Philipp Pirro, and Burkard Hillebrands, J. Magn. Magn. Mater. **509** (2020).
- ⁹ S. D. Bader and S. S. P. Parkin, Annual Review of Condensed Matter Physics **1** (1), 71 (2010).
- ¹⁰ Sabpreet Bhatti, Rachid Sbiaa, Atsufumi Hirohata, Hideo Ohno, Shunsuke Fukami, and S. N. Piramanayagam, Mater. Today **20** (9), 530 (2017).
- ¹¹ Yuan Ping Feng, Lei Shen, Ming Yang, Aizhu Wang, Minggang Zeng, Qingyun Wu, Sandhya ch, and Ching-Ray Chang, Wiley Interdisciplinary Reviews: Computational Molecular Science, e1313 (2017).
- ¹² M. Julliere, PhLA **54** (3), 225 (1975).
- ¹³ M. N. Baibich, J. M. Broto, A. Fert, F. Nguyen Van Dau, F. Petroff, P. Etienne, G. Creuzet, A. Friederich, and J. Chazelas, Phys. Rev. Lett. **61** (21), 2472 (1988).
- ¹⁴ B. Dieny, V.S. Speriosu, B.A. Gurney, S.S.P. Parkin, D.R. Wilhoit, K.P. Roche, S. Metin, D.T. Peterson, and S. Nadimi, J. Magn. Magn. Mater. **93**, 101 (1991).
- ¹⁵ J. S. Moodera, L. R. Kinder, T. M. Wong, and R. Meservey, Phys. Rev. Lett. **74** (16), 3273 (1995).
- ¹⁶ J. Mathon and A. Umerski, Phys. Rev. B **63** (22) (2001).
- ¹⁷ W. H. Butler, X. G. Zhang, T. C. Schulthess, and J. M. MacLaren, Phys. Rev. B

63 (5) (2001).

- 18 S. Yuasa and D. D. Djayaprawira, J. Phys. D: Appl. Phys. **40** (21), R337 (2007).
19 M. Bowen, V. Cros, F. Petroff, A. Fert, C. Martínez Boubeta, J. L. Costa-Krämer,
J. V. Anguita, A. Cebollada, F. Briones, J. M. de Teresa, L. Morellón, M. R. Ibarra,
F. Güell, F. Peiró, and A. Cornet, Appl. Phys. Lett. **79** (11), 1655 (2001).
20 S. S. Parkin, C. Kaiser, A. Panchula, P. M. Rice, B. Hughes, M. Samant, and S. H.
Yang, Nat. Mater. **3** (12), 862 (2004).
21 S. Yuasa, T. Nagahama, A. Fukushima, Y. Suzuki, and K. Ando, Nat. Mater. **3**
(12), 868 (2004).
22 S. Ikeda, J. Hayakawa, Y. Ashizawa, Y. M. Lee, K. Miura, H. Hasegawa, M.
Tsunoda, F. Matsukura, and H. Ohno, Appl. Phys. Lett. **93** (8) (2008).
23 Evgeny Y., Tsymbal, and Igor Žutić, *Handbook of spin transport and magnetism*
edited by Evgeny Y. Tsymbal, Igor Žutić. (CRC Press, Boca Raton, FL, 2012).
24 M. I. Dyakonov and V. I. Perel, PhLA **35** (6), 459 (1971).
25 Y. K. Kato, R. C. Myers, A. C. Gossard, and D. D. Awschalom, Science **306**
(5703), 1910 (2004).
26 S. O. Valenzuela and M. Tinkham, Nature **442** (7099), 176 (2006).
27 E. Saitoh, M. Ueda, H. Miyajima, and G. Tatara, Appl. Phys. Lett. **88** (18),
182509 (2006).
28 L. Liu, T. Moriyama, D. C. Ralph, and R. A. Buhrman, Phys. Rev. Lett. **106** (3),
036601 (2011).
29 K. Ando, S. Takahashi, J. Ieda, H. Kurebayashi, T. Trypiniotis, C. H. Barnes, S.
Maekawa, and E. Saitoh, Nat Mater **10** (9), 655 (2011).
30 K. Ando and E. Saitoh, Nature Communications **3**, 629 (2012).
31 Marta Galbiati, *Molecular spintronics : from organic semiconductors to self-*
assembled monolayers / by Marta Galbiati. (Springer International Publishing,
Cham, 2016).
32 Brajesh Kumar Kaushik, *Next generation spin torque memories / by Brajesh*
Kumar Kaushik, Shivam Verma, Anant Aravind Kulkarni, Sanjay Prajapati.
(Springer Singapore, Singapore, 2017).
33 Swaroop Ghosh, *Sensing of Non-Volatile Memory Demystified edited by Swaroop*
Ghosh, 1st ed. 2019. ed. (Springer International Publishing, Cham, 2019).
34 Wang Zhi Gang and Y. Nakamura, IEEE Transactions on Magnetism **32** (5), 4022
(1996).
35 Tetsufumi Tanamoto, Hideyuki Sugiyama, Tomoaki Inokuchi, Takao Marukame,
Mizue Ishikawa, Kazutaka Ikegami, and Yoshiaki Saito, J. Appl. Phys. **109** (7)
(2011).
36 Satoshi Sugahara and Junsaku Nitta, Proc. IEEE **98** (12), 2124 (2010).

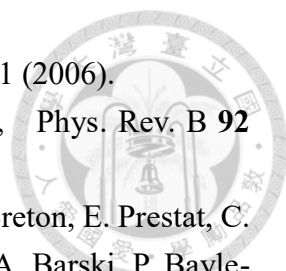
- 37 Satoshi Sugahara and Masaaki Tanaka, *Appl. Phys. Lett.* **84** (13), 2307 (2004).
- 38 Satoshi Sugahara and Masaaki Tanaka, *J. Appl. Phys.* **97** (10) (2005).
- 39 Jaroslav Fabian, Alex Matos-Abiague, Christian Ertler, Peter Stano, and Igor Žutić, *Acta Physica Slovaca. Reviews and Tutorials* **57** (4-5) (2007).
- 40 Y. Saito, T. Inokuchi, M. Ishikawa, H. Sugiyama, T. Marukame, and T. Tanamoto, *JEIS* **158** (10), H1068 (2011).
- 41 E. Shikoh, K. Ando, K. Kubo, E. Saitoh, T. Shinjo, and M. Shiraishi, *Phys. Rev. Lett.* **110** (12), 127201 (2013).
- 42 S. De Cesari, A. Balocchi, E. Vitiello, P. Jahandar, E. Grilli, T. Amand, X. Marie, M. Myronov, and F. Pezzoli, *Phys. Rev. B* **99** (3) (2019).
- 43 R. Jansen, S. P. Dash, S. Sharma, and B. C. Min, *Semicond Sci Tech* **27** (8), 083001 (2012).
- 44 R. Jansen, *Nat. Mater.* **11** (5), 400 (2012).
- 45 M. Koike, E. Shikoh, Y. Ando, T. Shinjo, S. Yamada, K. Hamaya, and M. Shiraishi, *Applied Physics Express* **6** (2), 023001 (2013).
- 46 H. Y. Hung, T. H. Chiang, B. Z. Syu, Y. T. Fanchiang, J. G. Lin, S. F. Lee, M. Hong, and J. Kwo, *Appl. Phys. Lett.* **105** (15), 152413 (2014).
- 47 Weifeng Zhang, Wei Han, Xin Jiang, See-Hun Yang, and Stuart S. P. Parkin, *Nature Physics* **11** (6), 496 (2015).
- 48 Willardson, Robert K. Beer, and Albert C., *Semiconductors and semimetals.* **82**, 1 (2008).
- 49 E. Saitoh, *Topological spin current.* (Oxford University Press, 2012).
- 50 Jairo Sinova and A.H. MacDonald, *Semiconductors and semimetals.* **82**, 45 (2008).
- 51 Michel I. Dyakonov, *Spin Physics in Semiconductors* (Springer Berlin Heidelberg, Berlin, Heidelberg, 2008).
- 52 A. R. Hamilton, R. Danneau, O. Klochan, W. R. Clarke, A. P. Micolich, L. H. Ho, M. Y. Simmons, D. A. Ritchie, M. Pepper, K. Muraki, and Y. Hirayama, *J. Phys.: Condens. Matter* **20** (16) (2008).
- 53 Y. Song, O. Chalaev, and H. Dery, *Phys. Rev. Lett.* **113** (16), 167201 (2014).
- 54 Yang Song and Hanan Dery, *Phys. Rev. B* **86** (8) (2012).
- 55 M. I. Dyakonov and V. I. Perel, *Sov. Phys. JETP Lett.* **13** (11), 461 (1971).
- 56 M. I. Dyakonov and A.V. Khaetskii, *Phys. Rev. Lett.* **157**, 211 (2008).
- 57 A. Hoffmann, *IEEE Transactions on Magnetism* **49** (10), 5172 (2013).
- 58 Jairo Sinova, Sergio O. Valenzuela, J. Wunderlich, C. H Back, and T. Jungwirth, *Reviews of Modern Physics* **87** (4), 1213 (2015).
- 59 G. Vignale, *Journal of Superconductivity and Novel Magnetism* **23** (1), 3 (2009).
- 60 Naoto Nagaosa, Jairo Sinova, Shigeki Onoda, A. H. MacDonald, and N. P. Ong,



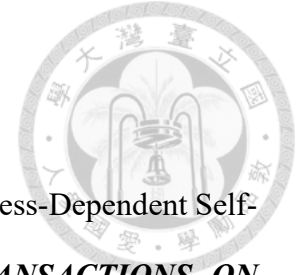
- Reviews of Modern Physics **82** (2), 1539 (2010).
- 61 R. Karplus and J. M. Luttinger, Phys. Rev. **95** (5), 1154 (1954).
- 62 Takuro Tanaka and Hiroshi Kontani, PThPS **128** (5), 805 (2012).
- 63 H. Kontani, T. Tanaka, D. S. Hirashima, K. Yamada, and J. Inoue, Phys. Rev. Lett. **102** (1), 016601 (2009).
- 64 T. Tanaka, H. Kontani, M. Naito, T. Naito, D. S. Hirashima, K. Yamada, and J. Inoue, Phys. Rev. B **77** (16) (2008).
- 65 H. L. Wang, C. H. Du, Y. Pu, R. Adur, P. C. Hammel, and F. Y. Yang, Phys. Rev. Lett. **112** (19), 197201 (2014).
- 66 Bernd Zimmermann, Kristina Chadova, Diemo Ködderitzsch, Stefan Blügel, Hubert Ebert, Dmitry V. Fedorov, Nguyen H. Long, Phivos Mavropoulos, Ingrid Mertig, Yuriy Mokrousov, and Martin Gradhand, Phys. Rev. B **90** (22) (2014).
- 67 J. Smit, Phy **24** (1-5), 39 (1958).
- 68 N. F. Mott, *The theory of atomic collisions / by N.F. Mott and H.S.W. Massey*, 3rd ed. ed. (Clarendon Press, Oxford [Oxfordshire, 1987).
- 69 Martin Gradhand, Dmitry V. Fedorov, Peter Zahn, and Ingrid Mertig, Phys. Rev. B **81** (24) (2010).
- 70 BERGER L, Phys. Rev. B **2** (11), 4559 (1970).
- 71 R. ASOMOZA', A. FERT, and R. REICH, Journal of the Less-Common Metals **90**, 177 (1983).
- 72 J. H. E. GRIFFITHS, Nature **158**, 2 (1946).
- 73 Charles Kittel, Letters to the editor **71** (270), 2 (1947).
- 74 L. LANDAU and E. LIFSHIT, Phys. Zeitsch. Sowjet **8**, 153 (1935).
- 75 O. Yalçın, *Ferromagnetic Resonance-Theory and Applications*. (InTech, 2013).
- 76 Mathias Getzlaff, *Fundamentals of magnetism by Mathias Getzlaff*. (Springer Berlin Heidelberg, Berlin, Heidelberg, 2008).
- 77 Shigemi MIZUKAMI, Yasuo ANDO, and Terunobu MIYAZAKI, JaJAP **40**, 580 (2001).
- 78 H. Nakayama, K. Ando, K. Harii, T. Yoshino, R. Takahashi, Y. Kajiwara, K. Uchida, Y. Fujikawa, and E. Saitoh, Phys. Rev. B **85** (14), 144408 (2012).
- 79 F. D. Czeschka, L. Dreher, M. S. Brandt, M. Weiler, M. Althammer, I. M. Imort, G. Reiss, A. Thomas, W. Schoch, W. Limmer, H. Huebl, R. Gross, and S. T. Goennenwein, Phys. Rev. Lett. **107** (4), 046601 (2011).
- 80 G. Y. Luo, C. R. Chang, and J. G. Lin, J. Appl. Phys. **115** (17), 17C508 (2014).
- 81 J. C. Rojas-Sanchez, N. Reyren, P. Laczkowski, W. Savero, J. P. Attane, C. Deranlot, M. Jamet, J. M. George, L. Vila, and H. Jaffres, Phys. Rev. Lett. **112** (10), 106602 (2014).
- 82 Y. Tserkovnyak, A. Brataas, and G. E. Bauer, Phys. Rev. Lett. **88** (11), 117601

- (2002).
- 83 Y. Tserkovnyak, A. Brataas, and G. E. W. Bauer, *Phys Rev B* **66** (22), 1 (2002).
- 84 K. Ando, S. Takahashi, J. Ieda, Y. Kajiwara, H. Nakayama, T. Yoshino, K. Harii,
Y. Fujikawa, M. Matsuo, S. Maekawa, and E. Saitoh, *J. Appl. Phys.* **109** (10),
103913 (2011).
- 85 S. P. Dash, S. Sharma, J. C. Le Breton, J. Peiro, H. Jaffres, J. M. George, A.
Lemaitre, and R. Jansen, *Phys. Rev. B* **84** (5), 054410 (2011).
- 86 Kiyotaka Wasa, Isaku Kanno, and Hidetoshi Kotera, *Handbook of sputter
deposition technology fundamentals and applications for functional thin films,
nano-materials and MEMS / edited by Kiyotaka Wasa, Isaku Kanno, Hidetoshi
Kotera*, 2nd ed. ed. (William Andrew, Waltham, MA, 2012).
- 87 Hartmut Frey and Hamid R. Khan, *Handbook of thin film technology / edited by
Hartmut Frey, Hamid R. Khan*. (Springer Berlin Heidelberg, Berlin, Heidelberg,
2015).
- 88 Peter M. Martin, *Handbook of deposition technologies for films and coatings
science, applications and technology / edited by Peter M. Martin*, 3rd ed. ed.
(William Andrew, Norwich, N.Y, 2009).
- 89 G. K. Wehner, *PhRv* **102** (3), 690 (1955).
- 90 D. Rosenberg and G. K. Wehner, *J. Appl. Phys.* **33** (5), 1842 (1962).
- 91 James F. Lutsko, in *New Perspectives on Mineral Nucleation and Growth: From
Solution Precursors to Solid Materials*, edited by Alexander E. S. Van Driessche,
Matthias Kellermeier, Liane G. Benning et al. (Springer International Publishing,
Cham, 2017), pp. 25.
- 92 J. A. Venables and G. D. T. Spiller, in *Surface Mobilities on Solid Materials:
Fundamental Concepts and Applications*, edited by Vu Thien Binh (Springer US,
Boston, MA, 1983), pp. 341.
- 93 R. Kumar, G. Kumar, and A. Umar, *J. Nanosci. Nanotechnol* **14** (2), 1911 (2014).
- 94 Peter Y. Yu, *Fundamentals of semiconductors physics and materials properties /
by Peter Y. Yu, Manuel Cardona*, 4th ed. ed. (Springer-Verlag Berlin Heidelberg,
Berlin, Heidelberg, 2010).
- 95 Jurgen Thomas, *Analytical transmission electron microscopy : an introduction for
operators / by Jurgen Thomas, Thomas Gemming*. (Springer Netherlands,
Dordrecht, 2014).
- 96 Ludwig Reimer, *Transmission electron microscopy physics of image formation /
by Ludwig Reimer, Helmut Kohl*. (Springer-Verlag New York, New York, NY,
2008).
- 97 B. D. Cullity, *Introduction to magnetic materials B.D. Cullity, C.D. Graham*, 2nd
ed. ed. (IEEE/Wiley, Hoboken, N.J, 2009).

- 98 Sheng S. Li, *Semiconductor Physical Electronics by Sheng S. Li*, Second Edition.
ed. (Springer Science+Business Media, LLC, New York, NY, 2006).
- 99 A. Dankert, R. S. Dulal, and S. P. Dash, *Scientific Reports* **3** (3196), 3196 (2013).
- 100 Chi-Feng Pai, Yongxi Ou, Luis Henrique Vilela-Leão, D. C. Ralph, and R. A.
Buhrman, *Phys. Rev. B* **92** (6) (2015).
- 101 H. Y. Hung, G. Y. Luo, Y. C. Chiu, P. Chang, W. C. Lee, J. G. Lin, S. F. Lee, M.
Hong, and J. Kwo, *J. Appl. Phys.* **113** (17), 17C507 (2013).
- 102 Ryo Ohshima, Stefan Klingler, Sergey Dushenko, Yuichiro Ando, Mathias Weiler,
Hans Huebl, Teruya Shinjo, Sebastian T. B. Goennenwein, and Masashi Shiraishi,
Appl. Phys. Lett. **110** (18), 182402 (2017).
- 103 T. G. Verhagen, H. N. Tinkey, H. C. Overweg, M. van Son, M. Huber, J. M. van
Ruitenbeek, and J. Aarts, *J. Phys.: Condens. Matter* **28** (5), 056004 (2016).
- 104 Y. Li and W. E. Bailey, *Phys. Rev. Lett.* **116** (11), 117602 (2016).
- 105 K. Ando, S. Takahashi, K. Harii, K. Sasage, J. Ieda, S. Maekawa, and E. Saitoh,
Phys. Rev. Lett. **101** (3), 036601 (2008).
- 106 Michael Farle, *Rep. Prog. Phys.* **61**, 755 (1998).
- 107 A. Tsukahara, Y. Ando, Y. Kitamura, H. Emoto, E. Shikoh, M. P. Delmo, T. Shinjo,
and M. Shiraishi, *Phys. Rev. B* **89** (23), 235317 (2014).
- 108 Kazunari Kanagawa, Yoshio Teki, and Eiji Shikoh, *AIP Advances* **8** (5), 055910
(2018).
- 109 Jack Bass and William P. Pratt, *J. Phys.: Condens. Matter* **19** (18), 183201
(2007).
- 110 M. Obstbaum, M. Hartinger, H. G. Bauer, T. Meier, F. Swientek, C. H. Back, and
G. Woltersdorf, *Phys. Rev. B* **89** (6), 060407(R) (2014).
- 111 V. Vlaminck, J. E. Pearson, S. D. Bader, and A. Hoffmann, *Phys. Rev. B* **88** (6),
064414 (2013).
- 112 W. Zhang, V. Vlaminck, J. E. Pearson, R. Divan, S. D. Bader, and A. Hoffmann,
Appl. Phys. Lett. **103** (24), 242414 (2013).
- 113 Z. Feng, J. Hu, L. Sun, B. You, D. Wu, J. Du, W. Zhang, A. Hu, Y. Yang, D. M.
Tang, B. S. Zhang, and H. F. Ding, *Phys. Rev. B* **85** (21), 214423 (2012).
- 114 Y. Wang, P. Deorani, X. P. Qiu, J. H. Kwon, and H. S. Yang, *Appl. Phys. Lett.*
105 (15), 152412 (2014).
- 115 F. Rortais, S. Oyarzun, F. Bottegoni, J. C. Rojas-Sanchez, P. Laczkowski, A.
Ferrari, C. Vergnaud, C. Ducruet, C. Beigne, N. Reyren, A. Marty, J. P. Attane, L.
Vila, S. Gambarelli, J. Widiez, F. Ciccacci, H. Jaffres, J. M. George, and M. Jamet,
J. Phys. Condens. Matter **28** (16), 165801 (2016).
- 116 Yi-Chien Weng, C. T. Liang, and Jauyn Grace Lin, *Appl. Phys. Lett.* **115** (23)
(2019).

- 
- 117 W. K. Tse and S. Das Sarma, *Phys. Rev. Lett.* **96** (5), 056601 (2006).
118 Z. S. Popović, Jamshid Moradi Kurdestany, and S. Satpathy, *Phys. Rev. B* **92**
(3), 035135 (2015).
119 A. Jain, J. C. Rojas-Sanchez, M. Cubukcu, J. Peiro, J. C. Le Breton, E. Prestat, C.
Vergnaud, L. Louahadj, C. Portemont, C. Ducruet, V. Baltz, A. Barski, P. Bayle-
Guillemaud, L. Vila, J. P. Attane, E. Augendre, G. Desfonds, S. Gambarelli, H.
Jaffres, J. M. George, and M. Jamet, *Phys. Rev. Lett.* **109** (10), 106603 (2012).
120 J. C. Rojas-Sánchez, M. Cubukcu, A. Jain, C. Vergnaud, C. Portemont, C. Ducruet,
A. Barski, A. Marty, L. Vila, J. P. Attané, E. Augendre, G. Desfonds, S. Gambarelli,
H. Jaffrès, J. M. George, and M. Jamet, *Phys. Rev. B* **88** (6), 064403 (2013).

List of publications



1. **Yi-Chien Weng**, G. Y. Luo, C.-T. Liang, and J. G. Lin. “Thickness-Dependent Self-Induced Spin-Pumping in Cobalt Thin Films.” *IEEE TRANSACTIONS ON MAGNETICS*, VOL. 53, NO. 11, (2017).
2. **Yi-Chien Weng**, C.-T. Liang, and Jauyn Grace Lin. “Modulation of spin-charge conversion in silicon.” *Applied Physics Letters*, 115, 232101 (2019).
3. **Yi-Chien Weng**, C.-T. Liang, and J. G. Lin. “Detection of torque effects in Co/Pt via ferromagnetic resonance.” *AIP Advances*, 9, 125135 (2019).
4. Yi-Hsiang Huang, **Yi-Chien Weng**, Chi-Te Liang, and J. G. Lin (2020, Jan). “Spin Hall angle and spin diffusion length of permalloy.” *AIP Advances*, 10, 015041, (2019).
5. Tzu-Hsiang Lo, **Yi-Chien Weng**, Chi-Feng Pai, and J.G. Lin (2020, Jan). “Effect of asymmetric Pt thickness on the inverse spin Hall voltage in Pt/Co/Pt trilayers.” *AIP Advances*, 10, 025120 (2020)
6. **Yi-Chien Weng**, C.-T. Liang, and Jauyn Grace Lin. “Influence of dopants on spin-charge conversion of GaAs” submitted to Applied physics letters on July 1(2020)



Appendix A

The resistance values can be obtained by the two different methods: the two-point probe and the equivalent circuit model. The equation of equivalent circuit model is shown as

$$R = \frac{R_{Co}R_{SC}}{(R_{Co} + R_{SC})}$$

$$R_{Co,SC} = \rho \frac{L}{A}$$

where R is total resistance, R_{Co} is resistance of Co layer and R_{SC} is resistance of SC layer, ρ is resistivity, L and A is length and cross-section area of sample, respectively. The conductivity of Co is $3.57 (\mu\Omega\text{-m})^{-1}$ and it was measured by four-point probe.

The comparison results of resistance are show in the table I ~ II and Fig. I ~ V for sample A; the two-point probe (black squares) and the equivalent circuit model (red circles).

Table I The values of resistance are measured by two-point probe for sample A.

| Sub. t_{Co} | <i>undoped-Si</i> | <i>n-Si-10</i> | <i>p-Si-10</i> | <i>p-Si-0.1</i> | <i>p-Si-0.005</i> |
|------------------|-------------------|----------------|----------------|-----------------|-------------------|
| 5 nm | 187.0 | 174.7 | 172.1 | 140.4 | 83.8 |
| 7 nm | 92.3 | 96.8 | 142.0 | 80.6 | 50.5 |
| 10 nm | 48.6 | 47.7 | 72.5 | 52.3 | 34.6 |
| 13 nm | 52.7 | 32.4 | 41.1 | 34.6 | 29.2 |
| 15 nm | 32.5 | 30.6 | 29.8 | 27.6 | 25.2 |
| 20 nm | 22.4 | 20.7 | 23.9 | 19.4 | 19.6 |
| 25 nm | 16.3 | 16.8 | 19.7 | 18.3 | 20.8 |
| 30 nm | 15.2 | 16.9 | 17.8 | 14.2 | 14.9 |
| 40 nm | 10.8 | 11.3 | 10.7 | 11.2 | 8.9 |

Table II The values of resistance are calculated by equivalent circuit model for sample A.

| Sub. t_{Co} | <i>undoped-Si</i> | <i>n-Si-10</i> | <i>p-Si-10</i> | <i>p-Si-0.1</i> | <i>p-Si-0.005</i> |
|------------------|-------------------|----------------|----------------|-----------------|-------------------|
| 5 nm | 112.0 | 69.6 | 84.5 | 5.69 | 0.2793 |
| 7 nm | 80.0 | 55.8 | 64.9 | 5.58 | 0.2790 |
| 10 nm | 56.0 | 42.9 | 48.2 | 5.42 | 0.2786 |
| 13 nm | 43.1 | 34.9 | 38.3 | 5.27 | 0.2782 |
| 15 nm | 37.3 | 31.0 | 33.7 | 5.17 | 0.2779 |
| 20 nm | 28.0 | 24.3 | 25.9 | 4.94 | 0.2772 |
| 25 nm | 22.4 | 20.0 | 21.0 | 4.73 | 0.2765 |
| 30 nm | 18.7 | 16.9 | 17.7 | 4.54 | 0.2759 |
| 40 nm | 14.0 | 13.0 | 13.5 | 4.20 | 0.2745 |

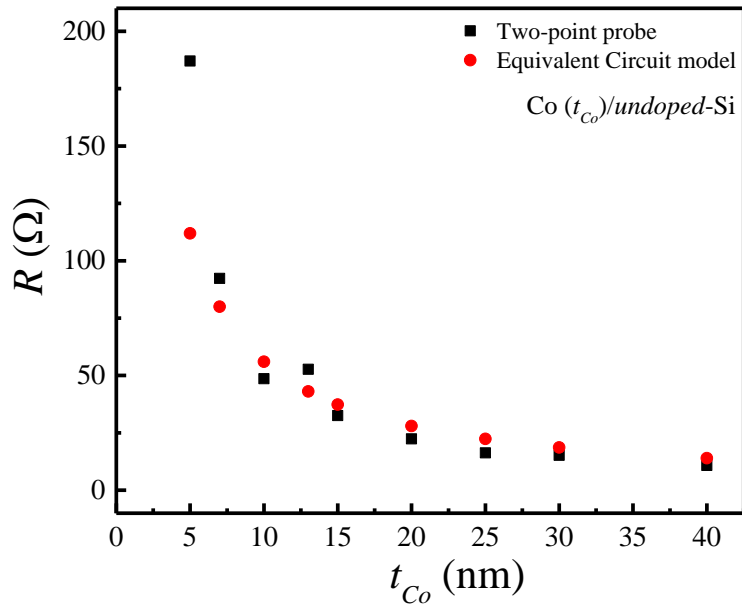


Fig. I The comparison results of $Co(t_{Co})/undoped-Si$.

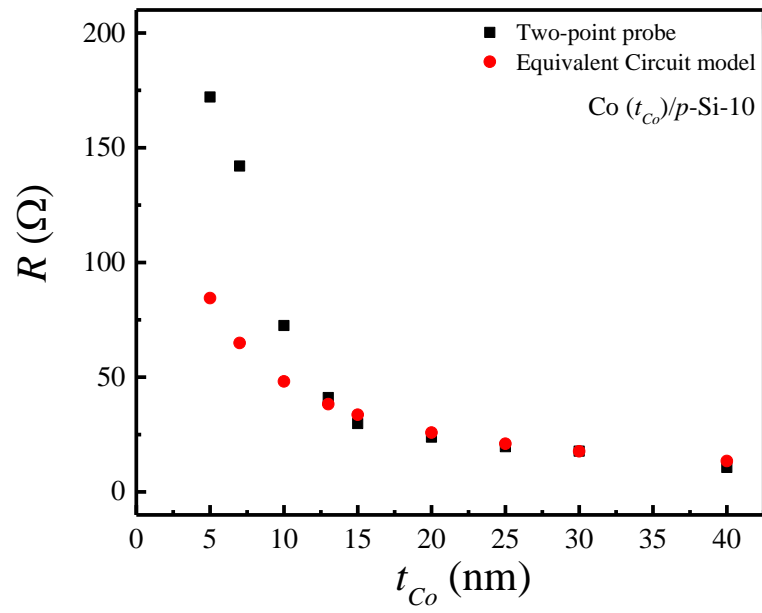


Fig. II The comparison results of Co (t_{Co})/p-Si-10.

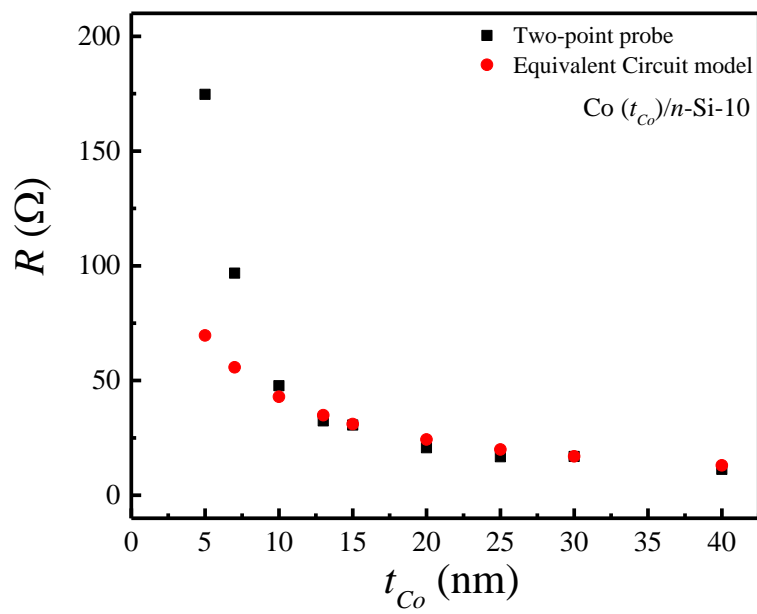


Fig. III The comparison results of Co (t_{Co})/n-Si-10.

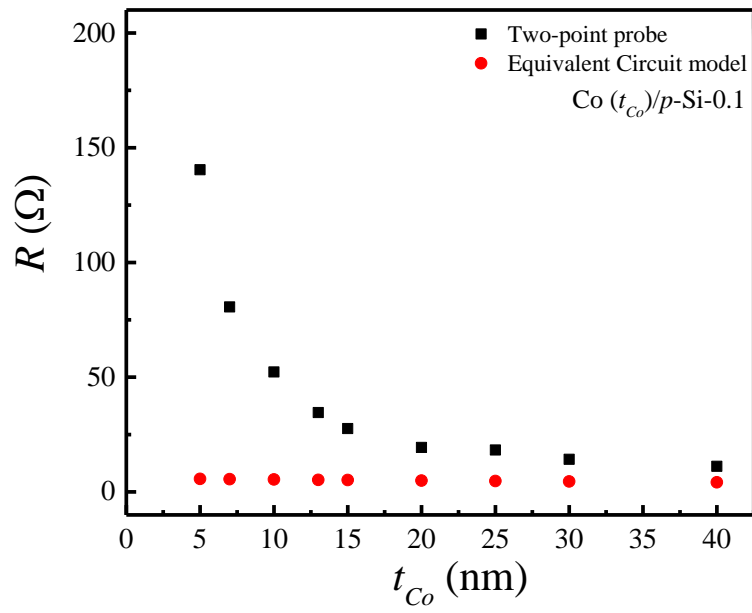


Fig. IV The comparison results of Co (t_{Co})/p-Si-0.1.

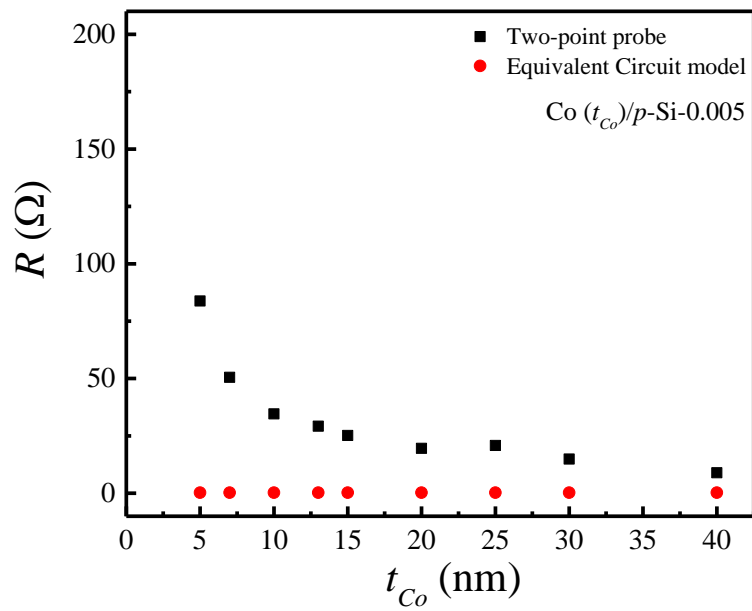
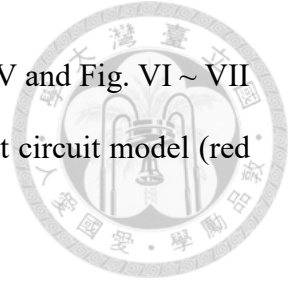


Fig. V The comparison results of Co (t_{Co})/p-Si-0.005.



The comparison result of resistance are show in the table III ~ IV and Fig. VI ~ VII for sample B; the two-point probe (black squares) and the equivalent circuit model (red circles).

Table III The values of resistance are measured by two-point probe for sample B.

| Sub. <i>t_{Co}</i> | <i>n</i>-GaAs | <i>p</i>-GaAs |
|--------------------------------------|----------------------|----------------------|
| 5 nm | 240.0 | 170.0 |
| 7 nm | 126.0 | 76.0 |
| 10 nm | 48.0 | 50.0 |
| 13 nm | 82.0 | 69.7 |
| 15 nm | 32.8 | 35.0 |
| 20 nm | 44.0 | 30.0 |
| 25 nm | 24.3 | 22.4 |
| 30 nm | 23.0 | 15.8 |
| 40 nm | 23.0 | 11.0 |

Table IV The values of resistance are calculated by equivalent circuit model for sample B.

| Sub. <i>t_{Co}</i> | <i>n</i>-GaAs | <i>p</i>-GaAs |
|--------------------------------------|----------------------|----------------------|
| 5 nm | 0.05697 | 3.85 |
| 7 nm | 0.05696 | 3.80 |
| 10 nm | 0.05694 | 3.72 |
| 13 nm | 0.05692 | 3.65 |
| 15 nm | 0.05691 | 3.60 |
| 20 nm | 0.05688 | 3.49 |
| 25 nm | 0.05686 | 3.39 |
| 30 nm | 0.05683 | 3.29 |
| 40 nm | 0.05677 | 3.10 |

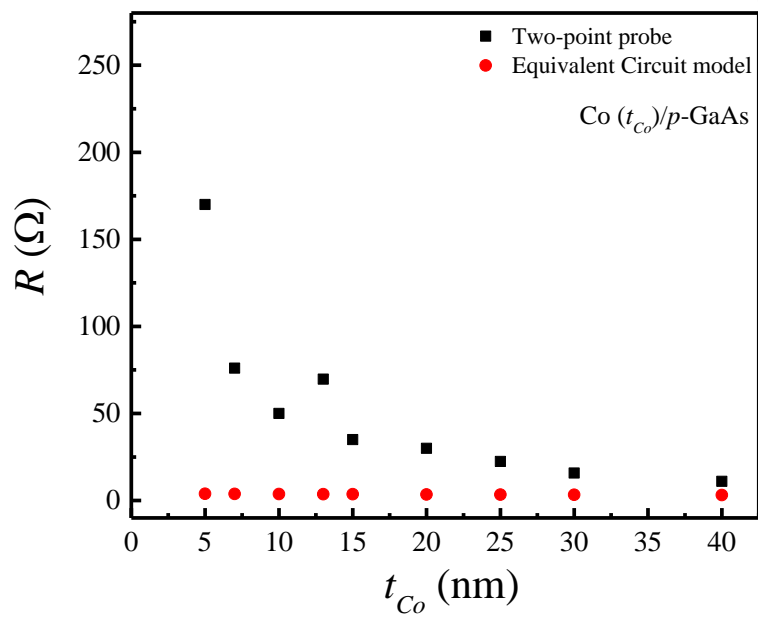


Fig. VI The comparison results of Co (t_{Co})/p-GaAs.

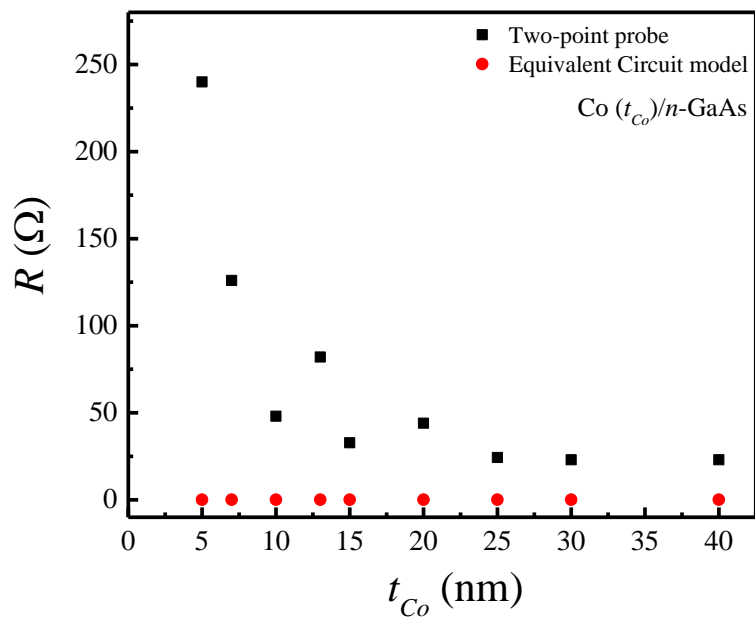


Fig. VII The comparison results of Co (t_{Co})/n-GaAs.

Appendix B



The FMR spectra and voltage signals are measured with different θ_H (change from 0° to 180°) for Pt/Co (10)/undoped, Co (10)/undoped-Si, Co (10)/p-Si-10, Co (10)/n-Si-10, Co (10)/p-Si-0.1, Co (10)/p-Si-0.005. Due to the instrument limit, we could not measure the FMR spectra at the out of plane, θ_H is 90° , for all samples.

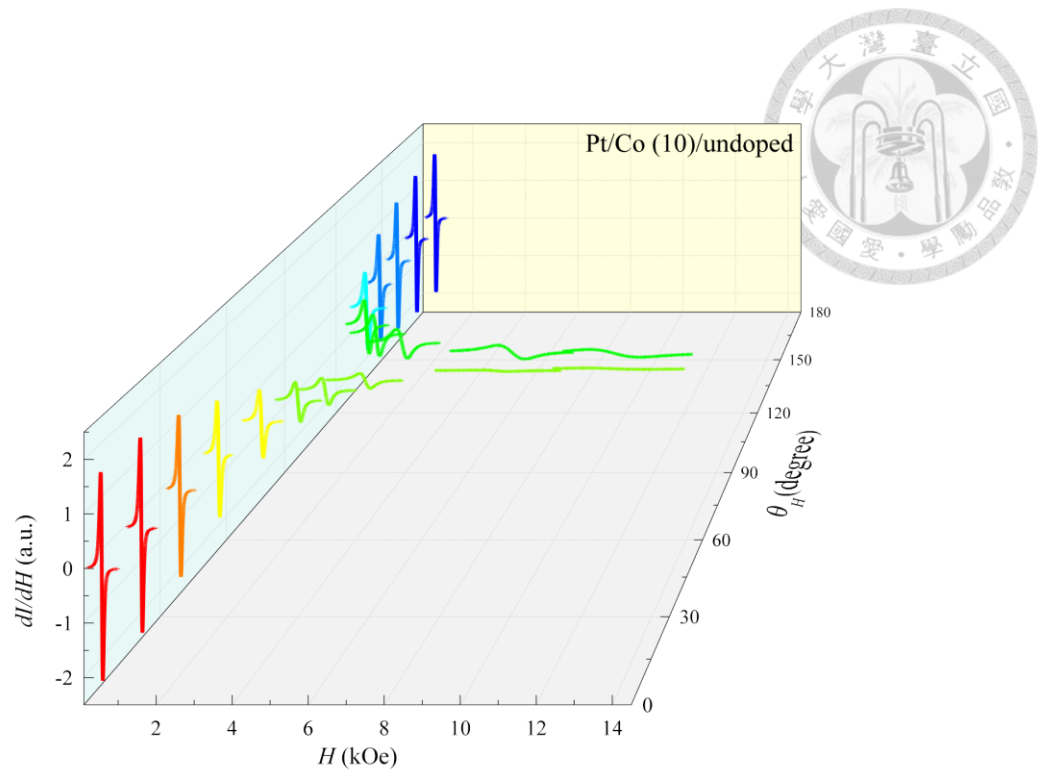


Fig. I The FMR spectra with θ_H changing from 0° to 180° for Pt/Co (10)/undoped.

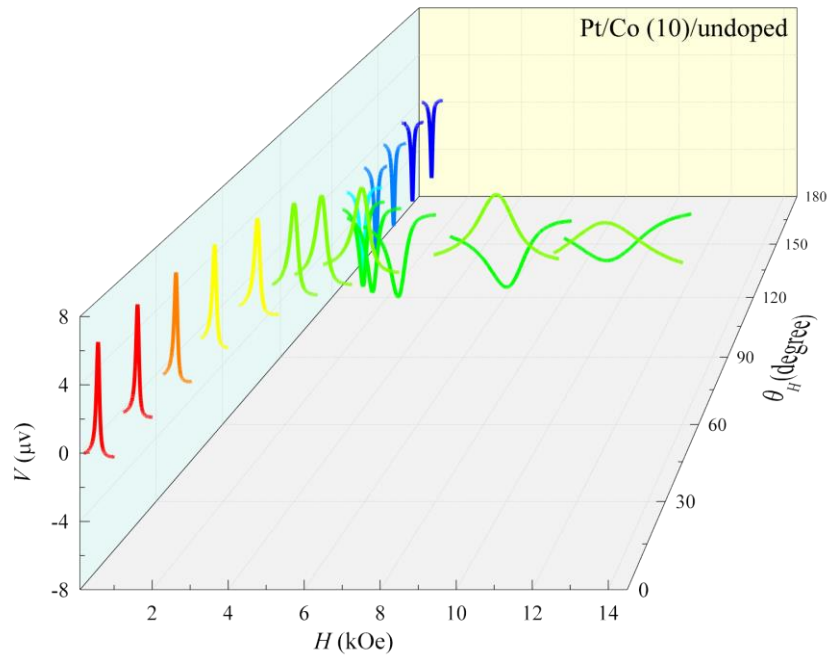


Fig. II The voltage signals with θ_H changing from 0° to 180° for Pt/Co (10)/undoped.

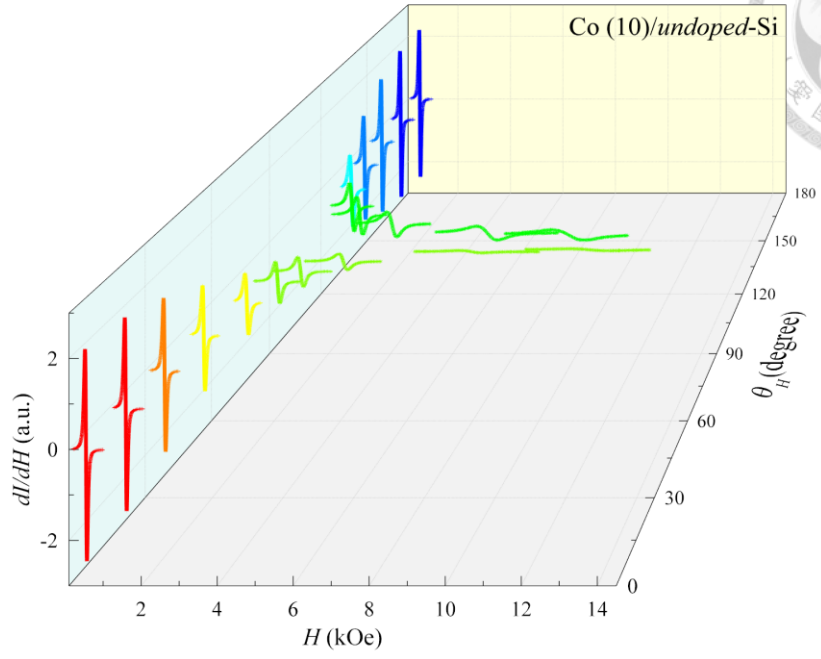


Fig. III The FMR spectra with θ_H changing from 0° to 180° for Co (10)/undoped-Si.

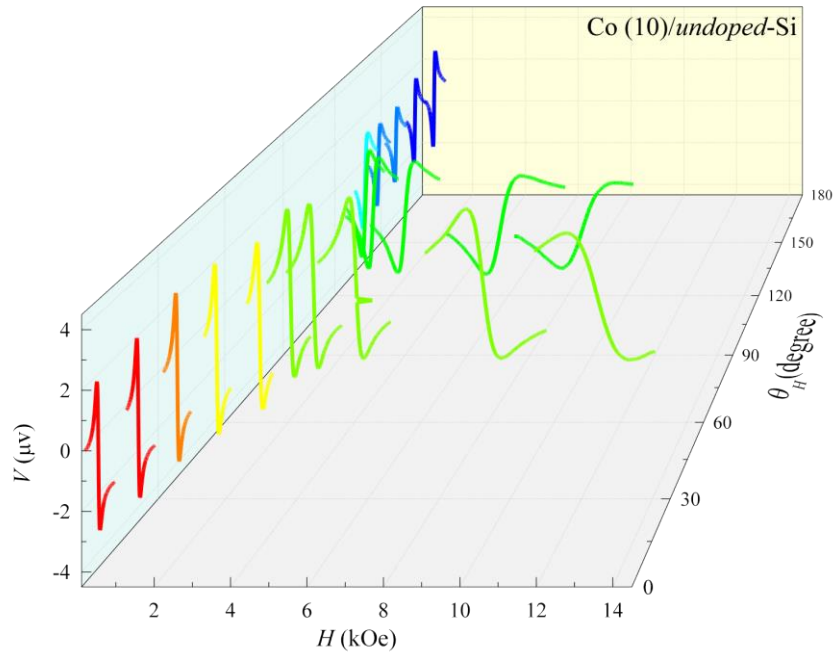


Fig. IV The voltage signals with θ_H changing from 0° to 180° for Co (10)/undoped-Si.

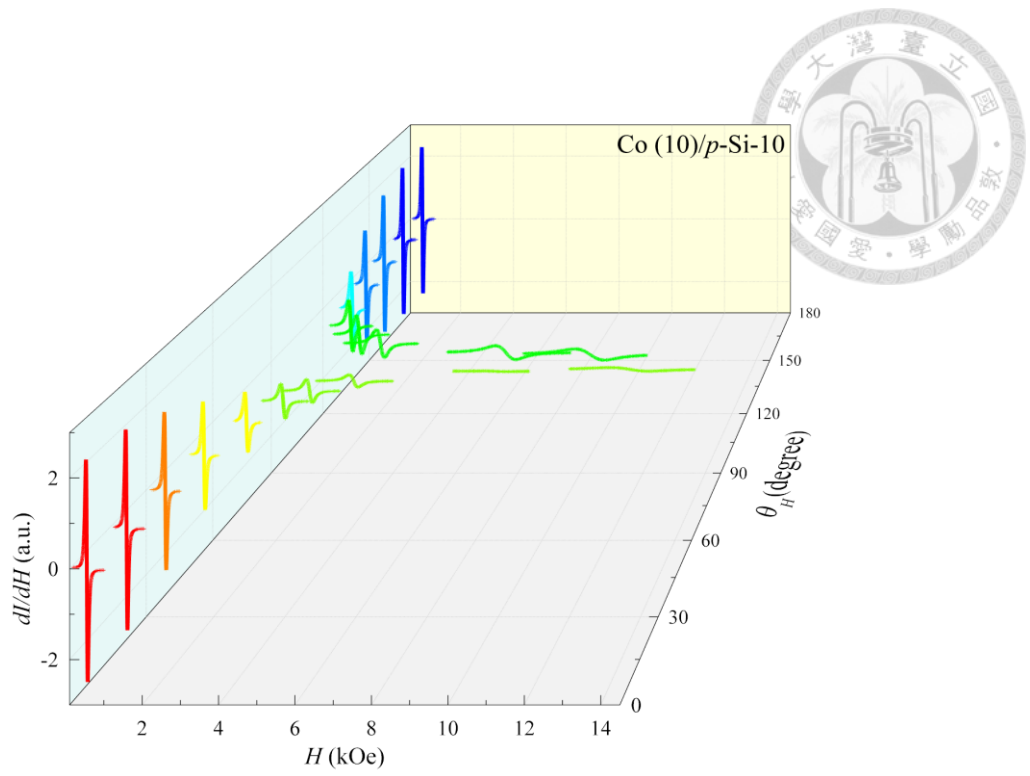


Fig. V The FMR spectra with θ_H changing from 0° to 180° for Co (10)/p-Si-10.

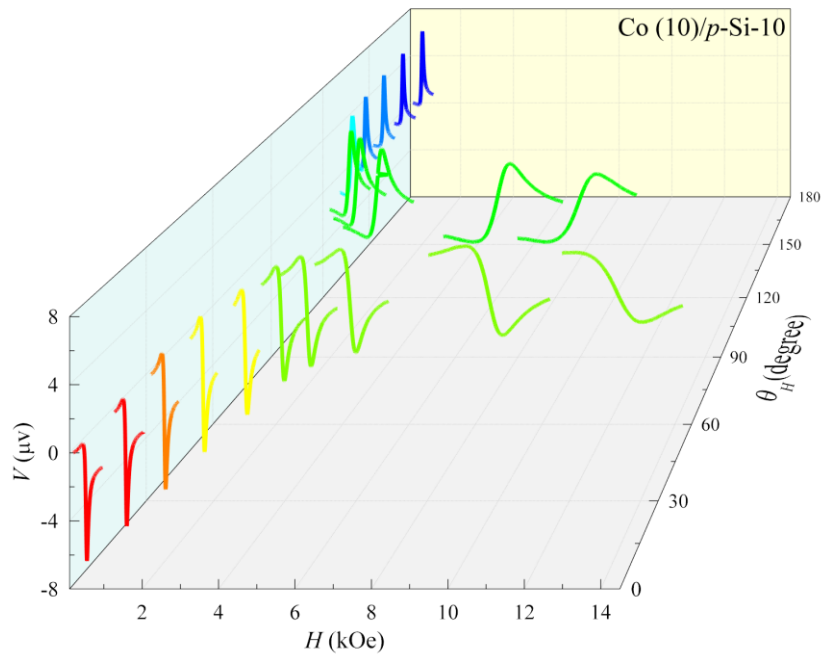


Fig. VI The voltage signals with θ_H changing from 0° to 180° for Co (10)/p-Si-10.

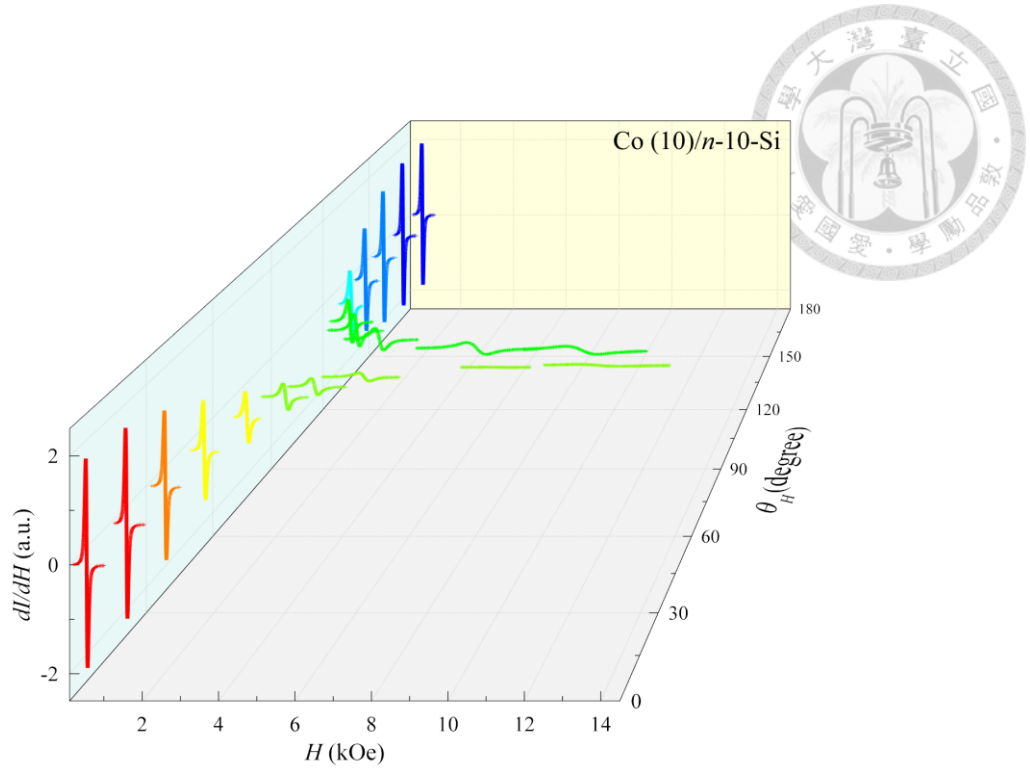


Fig. VII The FMR spectra with θ_H changing from 0° to 180° for Co (10)/n-Si-10.

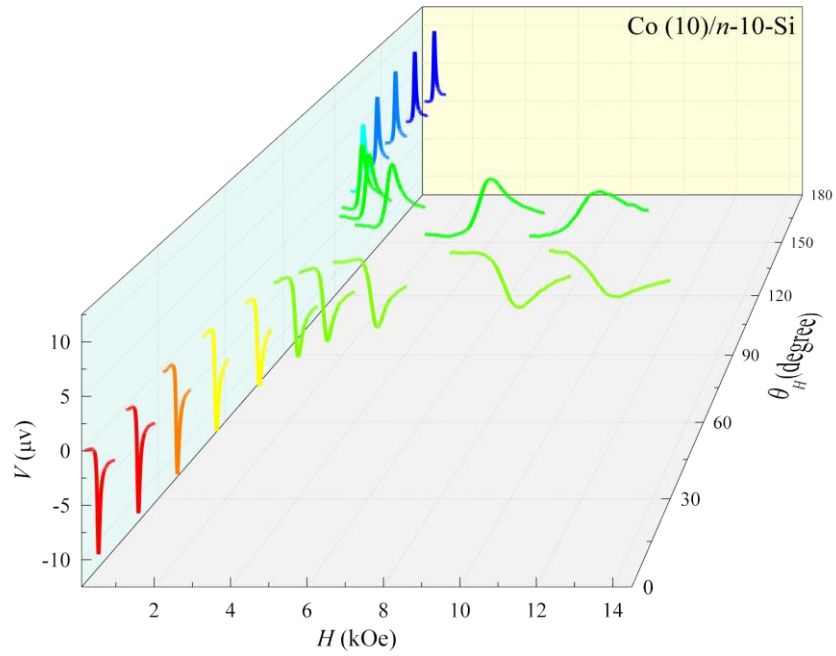


Fig. VIII The voltage signals with θ_H changing from 0° to 180° for Co (10)/n-Si-10.

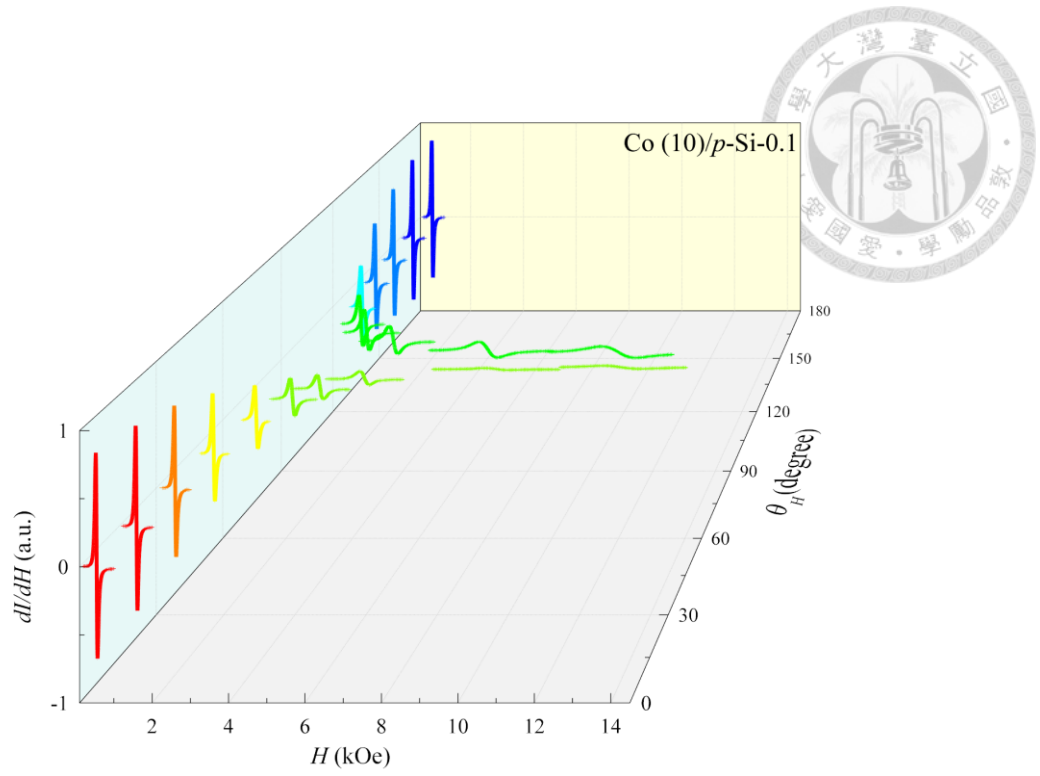


Fig. IX The FMR spectra with θ_H changing from 0° to 180° for Co (10)/p-Si-0.1.

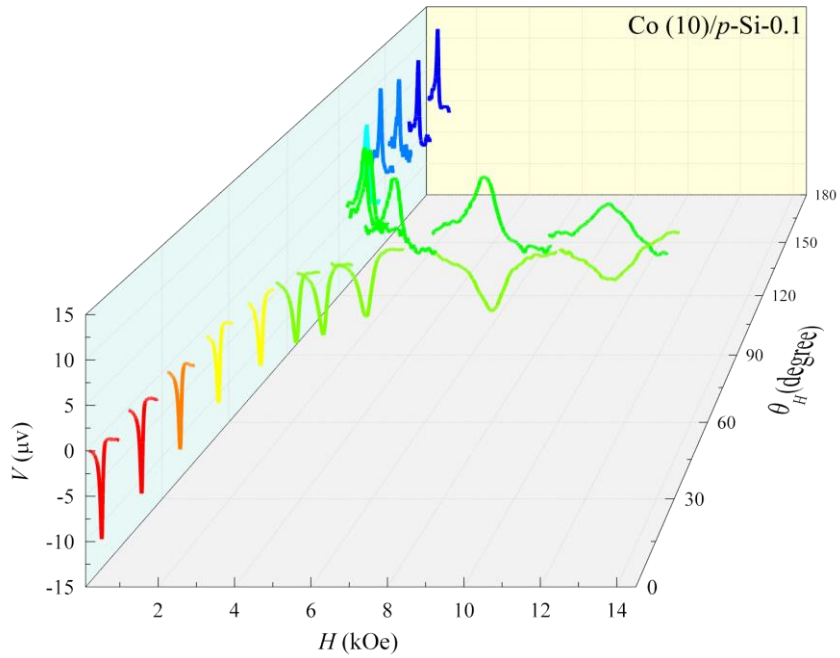


Fig. X The voltage signals with θ_H changing from 0° to 180° for Co (10)/p-Si-0.1.

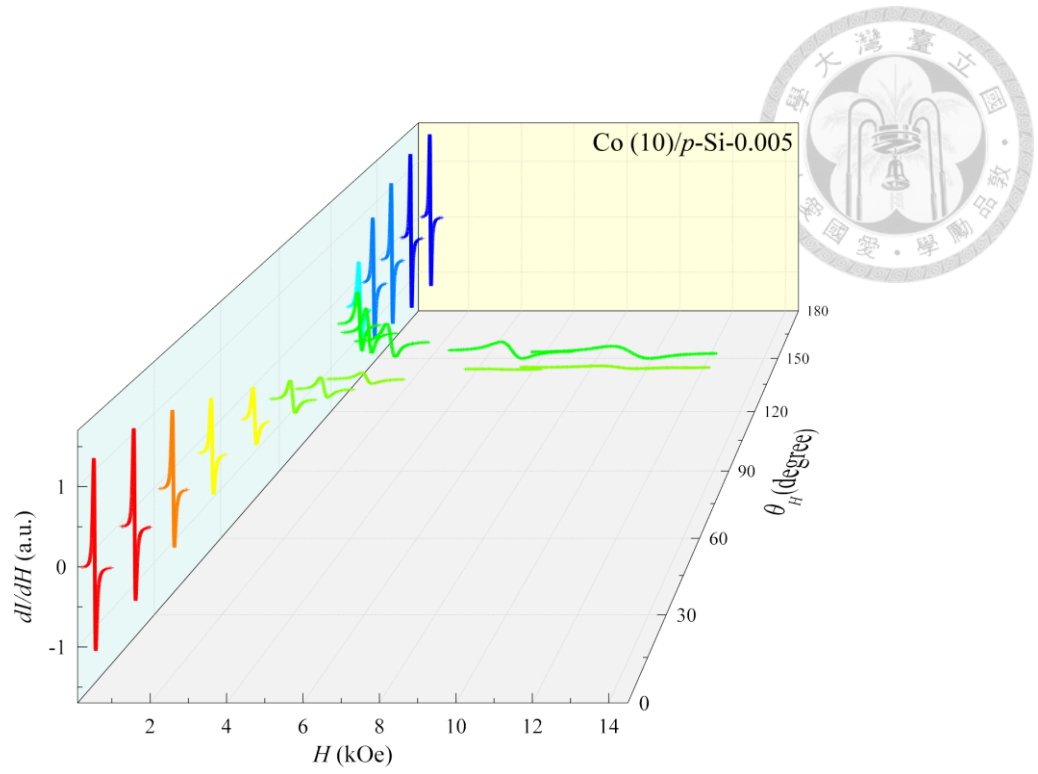


Fig. XI The FMR spectra with θ_H changing from 0° to 180° for Co (10)/p-Si-0.005.

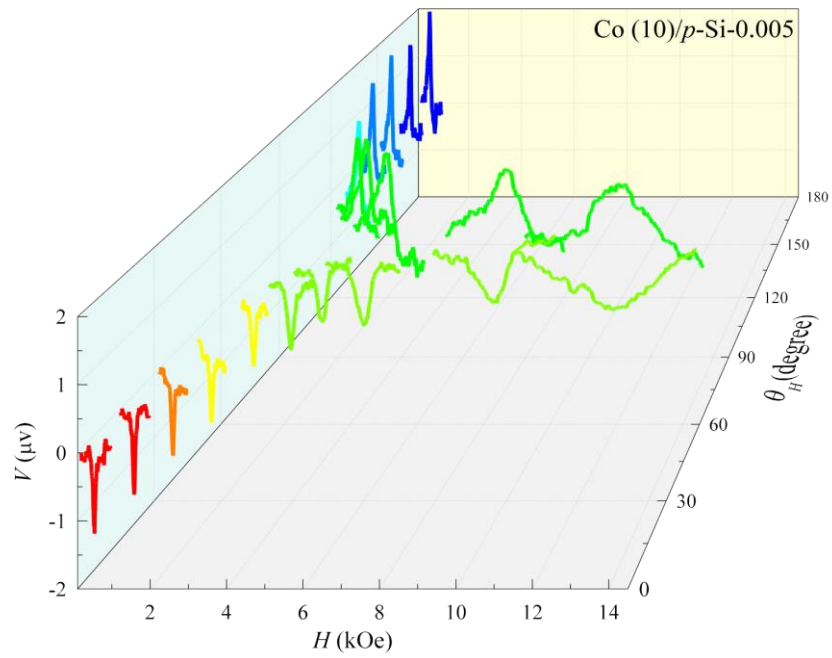


Fig. XII The voltage signals with θ_H changing from 0° to 180° for Co (10)/p-Si-0.005.

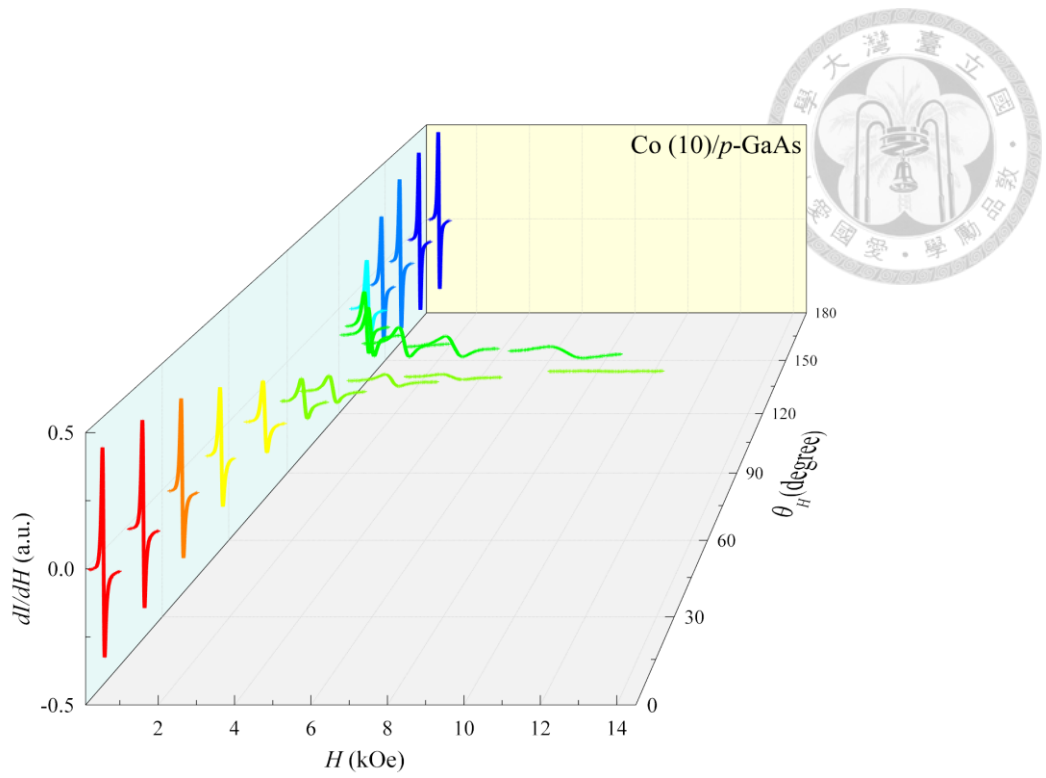


Fig. XIII The FMR spectra with θ_H changing from 0° to 180° for Co (10)/p-GaAs.

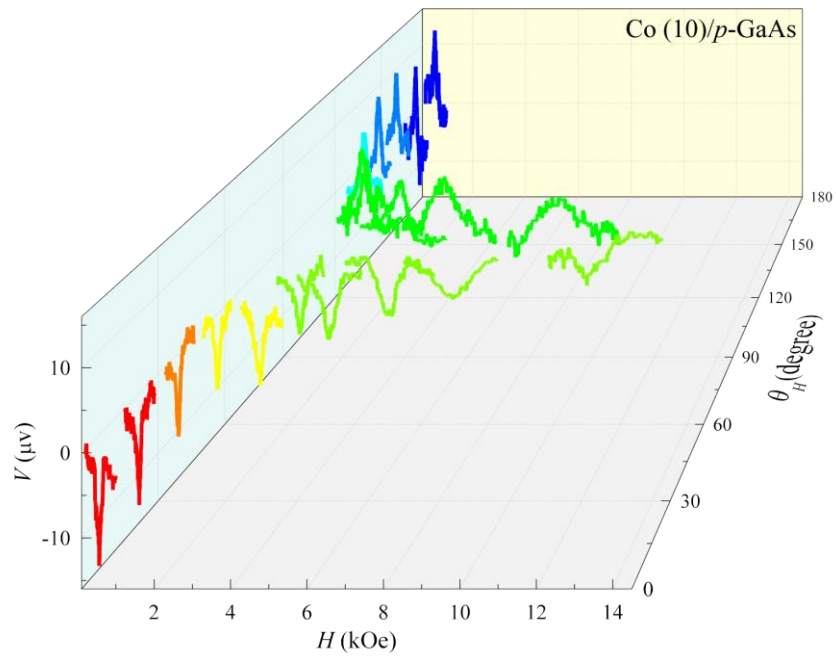


Fig. XIV The voltage signals with θ_H changing from 0° to 180° for Co (10)/p-GaAs.

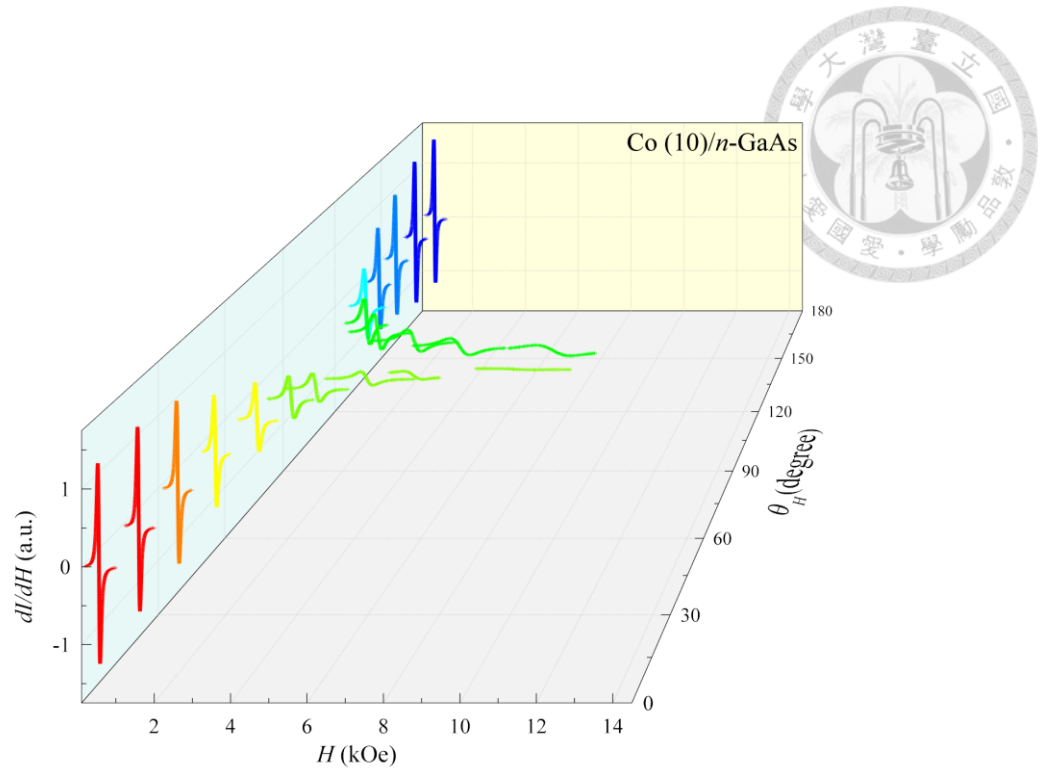


Fig. XV The FMR spectra with θ_H changing from 0° to 180° for Co (10)/n-GaAs.

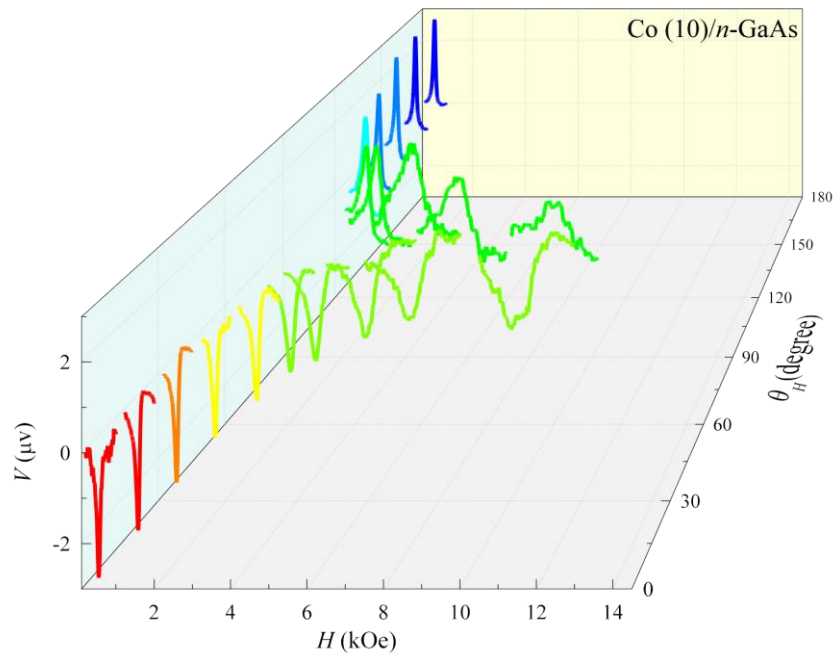


Fig. XVI The voltage signals with θ_H changing from 0° to 180° for Co (10)/n-GaAs.

Appendix C



The computer code for obtaining the normalized value of $V_{ISHE}(\theta_H)$. (Eq. 2.51).

```
clear all;

data='data input.txt';

input=load(data);

a=input(:,1);    % theta H
b=input(:,2);    % theta M

a=a*pi/180;
b=b*pi/180;

g=4.8*10^19    % mixing conductance

Ms=1270    % saturation magnetization (emu/cm^3)

fourMs=(4*pi*Ms*(10^-4))

p=50*10^-3;    % Power of magnetic field

h=(1.4*(sqrt(p)))*(10^-4)    % magnetic of MW

alpha=0.0130

hbar=1.054*10^-34

gamma=1.77*10^11;    % gyromagnetic ratio

f=9.8*10^9;    % frequency

omega=2*pi*f    % omega

DN=0.00036    %diffusion constant
```

```

omegaL=1*10^10

l = linspace(1e-10,2.8e-10,10);

Nv = length(l);

js=zeros(11,1)

for i=1:11

js(i)=((g*(gamma^2)*(h^2)*hbar)*(fourMs*gamma*((cos(b(i)))^2)+sqrt((fourMs^2)*(gamma^2)*
((cos(b(i)))^4)+(4*omega^2)))))...

/((8*pi*(alpha^2))*((fourMs^2)*(gamma^2)*((cos(b(i)))^4)+(4*omega^2)))

end

for i=1:11

for j =1:Nv

fun = @(x) exp(-x./l(j));

VISHE(i,j)=js(i)*cos(b(i))*integral(fun,0,5e-4,'RelTol',1e-9,'AbsTol',1e-9);

```

```

end

end

for i =1:10

    NorVISHE(:,i) = VISHE(:,i)./ VISHE(1,i);

end

% Vspin=zeros(11,1);

for i=1:11

    for j =1:Nv

        fun = @(x) exp(-x./(DN*l(j)).^(1/2));

        fun1 = @(x) real(exp(-x./(sqrt(DN*l(j))/sqrt(1+1i*omegaL*l(j)))));

%     fun1 = @(x) real(exp((-x./(sqrt(DN*l(j))))*sqrt(1+1i*omegaL*l(j))));

```

```

%   vspin(i,j)=js(i)*...

%       ((cos(a(i))*cos((a(i)-b(i))))*integral(fun,0,5e-4,'RelTol',1e-9,'AbsTol',1e-
9))...

%       +((sin(a(i))*sin((a(i)-b(i))))*integral(fun1,0,5e-4,'RelTol',1e-9,'AbsTol',1e-
9));

aaa=(cos(a(i))*cos((a(i)-b(i))))*integral(fun,0,5e-4,'RelTol',1e-9,'AbsTol',1e-9)

bbb=(sin(a(i))*sin((a(i)-b(i))))*integral(fun1,0,5e-4,'RelTol',1e-9,'AbsTol',1e-9)


vspin(i,j)=js(i)*(aaa+bbb)


end


end


for i =1:10

    Norvspin(:,i) = vspin(:,i)./ vspin(1,i);

end

```